AFCRL-66-767

AD 644243

INVESTIGATION OF ELECTRONIC FRINGE DETECTOR FOR A STELLAR INTERFEROMETER

John Boardman, Paul Kellen, and Diana Nyyssonen

Technical Operations Research
Burlington, Massachusetts

Contract No. AF19(628)-5145

CLEARINGHOUSE
FOR FEDERAL SCIENTIFIC AND
TECHNICAL INFORMATION

Hardcopy	Microfiche		
$3.00	$.65	90 pp	as

ARCHIVE COPY

Project No. 8663

Scientific Report No. 1

7 November 1966

Contract Monitor: George A. Vanasse

Distribution of this document
is unlimited

Research was sponsored by the Advanced Research Projects Agency, ARPA Order No. 450, Amendment 2, 4

DDC
RECEIVED
JAN 3 1967
C

Prepared
for

AIR FORCE CAMBRIDGE RESEARCH LABORATORIES
OFFICE OF AEROSPACE RESEARCH
UNITED STATES AIR FORCE
BEDFORD, MASSACHUSETTS

AFCRL-66-767

INVESTIGATION OF ELECTRONIC FRINGE DETECTOR FOR A STELLAR INTERFEROMETER

John Boardman, Paul Kellen, and Diana Nyyssonen

Technical Operations Research
Burlington, Massachusetts

Contract No. AF19(628)-5145

Project No. 8663

Scientific Report No. 1

7 November 1966

Contract Monitor: George A. Vanasse

Distribution of this document is unlimited

Research was sponsored by the Advanced Research Projects Agency, ARPA Order No. 450, Amendment 2, 4

Prepared
for

AIR FORCE CAMBRIDGE RESEARCH LABORATORIES
OFFICE OF AEROSPACE RESEARCH
UNITED STATES AIR FORCE
BEDFORD, MASSACHUSETTS

ABSTRACT

A fringe detector was constructed to detect fringes from a Michelson stellar interferometer and to relate these measurements to the characteristics of the source of illumination. This instrument has variable separation apertures adjustable from 0.6 to 6 cm. Aperture height is maintained at 0.1 times the separation. An optical system produces the fringe pattern by superimposing the partially coherent light entering the two apertures. A rotating reflector, single slit, and phototube combine to transform the spatially varying intensity pattern of the fringe field into a time-varying voltage signal displayed on an oscilloscope face. The oscilloscope trace is photographed and analyzed to determine fringe contrast.

The maximum sensitivity of the detector was determined to be equivalent to a source providing 10^{-10} watts/cm^2 at a fringe contrast of 1 and a signal-to-noise ratio of 1. Improvements in the entrance aperture configuration, phototube sensitivity, and the use of a grating instead of a single slit can provide a factor of 500 to 1000 improvement in detector sensitivity. The interferometer was determined to have potentially better resolution than a single-mirror telescope because it can electrically filter the effects of ambient background illumination and turbulence. The use of an interferometer to measure the angular size of a pie-shaped source was studied and found to be not particularly suited to this purpose.

TABLE OF CONTENTS

Section		Page
I	INTRODUCTION AND SUMMARY	1
II	DESIGN CRITERIA	3
	MICHELSON STELLAR INTERFEROMETER	3
	GENERAL REQUIREMENTS FOR FRINGE DETECTOR	5
	DETECTION AND MEASUREMENT OF FRINGE CONTRAST	5
	VARIABLE SEPARATION APERTURES	6
	OPTICAL SYSTEM	6
	CHOPPING AND BANDWIDTH	6
	REVIEW OF DESIGN PROBLEM	7
	OTHER SYSTEMS CONSIDERED	7
III	FRINGE DETECTOR DESIGN	10
	CONFIGURATION AND OPERATION	10
	VARIABLE SEPARATION APERTURES	12
	OPTICAL SYSTEM	12
	SILVERED ROTATING REFLECTOR	13
	SINGLE SLIT	13
	ELECTRONICS	13
IV	RESEARCH PROGRAM	14
	THEORETICAL RESEARCH	14
	THEORY OF SPATIAL FILTER	14
	SQUARE WAVE GRATING	15
	SINGLE SLIT	16
	SENSITIVITY CONSIDERATIONS	16
	EXPERIMENTAL RESEARCH	18
	SHOT NOISE FILTERING	19
	INSTRUMENT CALIBRATION	22

TABLE OF CONTENTS (Cont'd.)

Section		Page
	Frequency-Bandwidth Considerations	22
	Detector Slit-Width Considerations	22
	PERFORMANCE OF FRINGE DETECTOR	25
	Measurement of Angular Source Sizes	25
	DETECTION CAPABILITIES OF FRINGE DETECTOR	29
	Outside Noise Sources	31
V	COMPARISON OF TELESCOPE AND INTERFEROMETER	33
VI	INVESTIGATION OF PIE-SHAPED SOURCES	35
	THEORY	35
	COMPUTER CALCULATIONS	38
	EXPERIMENT	49
VII	CONCLUSIONS AND RECOMMENDATIONS	54
	SUMMARY	54
	FRINGE DETECTOR	54
	COMPARISON WITH TELESCOPE	55
	PIE-SHAPED SOURCES	55
REFERENCES		56
APPENDIXES		57
I	THE MICHELSON STELLAR INTERFEROMETER	59
	BASIC DEFINITIONS	60
	MUTUAL COHERENCE FUNCTION	60
	ANALYSIS OF FIZEAU INTERFEROMETER	62
II	COMPUTER PROGRAM FOR PIE-SHAPED SOURCES	65

TABLE OF CONTENTS (Cont'd.)

Appendixes		Page
III	SPECIFICATIONS FOR FRINGE DETECTOR	67
IV	GRATING MODULATION CHARACTERISTICS	71
	SQUARE-WAVE GRATING	74
	MOIRE FRINGE GRATING	78
	RELATIVE MERITS OF GRATINGS	78
	EXPERIMENT	79
	EXPERIMENTAL PROCEDURE	79
	DISCUSSION OF RESULTS	81

LIST OF ILLUSTRATIONS

Figure		Page
1	Fizeau Interferometer	3
2	Fringe Contrast $\lvert\gamma_{12}\rvert$ As A Function of Slit Separation	4
3	Corollary System to Grating Phototube Where Single Slit Is Inside Phototube	8
4	Schematic Diagram of Fringe Detector	10
5	Electronic Fringe Detector	11
6	Variable Separation Apertures	12
7	Square Wave Grating	15
8	Modulation Index for Single Slit	16
9	Entrance Aperture Configuration	17
10	Noise Output of Illuminated Phototube	20
11	Response of Type 53E/54E Plug-In Unit	20
12	Effect of Filter on Fringe Pattern	21
13	Number of Fringes in Envelope As Function of Aperture Separation	23
14	Correction Factor for Fringe Visibility As Function of Frequency	23
15	Signal-to-Noise Ratio for FC = 0.23 As Function of Slit Width	24
16	Slit Opening As Function of Measured Fringe Contrast for FC = 0, FC = 0.23	24
17	Measurement for $\Theta = 1.96 \times 10^{-5}$, X = 1.08 D (D = Slit Separation)	26
18	Measurement for $\Theta = 6.55 \times 10^{-5}$, X = 3.72 D (D = Slit Separation)	26

LIST OF ILLUSTRATIONS (Cont'd.)

Figure		Page
19	Measurement for $\Theta = 4.28 \times 10^{-5}$, $X = 2.43$ D (D = Slit Separation)	27
20	Measurement for $\Theta = 1.36 \times 10^{-4}$, $X = 7.64$ D (D = Slit Separation)	27
21	Fringe Contrast As Function of Slit Separation for Several Angular Source Sizes	28
22	Performance of Fringe Detector	29
23	Measurement of Angular Source Size for Various Source Brightnesses	30
24	Angular Size of Source As Function of Fringe Contrast for D = 0.67 cm	30
25	Notation of the van Cittert-Zernike Theorem	35
26	Intensity Distribution Over the Cone	38
27	Fringe Contrast $\lvert\gamma_{12}\rvert$ As Function of ω for $\alpha = 0^{\circ}$, $B'/B = 1$	40
28	Fringe Contrast $\lvert\gamma_{12}\rvert$ As Function of ω for $\alpha = 90^{\circ}$, $B'/B = 1$	41
29	Fringe Contrast $\lvert\gamma_{12}\rvert$ As Function of ω for $\alpha = 90^{\circ} \pm 5^{\circ}$, $B'/B = 1$	42
30	Fringe Contrast $\lvert\gamma_{12}\rvert$ As Function of ω for $\alpha = 0^{\circ}$, $B'/B = 10$	43
31	Fringe Contrast $\lvert\gamma_{12}\rvert$ As Function of ω for $\alpha = 90^{\circ}$, $B'/B = 10$	44
32	Fringe Contrast $\lvert\gamma_{12}\rvert$ As Function of ω for $\alpha = 90^{\circ} \pm 5^{\circ}$, $B'/B = 10$	45
33	Fringe Contrast $\lvert\gamma_{12}\rvert$ As Function of ω for $\alpha = 0^{\circ}$, $B'/B = 100$	46
34	Fringe Contrast $\lvert\gamma_{12}\rvert$ As Function of ω for $\alpha = 90^{\circ}$, $B'/B = 100$	47
35	Fringe Contrast $\lvert\gamma_{12}\rvert$ As Function of ω for $\alpha = 90^{\circ} \pm 5^{\circ}$, $B'/B = 100$	48
36	Micrograph of Pie-Shaped Source (100X)	49

LIST OF ILLUSTRATIONS (Cont'd.)

Figure		Page
37	Optical System Used to Transform Cone-Shaped Aperture	50
38	Enlarged Micrograph of Transform of Pie-Shaped Source	50
39	Experimental and Theoretical Results for $\|\gamma_{12}\|^2$ for $\varphi = 0^o$ . . .	51
40	Experimental and Theoretical Results for $\|\gamma_{12}\|^2$ for $\varphi = 90^o \pm 5^o$	52
41	Experimental and Theoretical Results for $\|\gamma_{12}\|^2$ for $\varphi = 90^o$ . . .	53
42	Schematic Diagram of the Michelson Stellar Interferometer . . .	59
43	Schematic Diagram of Fizeau Interferometer.	61
44	Electronic Fringe Detector, Front View	68
45	Electronic Fringe Detector, Top and Side Views	69
46	Overlap of Two Sinc Functions	73
47	Square-Wave Grating	75
48	Variation of Modulation Index vs Slit Width (2c), Slit Height (h), and Grating Length (L).	77
49	Experimental Setup.	79
50	Rotation of Grating vs Modulation Index	80
51	Sampling Aperture vs Modulation Index	81

SECTION I

INTRODUCTION AND SUMMARY

The purpose of this program was to study electronic methods of detecting fringes from a Michelson stellar interferometer and to relate these measurements to the characteristics of the source of illumination. The project objectives included: (1) the establishment of the feasibility of an electronic fringe detector, (2) the design, construction, operation, and testing of a prototype, (3) the determination of the best method for optimizing the fringe detector output, (4) the evaluation of atmospheric noise inputs, and (5) the evaluation of the use of the interferometer to analyze pie-shaped sources.

The specific type of Michelson stellar interferometer studied is called a Fizeau interferometer and consists of two apertures that produce a fringe pattern when illuminated by an incoherent source in the far field of that source. The fringe contrast can be directly related to the shape of the source and its distance from the detector by the van Cittert-Zernike[1] prediction of the mutual coherence function. This prediction holds only in the far field of the source.

Photographic and visual measurements of fringe contrast fail when the fringes vibrate because of image motion or atmospheric turbulence. Electronic fringe-contrast measurements are superior to visual and photographic measurements because the noise produced by fringe motion and other noise sources can be electrically filtered out of the signal. These electronic fringe-contrast measurements are accomplished by converting the intensity versus position relation of the fringe field to a voltage versus time relation through the use of a grating of the same frequency as the fringes which moves relative to the fringes. The transmission of the grating is monitored by a phototube that yields the desired voltage versus time signal.

For symmetric source distributions, the fringe contrast will vanish for particular separations of the input apertures. The usual determination of the angular source size relies on determining the zero contrast separation by visual examination of the fringe field. With electronic detection, this zero point must be determined by extrapolation since it represents a point of zero signal level. We have demonstrated this capability, and we have shown that the angular source can be predicted from a single measurement of the contrast function with an accuracy limited only by the available energy. This requires, of course, that the geometrical configuration and orientation of the source be known so that the general form of the coherence function can be predicted.

For this purpose a study was made of the mutual coherence function that will exist in the far field of a pie-shaped incoherent source. This was done for selected axes by a computer study and further verified experimentally by obtaining the optical Fourier transform of a pie-shaped source from which a full two-dimensional mapping of the coherence function could be deduced. The results show that high contrast levels can be expected only over small aperture separations and only along specific axes. This means that a relatively brighter pie-shaped source will be needed to achieve the accuracy represented by the axially symmetric sources studied under this program.

The electronic fringe detector operated well and its performance was in excellent agreement with the limitations predicted from energy and noise considerations. Its design necessarily involves some compromises, since an optimum device would have involved a level of effort incommensurate with the objectives of this contract. However, the operating characteristics of an improved device can be predicted from the same type of analysis which was successfully used on the experimental model.

The electronic fringe detector has several advantages over a single-mirror telescope. Fundamentally, of course, it can make size determinations beyond the diffraction limit of such a telescope. It is also less affected by atmospheric turbulence, image motion, and ambient background illumination, since these noise sources can be electrically filtered in the output of the electronic fringe detector.

In the pages which follow, the fundamental problems involved in constructing an operational instrument are first surveyed. The actual design selected is then described. The theoretical and experimental research carried out to select and evaluate design components follows. The fringe detector is then compared with the single-mirror telescope. Pie-shaped sources of uniform and nonuniform intensity are next considered. The final section discusses the results and conclusions of the entire program. The general theory of the Michelson stellar interferometer, the pie-shaped sources computer program, the component specifications for the fringe detector, and the theoretical investigation of gratings are given in the appendixes.

SECTION II

DESIGN CRITERIA

This section briefly discusses the principles of the Michelson stellar interferometer and relates these principles to the functions the fringe detector-interferometer must perform. It then describes the design criteria dictated by these functions. Because these functions are interdependent, the entire instrument had to be designed as a unit. For simplicity, we shall call this unit a "fringe detector." Alternate configurations are suggested for possible future development under "Other Systems Considered" (p. 7).

MICHELSON STELLAR INTERFEROMETER

The general theory of the Michelson stellar interferometer is given in Appendix I. For our purposes, this interferometer will be considered to be two slits, or entrance apertures, which combine with an optical system to focus a set of fringes at a distance from the optical system equal to one focal length, as shown in Figure 1. Here the width of the central envelope of the fringes is inversely proportional to the width of

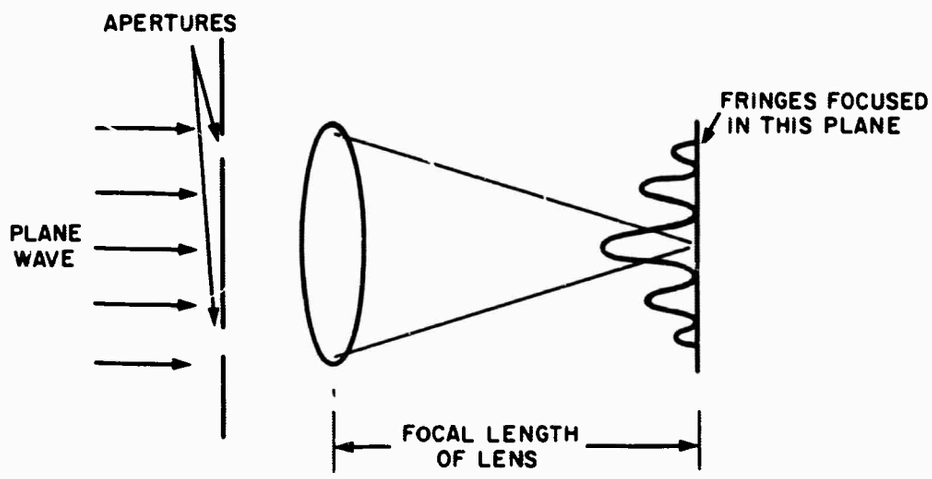

Figure 1. Fizeau Interferometer

one of the slits (when the two slits are of the same width), and the width of one of the fringes is inversely proportional to the slit separation. Thus, both the spatial fringe frequency and the number of fringes in the central envelope are proportional to the aperture separation. As the aperture separation increases for a circular source, the contrast of the fringes will decrease until the contrast reaches zero, as shown in Figure 2. For this source, this separation, called "extinction separation," is a measure of the angular size of an incoherent source in the far field of that source, where "angular size" means the simple angle the source subtends as viewed by the interferometer.

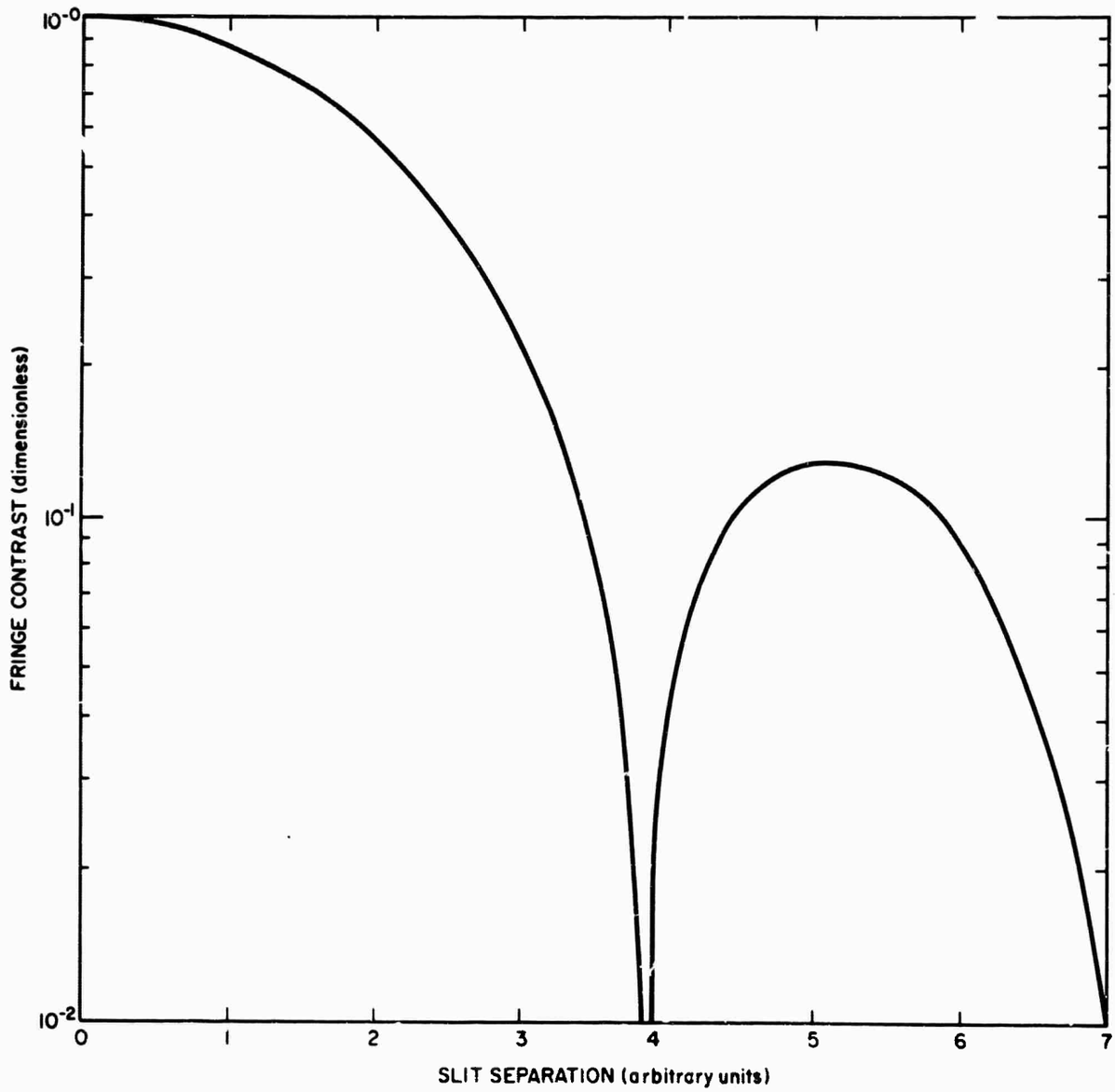

Figure 2. Fringe Contrast $|\gamma_{12}|$ As A Function of Slit Separation

For circular sources, the extinction separation varies inversely as the angular size of the source. Generally, for nonsymmetric sources, a well-defined extinction separation will not exist. The position of maxima and minima will, however, vary as the source is rotated. Thus, the object of this program reduces to studying electronically the inflections in the fringe pattern as a function of aperture separation and orientation.

GENERAL REQUIREMENTS FOR FRINGE DETECTOR

The fringe detector must perform two functions to determine the angular size of a source: (1) it must provide for measurements made at different slit separations, and (2) it must demodulate the fringe field to yield a measure of fringe contrast. This is obtained by measuring the values of the envelopes of the peaks, I_{max}, and the valleys, I_{min}, of the intensities of the fringe field at an arbitrary point in the field:

$$FC = \frac{I_{max} - I_{min}}{I_{max} + I_{min}} .$$

For our purposes, $I_{max} - I_{min}$ will be considered to be the strength of an ac signal riding on top of a dc signal given by $I_{max} + I_{min}$.

Let us now consider the design criteria developed to fulfill these functions.

DETECTION AND MEASUREMENT OF FRINGE CONTRAST

Several techniques were investigated to detect and measure fringe contrast: nonlinear surface detectors, measurement of intensity levels at a single value of I_{max} and a neighboring value of I_{min}, and conversion of the field by a spatial filter. The first two were rejected because they were less sensitive and less efficient than the third, which yields a continuous signal. For a continuous signal it is possible to filter out the noise from atmospheric sources. The net result is much better sensitivity. For these reasons this method was chosen, and several types of gratings were studied — cosine, square wave, and moire fringe (see Appendix IV). The square wave and the cosine grating of equal transmission were found to be roughly equivalent in their ability to demodulate the fringe field (the adjustment of the moire grating was too tedious to be practical). However, since the square wave grating was more easily obtained and fabricated, it was preferable to the cosine grating.

In demodulating the fringe field with a grating, the grating is placed in the plane of the fringes, and the grating and the fringes are moved relatively to each other in a direction perpendicular to the fringes in the plane of the fringes. This yields a time-varying transmission of the grating which is a function of the peak-to-peak intensity difference of the fringes, $I_{max} - I_{min}$. A measure of $I_{max} + I_{min}$ can be found by chopping the signal. The transmission of the grating is then monitored by a photomultiplier tube whose output can be studied by conventional techniques.

VARIABLE SEPARATION APERTURES

The entrance apertures of a Fizeau interferometer are generally either pinholes or parallel slits, since no other shape offers any particular advantage except for a unique application. Entrance apertures of finite size degrade the fringe contrast, because the fringes are a measure of the second-order correlations of the electromagnetic field amplitudes at two points. If the entrance apertures are of finite size, a true two-point correlation no longer exists. However, if the two pinholes are made very small, there is no degradation due to the finite sizes of the pinholes but no energy is transmitted. Therefore it is desirable to have the maximum possible aperture area with a minimum degradation of fringe contrast. The best way to do this is with a pair of parallel slits which are designed to keep fringe degradation constant as the slit separation is varied. A system was therefore selected whereby the height of the aperture was a constant percentage of the aperture separation. The energy per fringe would then be constant and independent of the aperture separation. This is useful for instrument calibration (see p. 22). (Deriving the optimum aperture height to maximize the signal ($I_{max} - I_{min}$)-to-noise ratio is a difficult problem requiring the use of a computer. Such a study would be necessary to design the optimum fringe detector.)

OPTICAL SYSTEM

Although a grating will provide greater instrument sensitivity than a slit, the optical system required for a grating proved to be impractical. Such an optical system (similar to a zoom lens system) would have to be capable of tuning the spatial fringe frequency to the grating frequency. Commercially available zoom lenses change focal length by a factor of 3 or less. This range is too small for our purposes. Also, zoom lenses usually suffer from pincushion or barrel distortion at the extreme focal length conditions. Other lens systems involve impractically large changes in optical path length. Thus, a simple lens system combined with a single detecting slit became the logical choice for the fringe detector.

CHOPPING AND BANDWIDTH

An additional problem is to select a method of moving the fringes at a constant velocity to obtain a narrow bandwidth, as well as to chop the beam to obtain a measure of $I_{max} + I_{min}$. The bandwidth considerations arise in transforming the spatial frequency of the fringe field to a time-varying signal as recorded by the phototube. The ambient noise of an unilluminated phototube is proportional to the square root of the frequency bandwidth and approaches the dark current noise as the bandwidth becomes large. Practical considerations generally limit the narrowness of the bandwidth to be employed. Therefore it was decided that a rotating reflector would not degrade the system's sensitivity in terms of bandwidth, since the reflector moves the equally spaced fringes by the slit at a constant velocity, which leads to a constant frequency output. The rotating reflector automatically provides chopping for a measure of $I_{max} + I_{min}$.

For a Fizeau interferometer of fixed focal length, it is clear that for a constant rotational speed of the reflector the frequency of the signal will change as the separation of the slits is changed. To increase the sensitivity of the instrument, an electrical filter must be used to filter out noise at frequencies other than the frequency of the signal. However, as the slit separation is increased, the signal frequency will increase by as much as a factor of 10 (for a slit separation variable by a factor of 10). In addition, since, at the widest slit separation, the fringe frequency is 100 times the frequency of the fringe envelope, a 100 cps bandwidth is required to retain the linearity of the system. Thus, a constant rotational speed of the reflector requires a 1000 cps bandwidth. With a 1000 cps bandwidth, the noise of the phototube can, at best, be improved by a factor of 30 over the dark current noise by means of filters. If the speed of the rotating reflector is changed to keep the signal frequency constant, a further reduction by a factor of 3 in the signal-to-noise ratio can be achieved by reducing the bandwidth to 100 cps. If only knowledge of the existence of fringes is required, possibly another factor of 3 improvement in the signal-to-noise ratio can be obtained by reducing the bandwidth to 10 cps. This, of course, requires careful adjustment of the speed of the rotating reflector as the slit separation is changed. Thus, a low-pass filter was selected, and the speed of the rotating reflector was adjusted to keep the fringe frequency at 100 cps.

REVIEW OF DESIGN PROBLEM

For a fixed focal-length system, a Fizeau interferometer generates a spatial fringe frequency that varies as the slit separation. To obtain a constant fringe frequency, the possibility of using a "zoom" lens system that changes focal length by a factor of 10 was considered but discarded, because the design of an appropriate zoom lens system that suffered from neither pincushion nor barrel distortion would be impractical. Other optical combinations to retain a constant fringe frequency would involve large changes in the optical path length. Thus, it became necessary to work with a fringe field with changing spatial fringe frequency. This led to the use of a single slit instead of a grating in front of the phototube to demodulate the field and to the use of a rotating reflector to provide linear fringe motion and chopping. The variable separation apertures were designed to maintain the aperture height at a constant percentage of the aperture separation. This facilitated calibration by keeping the energy per fringe constant and maintaining constant degradation of the fringe contrast due to the finite height of the slits.

OTHER SYSTEMS CONSIDERED

Several alternate system configuration were considered. While they may prove to be useful in an optimum system, they did not serve the objectives of this feasibility study. They are presented here to indicate possible courses of development for the design of components of an ultimate fringe detector. The performance of these configurations can be directly predicted from the results of this study.

A corollary to the grating phototube combinations selected is shown in Figure 3, where the single slit or grating is actually inside the phototube. Here the focusing coil generates a magnetic field which focuses the electrons coming off the photoemissive surface onto the plane of the grating. The electric field plates then deflect

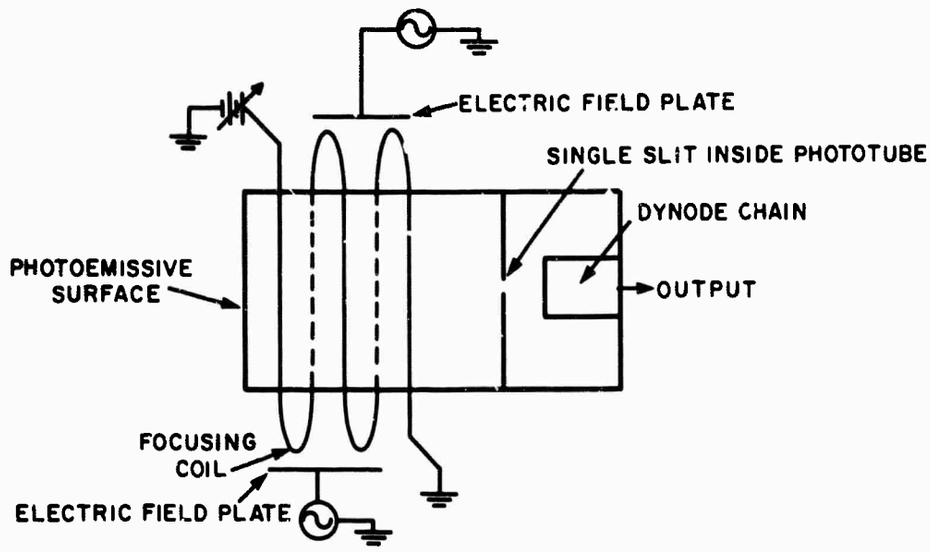

Figure 3. Corollary System to Grating-Phototube Where Single Slit Is Inside Phototube

the electrons so that the representation of the fringe pattern formed by the electrons is swept across the grating. The current transmitted by the grating is then amplified in the usual manner with further dynode stages. Intrinsically, this system is similar to the system where the phototube was placed behind the grating; however, the effective area of the photoemissive surface is equal to the area of the slit, since only the "dark current" electrons from that portion of the photoemissive surface focused on the slit are amplified by the dynode chain. This has the potential advantage of a better signal-to-noise ratio than the grating-phototube combination since the signal-to-noise ratio is, in general, inversely proportional to the square root of the cathode or photoemissive surface area. All the results of this effort can be applied directly to a specialized phototube once it has been designed and the noise figures determined.

Another corollary to the transmission grating system is a grating in the form of twenty-one concentric spirals that rotate in the plane of the fringe field. Here the fringes would be formed into a one-dimensional sine wave by a positive cylindrical lens. This one-dimensional sine wave would then be radially aligned with the spiral grating, and rotation of the spiral about its center would yield the desired modulated electrical signal proportional to the $I_{max} - I_{min}$. The $I_{min} + I_{max}$ component would be determined either by chopping the beam or through the use of a second channel. After obtaining bids on producing the spiral grating, this system was abandoned as being too costly and complex to be within the scope of this contract. However, this sytem has one very noteworthy advantage. If the measurement of fringe visibility is to be made over a long period of time, "lock-in amplifier" techniques may be used to obtain a very narrow bandwidth. In this case the signal-to-noise ratio would improve as $(t)^{1/2}$, where t is the time interval over which the measurement is made.

An optical method of improving sensitivity involves a square wave grating whose parallel members alternatively reflect or transmit the fringe pattern. Both the reflected and transmitted energy can be collected and electronically correlated. This will provide an effective improvement factor of a 2 in bandwidth.

A pair of long slits parallel to a cylindrical lens is an aperture-lens combination which produces a fringe pattern containing a larger amount of energy. This results in a tall fringe pattern (same height as slits) in a direction parallel to the slits. Under these conditions, alignment of the fringe field with a grating will constitute a severe problem. Thus, such a system does not appear practical if the slit separation is to be changed. Such a system may be useful, however, if only a single measurement of fringe contrast is required. Several such systems operating in parallel could provide measurements of fringe contrast at several conditions of aperture separation.

SECTION III

FRINGE DETECTOR DESIGN

This section describes the design of the fringe detector, as well as the general dimensions and the operating characteristics of the components. Construction details and the exact specification of the component parts are included in Appendix III.

CONFIGURATION AND OPERATION

The arrangement of the components of the electronic fringe detector is shown schematically in Figure 4. The components are mounted on a flat aluminum plate, approximately 36 in. by 14 in., that serves as the bottom of a light-tight box

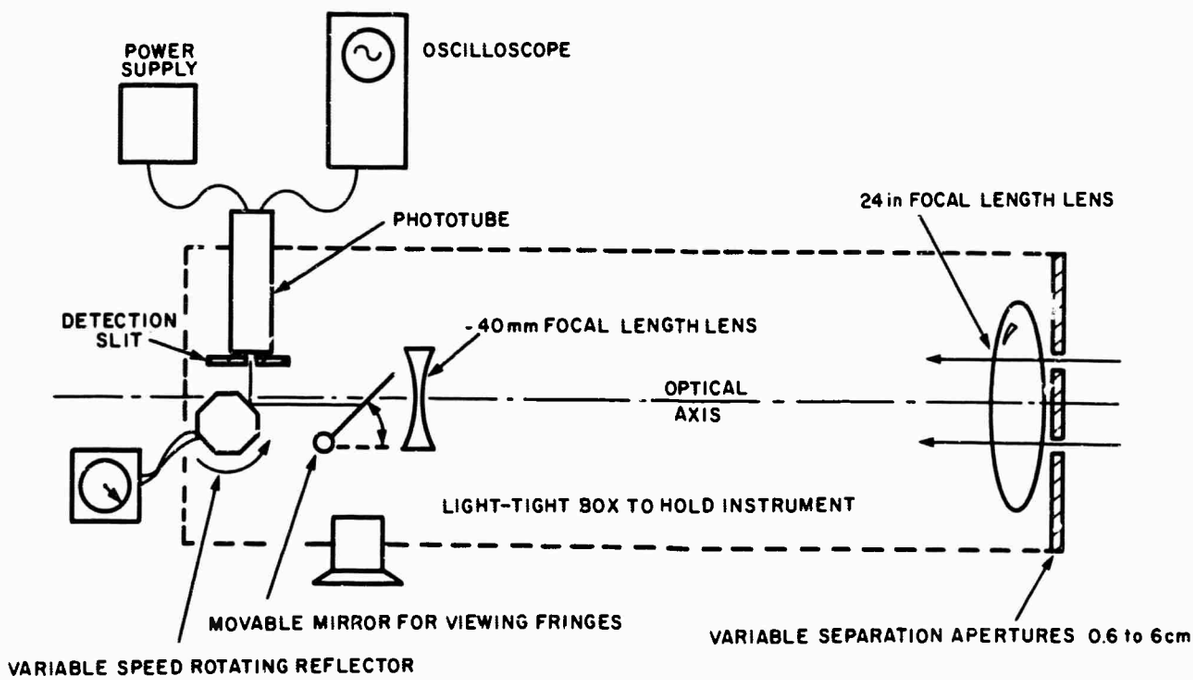

Figure 4. Schematic Diagram of Fringe Detector

approximately 36 in. long by 14 in. wide by 10 in. deep; light enters the system only through the entrance apertures. This light passes through the lenses and is reflected from one face of the rotating reflector onto the single slit in front of the phototube. In the plane containing the single slit, the light from the two apertures interferes and creates a spatial fringe field. If the reflector is rotating, the fringes pass by the slit and cause the light passing through the slit to vary as a function of the contrast of the fringe field, yielding a measure $I_{max} - I_{min}$ When the prism does not reflect light onto the slit, the base level of the fringes is determined, providing a measure of $I_{max} + I_{min}$. For the circular sources studied, the aperture separation for which the fringe contrast is a minimum is called the "extinction separation," and for a Michelson stellar interferometer it is a measure of angular source size. The second maximum of fringe contrast is located at approximately 1.3 times the extinction

separation. A mirror can be put into the optical path so that the fringes may be viewed in the eyepiece (see Figure 4). When the fringe field is centered in the eyepiece, the fringe detector is approximately aligned on target. Final alignment is made by viewing the output of the phototube on the oscilloscope. Here the spatial intensity distribution is observed as a voltage vs time relation. The fringe contrast is then determined by drawing envelopes of I_{max} and I_{min} on the picture of the scope trace. Since the envelopes constitute a graphical average over many fringes, the accuracy of this measurement is greater than the measurement of the contrast of a single fringe. In fact, the accuracy increases as the square root of the number of fringes sampled. These envelopes reduce the bandwidth inversely as the number of cycles included in the envelope. Since the signal-to-noise ratio is inversely proportional to the square root of the bandwidth, the effective signal-to-noise ratio is increased by the square root of the number of fringes sampled. Two views of the fringe detector are shown in Figure 5.

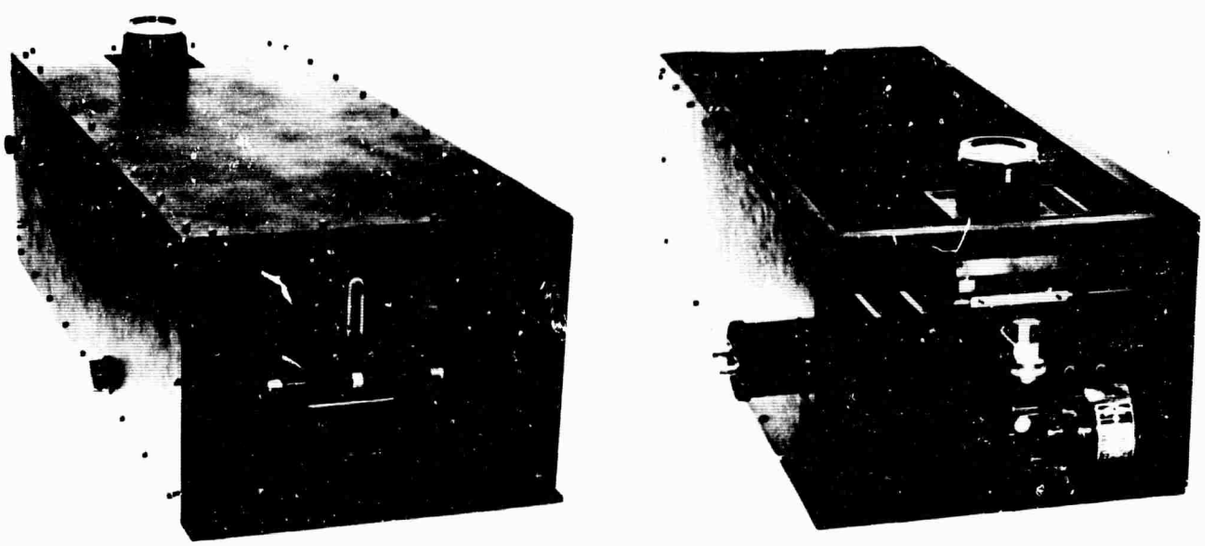

Figure 5. Electronic Fringe Detector

VARIABLE SEPARATION APERTURES

Entrance apertures 0.06 cm wide were constructed with separations manually variable from 0.6 to 6 cm. Provisions were made to maintain the aperture height at 0.1 times the aperture separation by means of triangular stops, as shown in Figure 6. For a Michelson interferometer, aperture separations from 0.6 to 6 cm

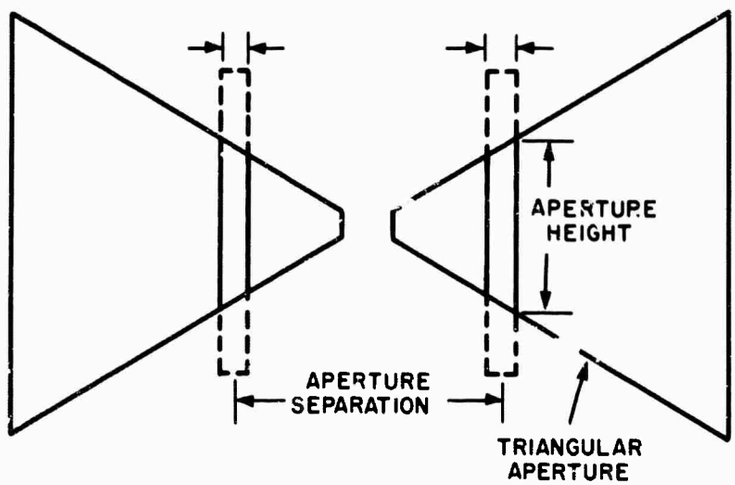

Figure 6. Variable Separation Apertures

cover a range of angular source sizes from 10^{-4} to 10^{-5} radians when viewing an optical wavelength of 5000 Å. The aperture height is maintained at 0.1 times the aperture separation so that the degradation of the fringe contrast due to the finite length of the aperture will not vary as a function of aperture separation. Since the aperture height increases linearly with aperture separation, the height of the fringe field decreases as the inverse of the aperture separation. Thus, for wide aperture separations, the fringe field is very short compared with the height of the slit in front of the phototube. This is helpful in maintaining the alignment of the fringes and the detecting slit.

OPTICAL SYSTEM

A 24 in. positive lens and a -40 mm negative lens were combined to produce a fringe field equivalent to that produced by a 200 in. lens with an optical path length of only 36 in. The fringe field was enlarged in order to adjust the spatial fringe frequency to practical dimensions so that alignment requirements would not be too severe. For the arrangement shown in Figure 5, the spatial fringe frequency in lines per millimeter is given by

$$SFF = \frac{d}{f\lambda} \approx 40\,d$$

where f is the effective focal length of the system (200 in.); λ is the source wavelength, chosen as 5000 Å in this example; and d is the aperture separation in centimeters. For aperture separations variable from 0.6 to 6 cm, the spatial fringe frequency will vary from 24 to 240 lines/min.

SILVERED ROTATING REFLECTOR

The reflector is an eight-sided silvered prism whose rotation is controlled by a variable speed motor to provide necessary frequency adjustment. As the aperture separation is increased, the fringe frequency increases. This frequency must be adjusted to remain in the bandpass of the electrical system, discussed below. The rotating reflector serves two additional functions: (1) it provides fringe motion across the single slit so that an ac signal related to the fringes can be recorded on the oscilloscope to give a measure of $I_{max} - I_{min}$; and (2) it also acts as a chopper, giving a measure of $I_{max} + I_{min}$. With this rotating reflector arrangement, the fringes pass by the slit at a constant frequency and do not increase the required bandwidth of the system.

SINGLE SLIT

In the fringe detector, the fringes are focused in the plane of the detection slit in front of the phototube. This slit is a standard interferometer slit with an adjustable width. As the entrance aperture separation is changed, the width of each fringe changes. Thus, to keep the demodulation of the fringes by the detection slit constant, the width of the slit must be adjusted each time the entrance-aperture separation is changed. The manner in which this slit-width adjustment is performed is discussed under "Instrument Calibration" (p. 22).

ELECTRONICS

The electronic system comprises the phototube, the electrical filter, and the oscilloscope. The phototube is placed behind the detection slit and monitors the transmission of light through it. The ac component of this light is proportional to $I_{max} - I_{min}$ and the dc component is proportional to $I_{max} + I_{min}$. The frequency of the ac component is proportional to the spatial fringe frequency, the rotational speed of the reflector, and the radial distance from the reflector to the single slit. Thus, as the spatial fringe frequency increases, the rotational speed of the reflector must be reduced to keep the frequency of the ac component within the bandpass of the filter. The filter is a simple low-pass filter constructed of active electrical components. Active components were chosen over passive components since, at the low frequencies involved (0 - 100 Hz), passive components proved inadequate. The capacitance and inductance values required were impractically large when matched to the output impedance of the phototube and the input impedance of the oscilloscope (both $10^6\ \Omega$). The exact form of the filter will be discussed under "Instrument Calibration" (p. 22).

SECTION IV

RESEARCH PROGRAM

This section describes the theoretical and experimental research undertaken to demonstrate the feasibility of the electronic fringe detector.

THEORETICAL RESEARCH

A principal problem in this effort was obtaining a method of demodulating the fringes and an optical system for the fringe detector which were mutually compatible. The first part of this section describes the manner in which a grating transforms the spatial intensity fluctuations of the fringe field into time intensity fluctuations suitable for monitoring with a phototube. The second part of this section is a sensitivity analysis which treats the fringe-detecting ability of the fringe detector as a whole in terms of the intensity provided by the angular source. This analysis was performed to define the areas in which the sensitivity could be improved. The theoretical results are in good agreement with the experimental results discussed immediately following.

THEORY OF SPATIAL FILTER

The conversion of the spatially distributed fringe field into a time-varying intensity can be performed by a spatial filter by moving the filter relative to the fringes in the plane of the fringes. Mathematically, this is equivalent to convolving the spatial filter with the fringe field. Since the fringe field is periodic in one dimension, the spatial filter is selected to be periodic in one dimension (i.e., grating). Letting x be position, ν_g the grating frequency, I(x) the fringe field, and v the relative velocity of the fringes and the grating normalized to the grating frequency, we obtain the transmitted intensity as a function of time I(t):

$$I(t) = \int_{-L}^{L} I(x)\, g\left(\nu_g x - vt\right) dx$$

where L is one half the length of the grating in a direction perpendicular to the fringes. The fringe field may be described in one dimension by

$$I(x) = I_o \left(1 + FC \cos \nu_f x\right)$$

where $I(x)$ is the intensity at any point x, I_o is the average intensity, FC is the fringe contrast with a value between 0 and 1, and ν_f is the spatial fringe frequency. In solving for I(t), we obtain an expression of the form

$$I(t) = K\left(1 + D \cdot FC \cdot \cos \nu t\right).$$

Here D is the modulation index, which is a function of the grating, and K is a constant proportional to I_o and the average transmission of the grating.

Based on such an approach, the theory of fringe demodulation by gratings — moire fringe, cosine, and square wave — was considered (see Appendix IV). The square-wave grating was selected as the best grating configuration. Here we extract the results of the theoretical treatment of the square wave grating and show how these results apply to the single detection slit.

SQUARE WAVE GRATING

Consider a square wave described by Figure 7 where $d = (\nu_g)^{-1}$. Let h be the height of the grating or the height of the fringe field, whichever is less, in a direction parallel to the fringes. Let L be the half-length of the grating or the length of the fringe field, whichever is less, in a direction perpendicular to the fringes. Let ϕ be the angular misalignment in radians between the grating and the fringes. Then the modulation index, D, is described by

$$D = \text{sinc}\left(L\left|\nu_f - \nu_g\right|\right) \text{ sinc}\left(h\,\phi\,\pi\nu_f\right) \text{ sinc}\left(\pi c \nu_f\right)$$

where sinc x = sin x/x.

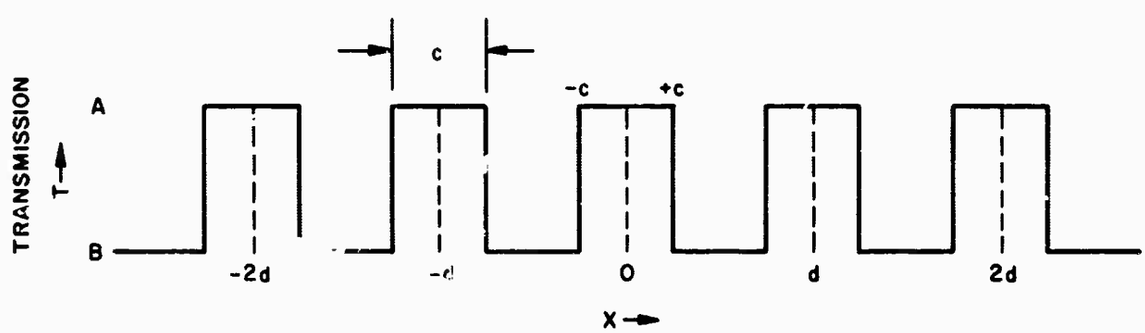

Figure 7. Square Wave Grating

SINGLE SLIT

The single slit is a degenerate case of the square wave grating. Here sinc $(L|\nu_f - \nu_g|)$ is no longer of interest. In the actual fringe detector constructed, alignment of the slit with the fringe field was not a problem, as discussed below "Detector Slit Width Considerations" (p. 22). Thus, the demodulation index is described by sinc $(\pi C \nu_f)$. The modulation index for a single slit is shown in Figure 8.

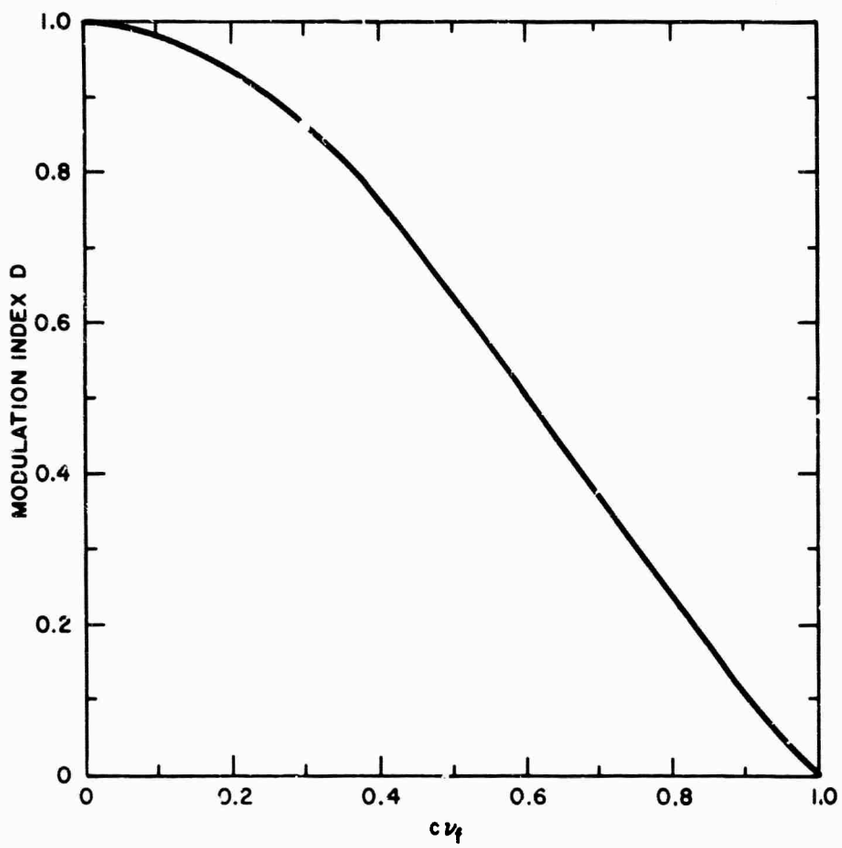

Figure 8. Modulation Index for Single Slit

SENSITIVITY CONSIDERATIONS

The usefulness of an electronic fringe detector is directly related to its sensitivity. The following analysis was performed to provide a better understanding of how the fringe detector should be constructed, as well as to point out the techniques for analyzing such an instrument.

The equivalent noise input, ENI, of a phototube is the noise in a 1 cps bandwidth measured at 1000 cps. In analyzing phototubes, the ENI is assumed to be independent of the frequency of the measurement for frequencies that do not approach the response limitations of the phototube. The ENI is multiplied by the square root of the bandwidth, ENI x $\sqrt{\Delta f}$, to obtain the dark current noise of the phototube. This noise is then approximately equivalent to the minimum signal that may be detected by the phototube at a signal-to-noise ratio of 1. Thus, for a single slit detector, an amount of energy equal to ENI x $\sqrt{\Delta f}$ is required in each fringe for detection at a signal-to-noise ratio of 1 with a fringe contrast of 1.

The entrance apertures to our system are described by Figure 9, where the aperture separation, d, is variable from 0.6 to 6 cm, the aperture height is always equal to 0.1 d, and the aperture width is equal to 0.06 in. Here, the fringe-field height is given by $F(h) = f\lambda/h$, the fringe-field width is $F(\Delta s) = f\lambda/\Delta s$, the distance between adjacent fringes is $F(d) = f\lambda/d$, and the portion of the energy in any one fringe is given by $F(d)/F(\Delta s) = \Delta s/d$, where f is the focal length of the system and λ is the mean wavelength of the light emanating from the source.

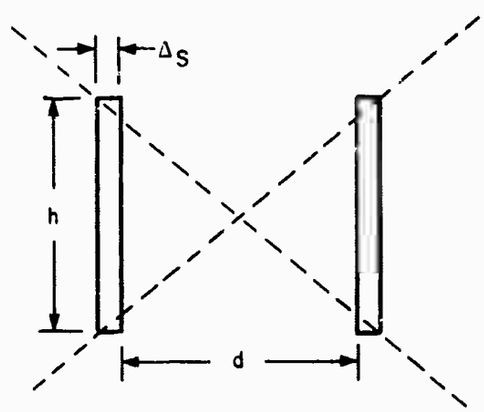

h = Aperture Height = 0.1 d

Δs = Aperture Width = 0.06 cm

d = 0.6 to 6 cm

Figure 9. Entrance Aperture Configuration

The total energy is proportional to the aperture height, h = 0.1 d, for our case. The energy in any one fringe is given by $(\Delta s/d) \times 0.1\,d = (0.1)\Delta s$ and is therefore independent of d. If the intensity in watts per centimeter squared incident on the two apertures is given, then the total energy entering the system is equal to the number of watts per centimeter squared incident on the system times the area of the two apertures in centimeters squared. The area of the two apertures is given by $A = 2(\Delta s)h = 0.2d\Delta s$. To get the approximate effective area for energy in an average fringe in the fringe envelope we multiply A by $\Delta s/d$

$$A_{eff} = 0.2\Delta s^2 = 0.2\,(0.06\text{ cm})^2 = 7.2 \times 10^{-4}\text{ cm}^2 \quad .$$

Thus, the energy density on the fringe detector required for the detection of fringes with a fringe contrast of 1 is

$$\text{Required energy density} = \frac{\text{ENI}\sqrt{\Delta f}}{0.2(\Delta s)^2} \times \frac{1}{D} \times \frac{1}{p}$$

where D is the modulation index of the single slit and p is the portion of the energy in a single fringe transmitted by the slit. The factor p is less than 1 because the width of the single slit is less than the total width of the fringe for an optimum signal-to-noise ratio.

In the fringe detector constructed (see "Instrument Calibration," p. 22) the optimum D was found to be equal to 0.8, at which point p was found to be 0.3. The ENI of the phototube used was measured and found to be equal to 4×10^{-15} watts. For the filter selected, Δf was equal to 250 cps. The width of the entrance apertures was equal to 0.06 cm. The minimum detectable signal was then calculated to be

$$\frac{4 \times 10^{-15}\sqrt{250}}{0.2\,(.06)^2} \times \frac{1}{68} \times \frac{1}{0.4}\ \frac{\text{watts}}{\text{cm}^2} = 2.8 \times 10^{-10}\ \frac{\text{watts}}{\text{cm}^2} .$$

The minimum detectable signal was measured to be 4×10^{-10} watts/cm^2 (see "Performance of Fringe Detector," p. 25) for a fringe contrast of 1 at a signal-to-noise ratio of 1. Two factors may account for the difference between the theoretically predicted and the experimentally measured values for minimum detectable signal. First, the losses in the optics were not taken into account. Second, the mercury arc lamp used in the experiment was not new and may have been degraded slightly from the manufacturer's specifications.

EXPERIMENTAL RESEARCH

The experimental work was concentrated on three problems – noise, instrument calibration, and the performance of the fringe detector. A large portion of the experimental research concerned obtaining the proper electrical filter for an acceptable signal-to-noise ratio. The problem of electrical noise was somewhat more involved than anticipated. It has become clear that almost all the fundamental problems encountered in constructing an electronic fringe detector are ultimately noise problems and may be treated as such. This includes not only the standard sources of electrical noise, but also the effects of atmospheric turbulence, fluctuations in source brightness, vibrations in the fringe detector, background illumination, and target motion. For the majority of our measurements, however, the noise limit was set by the shot noise in the phototube. Once an acceptable electrical filter was obtained, the calibration of the instrument and the evaluation of the performance of the fringe detector proceeded without delay.

SHOT NOISE FILTERING

The problem of designing an electrical filter involves many considerations: the filter must be compatible with the rest of the fringe detector, it must effectively filter the shot noise, and it must be useful in reducing the noise due to atmospheric influences on the system and the source. The problems involved in filtering shot noise can best be understood by examining the various filter techniques attempted. It is important to keep in mind that the shot noise increases as the square root of the bandwidth.

Initially, the output of the phototube was filtered by connecting a variable capacitor between the output of the phototube and ground. While this clearly reduced the noise output of both the illuminated and unilluminated (dark current) phototube, it made the fringe contrast so highly dependent on the frequency of operation, as determined by the rotational speed of the reflector and the variable aperture separation, that any attempt to calibrate the instrument proved fruitless. A 200 cps high-pass filter and a 1500 cps low-pass filter were then connected between the output of the phototube and the oscilloscope. These LC filters had a $10^4\,\Omega$ input and output impedance, constituting an impedance mismatch with both the output impedance of the phototube and the input impedance of the scope, which were $10^6\,\Omega$. Calculation indicated that impedance matching was impossible with passive elements at frequencies less then 1500 cps, since the L and C values required would be impractically large. In spite of this, it was hoped that this approach would lead to an acceptable solution, but the results were disappointing. The combination oscillated so badly that under certain conditions it was difficult to tell one fringe envelope from another, much less resolve the individual fringes. The impedance matching problems were solved by using a General Radio tuned amplifier in series with the LC filters while setting the amplifier to a flat response; however, this provided little improvement in the performance of the LC filter. When the tuned amplifier was employed as a pass-band filter for the output of the phototube, the system still oscillated.

The tuned amplifier approach has another inherent limitation. If the amplifier is tuned to the fringe frequency, the envelope is at the wrong frequency and thus the envelope height cannot be simultaneously measured. If the pass band is made broad enough to include both the frequency of the fringes and the envelope frequency, the system will have a large noise figure. This is in contrast to the low-pass filter, in which the pass band can be made arbitrarily small and still include both the envelope and the fringe frequency. On the basis of these results, the tuned amplifier approach was abandoned in favor of operating the device at a low frequency with a single low-pass filter.

To properly match the impedances, a filter with active components was selected. Using the tuned amplifier, we measured the noise spectrum of the illuminated phototube and obtained the results shown in Figure 10. The filter response of the low-pass filter of a type 53E/54E Tektronix plug-in unit is shown in Figure 11. On the basis of these curves, we selected the 250 cps filter to attenuate the noise. This filter gave the best signal-to-noise ratio obtained, at least a factor of 8 better than any pass-band filter tried. One attractive feature of this filter is its nearly linear response below 100 cps. As was determined in "Instrument Calibration," (p. 22) 100 cps is approximately the minimum operational frequency of our system for conditions of wide aperture separation. Scope traces of a fringe pattern with a fringe contrast of 0.4 are shown with and without the 250 cps filter in Figure 12 to demonstrate the effect of the filter.

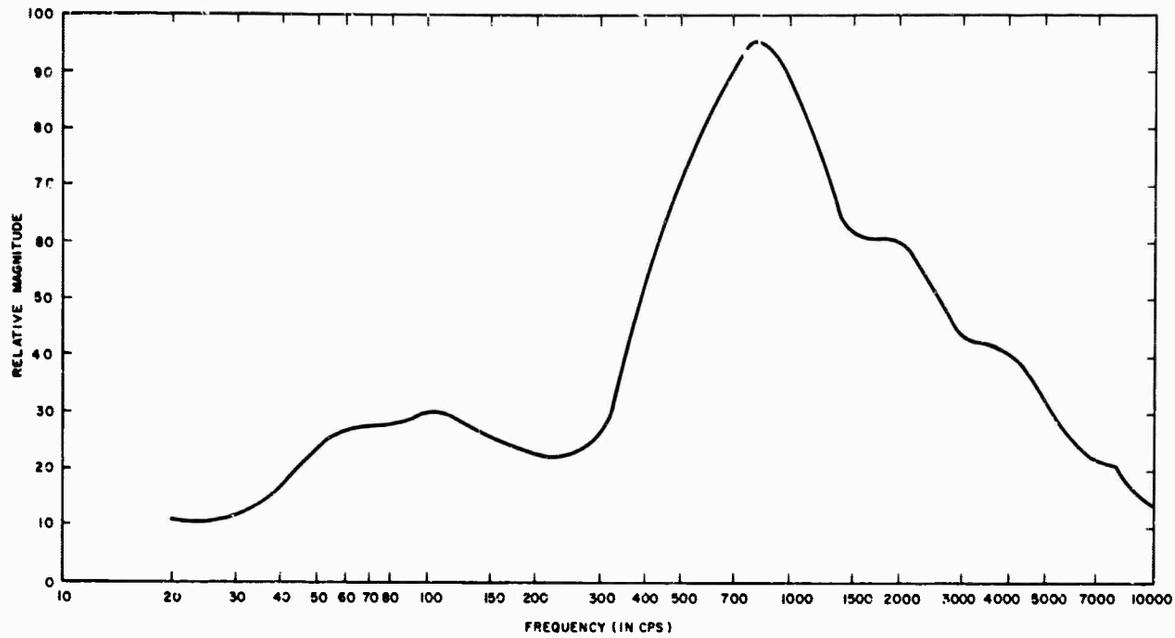

Figure 10. Noise Output of Illuminated Phototube

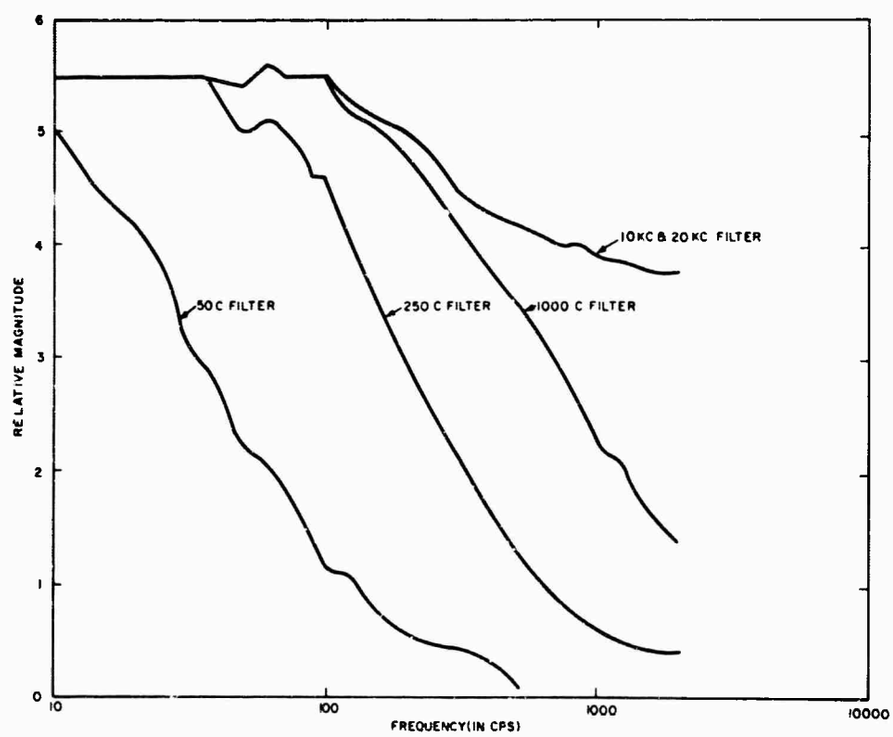

Figure 11. Response of Type 53E/54E Plug-In Unit

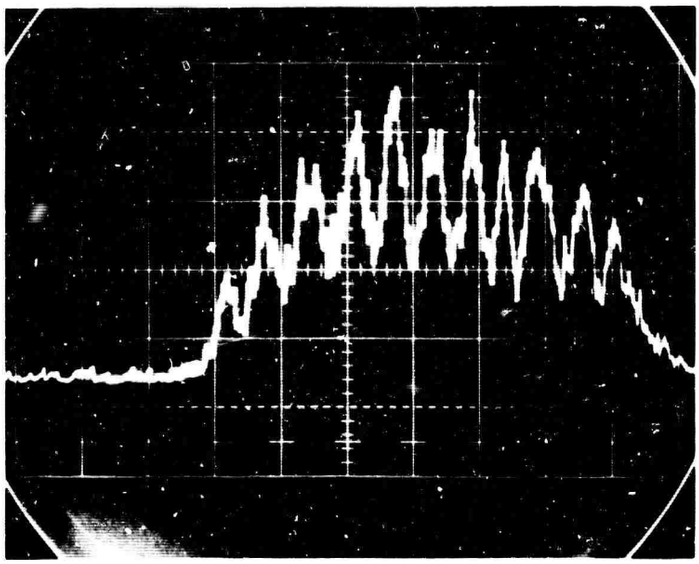

Fringes with Filter

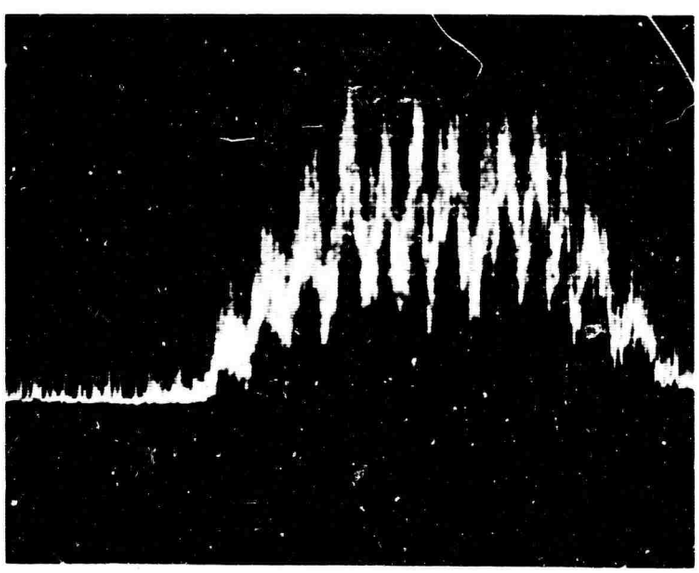

Fringes without Filter

Figure 12. Effect of Filter on Fringe Pattern

INSTRUMENT CALIBRATION

Frequency-Bandwidth Considerations

In accordance with the 250 cps filter response shown in Figure 11, the rotational speed of the rotating reflector was adjusted so that the frequency of the fringes was always below 100 cps. The measured frequency ranges possible with this reflector and the results obtained are shown in Table I (where D is the aperture separation).

TABLE I

FREQUENCY RANGE OF FRINGE DETECTOR

Condition	Minimum Frequency (cps)	Maximum Frequency (cps)
D = 0.67 cm	10	1,700
D = 6.0 cm	90	15,000
Envelope	0.8	156

The frequency was determined by measuring the time width of the fringe envelope and combining this with the number of fringes in the envelope. We measured the number of fringes in the envelope as a function of aperture separation and the results are shown in Figure 13. The correction factor for the 250 cps filter in the measurement of fringe visibility is shown in Figure 14 and is simply the inverse of the filter response curve.

Detector Slit-Width Considerations

Since the spatial-fringe frequency changes as the inverse of the separation of the entrance apertures, it is necessary to vary the width of the detection slit in front of the phototube accordingly. To keep the modulation index of the slit constant, its width must vary inversely with the separation of the entrance apertures.

Figure 15 shows the signal-to-noise ratio as a function of slit width, measured in arbitrary units, proportional to the height of the envelope of fringes, as measured in volts on the oscilloscope face. Over a large range of slit widths, the signal-to-noise ratio remained fairly constant but dropped sharply as the slit width was increased. We made all the measurements at the 21 point on the arbitrary scale, which was fairly easy to find and which gave an accurate reading of the fringe contrast. Figure 16 shows data similar to that in Figure 15 except that the actual measured values of fringe contrast are plotted instead of the signal-to-noise ratio. Measurements were made at D = 0.67 cm and D = 1.06 cm, where the actual fringe contrasts were 0.23 and 0, respectively. The measurement of fringe contrast at D = 1.06 cm is actually a measurement of the noise level.

In calibrating the detection slit, the best signal-to-noise ratio was found to occur when the fringe demodulation was greater than 0.8, at which point 30% of the energy in one fringe is transmitted through the slit, as determined by measurement. Operating under these conditions, we needed very little correction for the fringe demodulation to measure the actual fringe contrast.

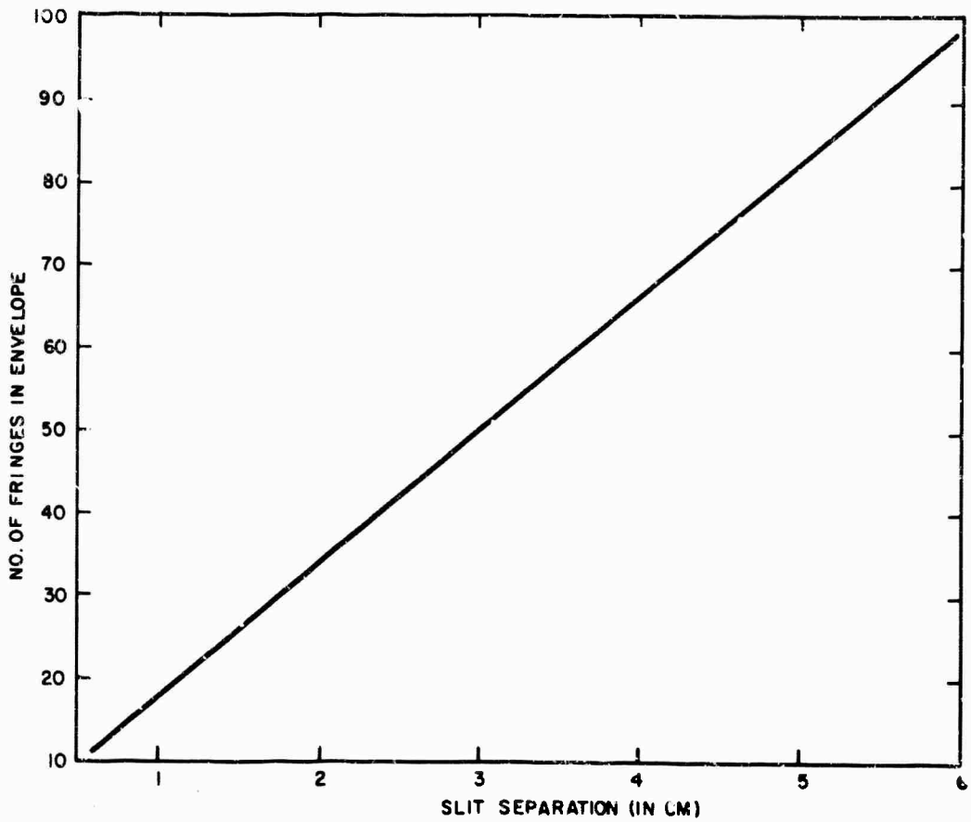

Figure 13. Number of Fringes in Envelope As Function of Aperture Separation

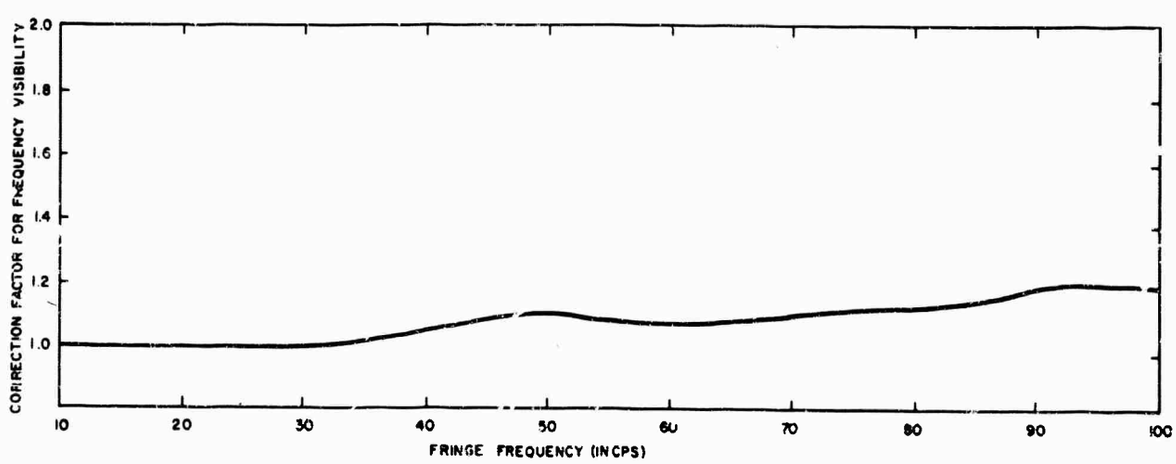

Figure 14. Correction Factor for Fringe Visibility As A Function of Frequency

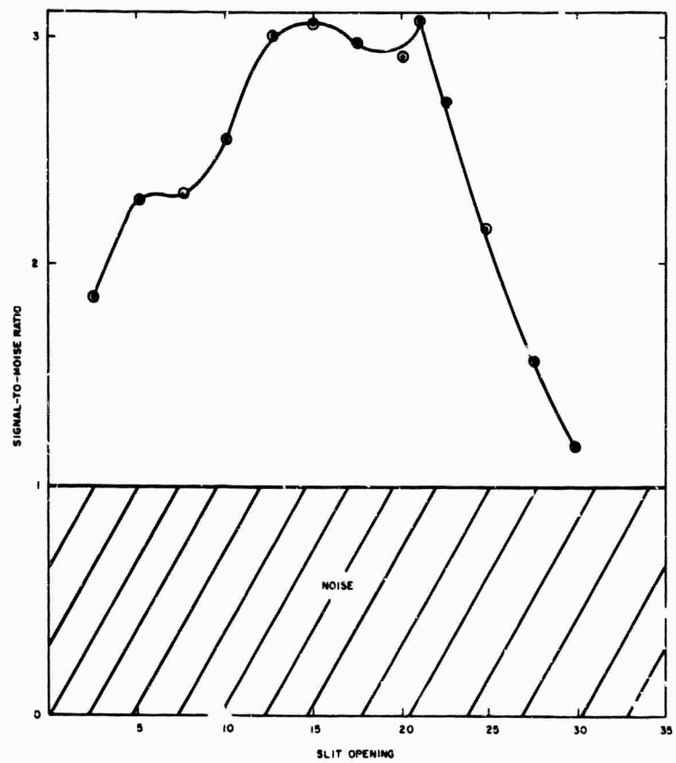

Figure 15. Signal-to-Noise Ratio for FC = 0.23 As Function of Slit Width

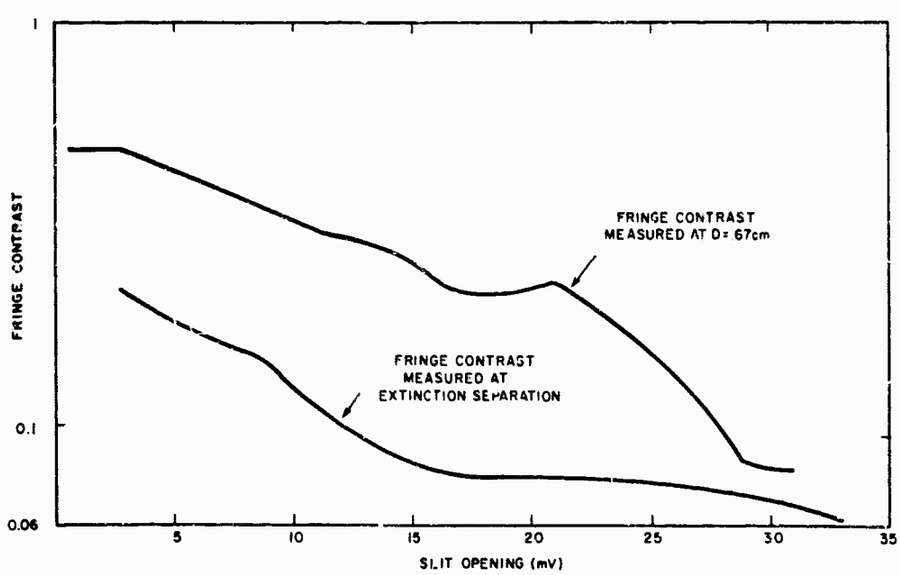

Figure 16. Slit Opening As Function of Measured Fringe Contrast for FC = 0, FC = 0.23

Since the height of the entrance aperture increases linearly with the aperture separation, the energy per fringe remains constant. Thus, the detection slit width was adjusted to keep the envelope height on the scope face constant, thereby keeping constant the ratio of detecting slit width to fringe width. This enabled the operator to keep the fringe demodulation constant as a function of entrance aperture separation (fringe frequency).

The height of the fringe field in a direction parallel to the fringes is inversely proportional to the height of the entrance apertures. Thus, since the height of the apertures increases linearly with their separation, it follows that the height of the fringe field varies inversely as the spatial fringe frequency. In other words, the product of the spatial fringe frequency times the height of the fringe field is a constant. In the theoretical section, the demodulation error due to misalignment between the fringe field detection and the slit was shown to be a function of this product. Thus, the alignment error does not depend on the spatial frequency in this instrument. In actual practice, it was observed that the detection slit could be easily and accurately aligned with the fringes when the lowest fringe frequency was used. Thus, alignment of the single slit with the fringe field did not constitute a problem.

PERFORMANCE OF FRINGE DETECTOR

Measurement of Angular Source Sizes

Collimated light from a lens-pinhole combination was used to obtain sources with angular dimensions suitable for use with the interferometer. Lenses with focal lengths of 48 in. and 15 in. were used in various combinations with a 25μ and a 52μ pinhole to yield source sizes of 1.96×10^{-5}, 4.28×10^{-5}, 6.55×10^{-5}, and 1.36×10^{-4} rad. The results of measuring these sources are shown in Figures 17-20. Figure 21 combines all the measurements of angular source size on a single scale for comparison. As the source size (intensity) increases, the point of fringe extinction separation becomes more clearly defined because the larger sources are brighter and, hence, the signal-to-noise ratios are better. For the 6.55×10^{-4} rad case, the data started on the second maximum of fringe contrast. The measured fringe contrast is lower than the theoretical value near the first maximum because the fringe contrast is degraded by the finite size of the entrance apertures, and the demodulation of the fringes by the detection slit is less than 1. In the region near the first maximum, noise was generally not significant. At the second maximum, the measured fringe contrast was high because of the contribution of the noise to the measured signal. The false fringe contrast measured at extinction separation is a measure of the noise level of the system.

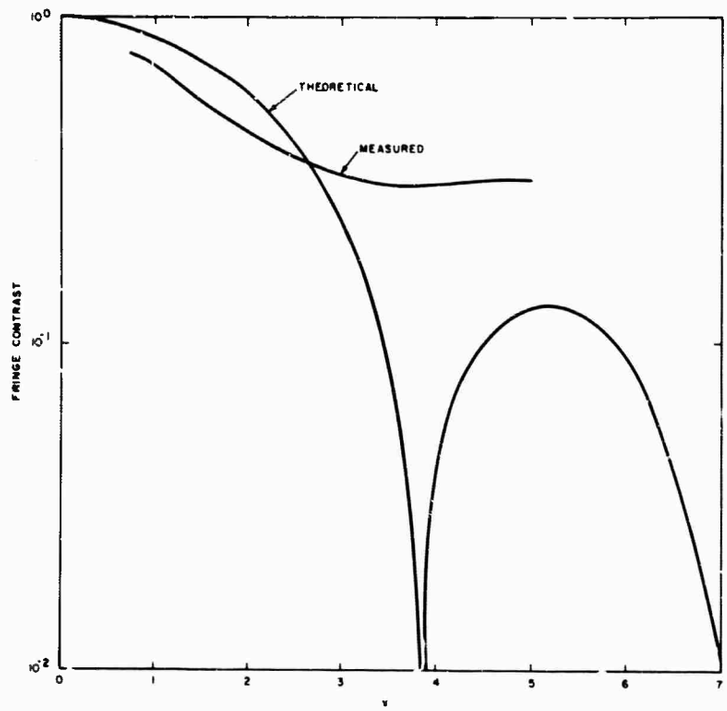

Figure 17. Measurement for $\Theta = 1.96 \times 10^{-5}$, $X = 1.08$ D
(D = Slit Separation)

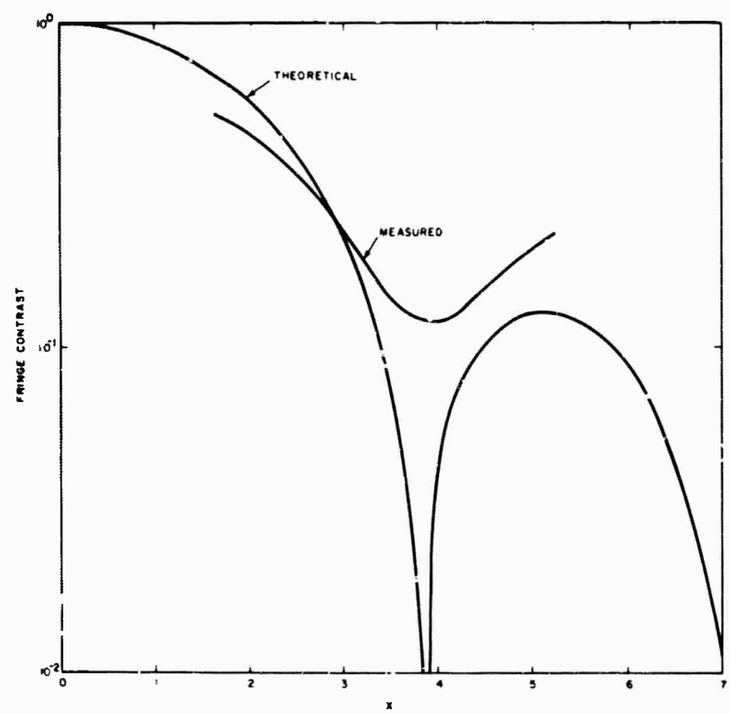

Figure 18. Measurement for $\Theta = 6.55 \times 10^{-5}$, $X = 3.72$ D
(D = Slit Separation)

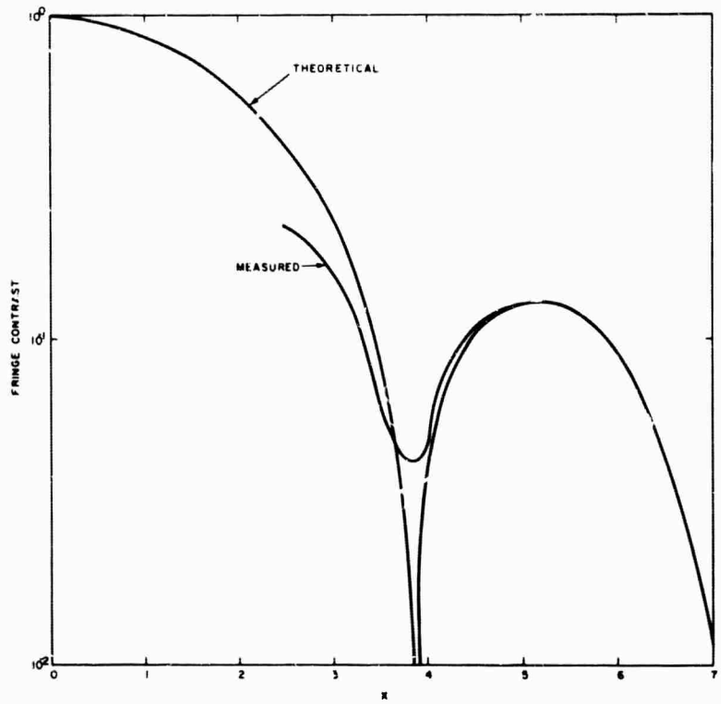

Figure 19. Measurement for $\Theta = 4.28 \times 10^{-5}$, $X = 2.43$ D
(D = Slit Separation)

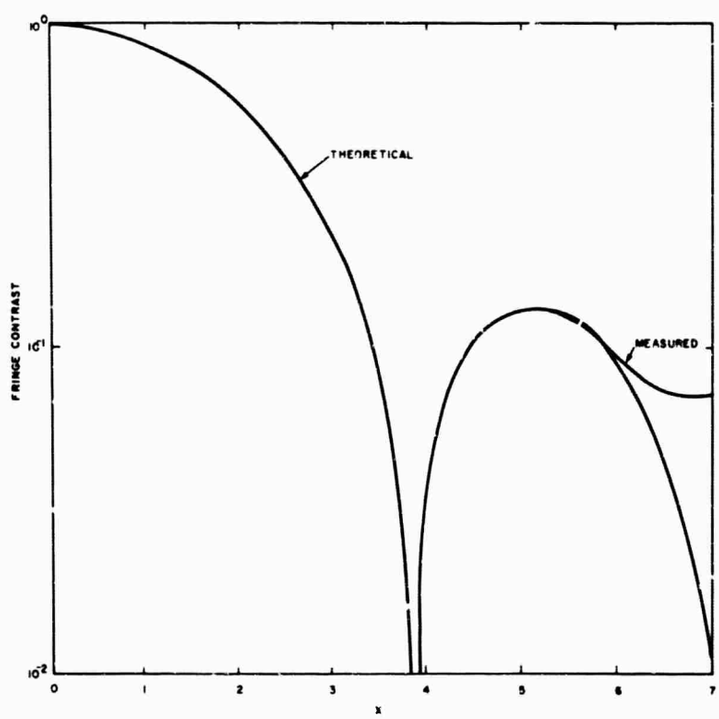

Figure 20. Measurement for $\Theta = 1.36 \times 10^{-4}$, $X = 7.64$ D
(D = Slit Separation)

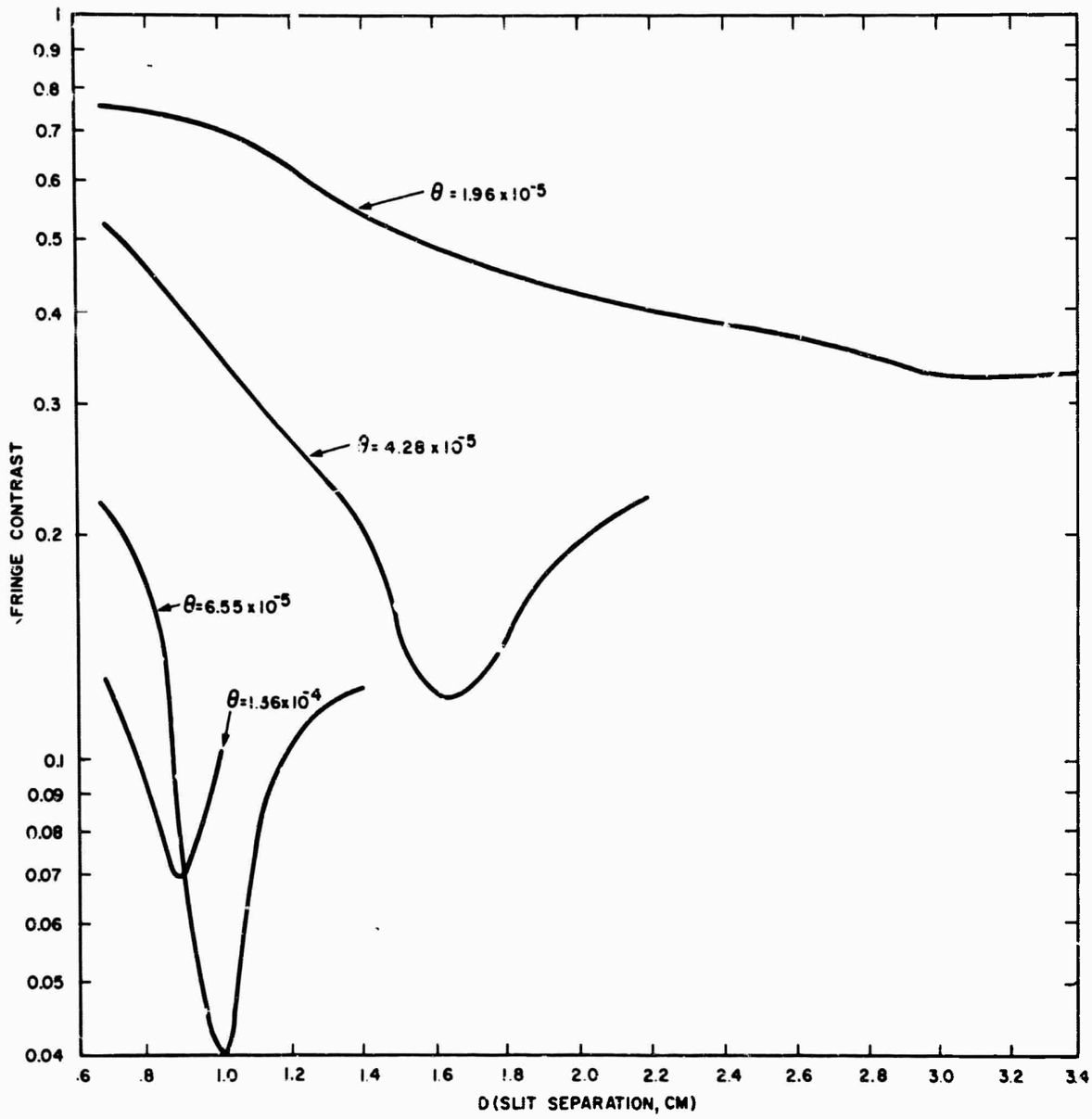

Figure 21. Fringe Contrast As Function of Slit Separation for Several Angular Source Sizes

DETECTION CAPABILITIES OF FRINGE DETECTOR

For the measurements made, the signal-to-noise ratio can be shown to be

$$\frac{S}{N} = \frac{FC\sqrt{S_e}}{k\sqrt{\Delta f}}$$

where FC is the fringe contrast, S_e is the signal of the envelope, and k is a constant of the phototube in question. Using this formula we plotted the solid line in Figure 22 as a prediction of the noise level for each level of incident radiation in watts per centimeter squared. We derived this from the known brightness of the mercury arc source as specified by the manufacturer and from the noise level at extinction separation for the 1.96×10^{-5} source. This noise level is the fringe contrast in watts per centimeter squared that can be detected at a signal-to-noise ratio of 1. Any combination of fringe contrast and watts per centimeter squared lying in the upper right-hand part of the graph can be detected with this system. The circled data points are the noise levels for various intensities measured with different-sized sources. These data points seem to be in excellent agreement with the predicted curve. To further support these data, we studied the 6.55×10^{-5} source with 0.3, 0.8, and 1.6 neutral density filters in front of the source (see Figure 23). The results here are also shown as circled points in Figure 22. The dotted line in the first graph represents what can be done with the best available phototube (cooled, and so forth), which would be about a factor of 20 better than our tube.

Figure 24 shows the fringe contrasts at D = 0.67 cm measured for various-sized sources. This demonstrates that the angular source size can be predicted from a single

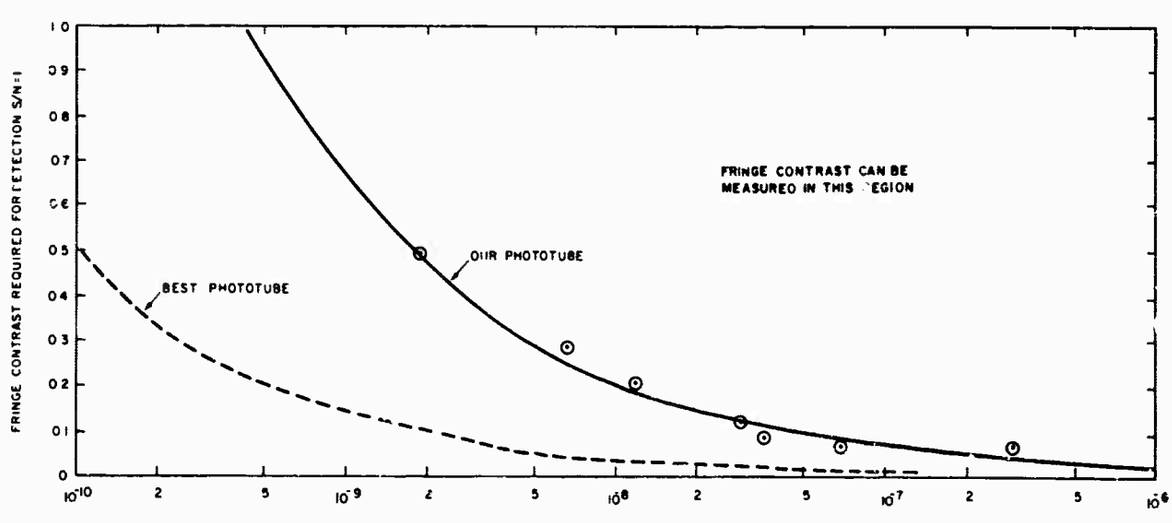

Figure 22. Performance of Fringe Detector

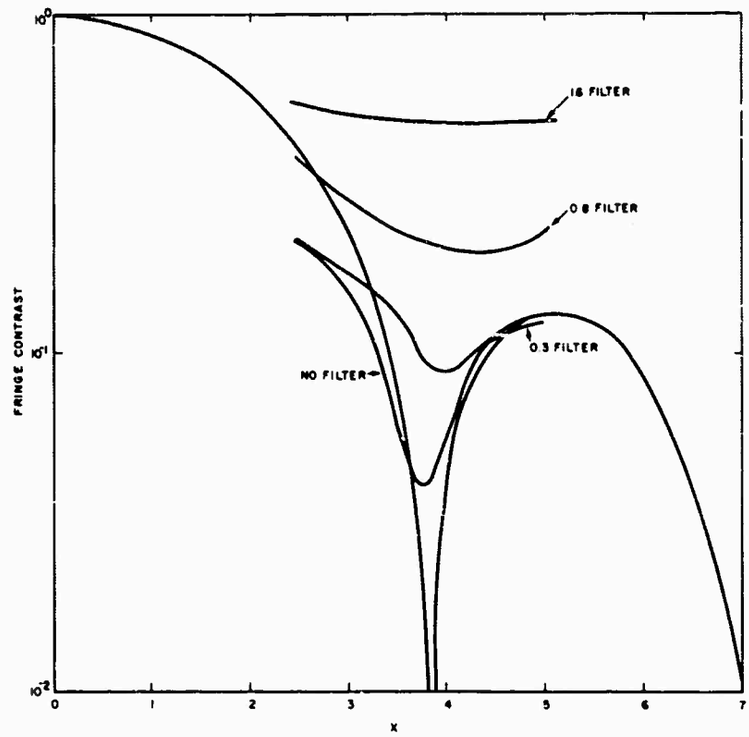

Figure 23. Measurement of Angular Source Size for Various Source Brightnesses

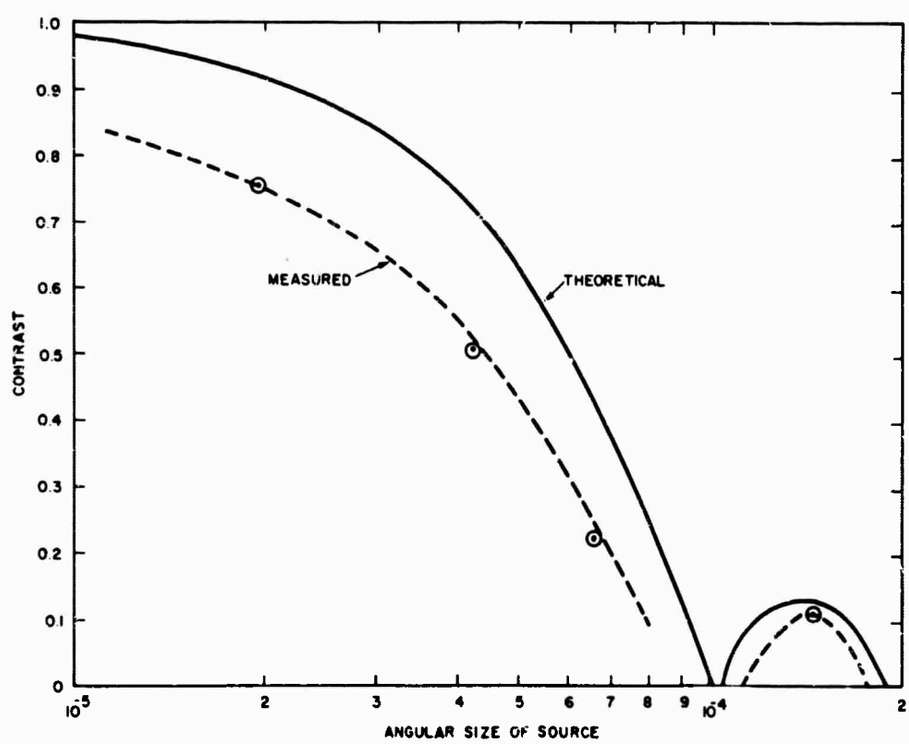

Figure 24. Angular Size of Source As Function of Fringe Contrast for D = 0.67 cm

measurement of fringe contrast. This, of course, allows the use of a fixed aperture separation and, hence, a constant spatial fringe frequency, which in turn would lead to improved sensitivity for the instrument since a grating could be used instead of a slit.

Outside Noise Sources

The five types of outside noise sources considered are atmospheric turbulence, vibration or movement of the detector, image motion, brightness fluctuations in the target, and background illumination.

Atmospheric turbulence, movement of the detector, and image motion are similar in that they all produce phase modulation of the ac signal coming out of the phototube. All three sources of noise cause apparent image motion, which causes the fringe field to move about on the slit. The frequency and amplitude of this unwanted fringe motion is transformed by the rotating reflector and the detection slit into a phase modulation of the signal. The bandwidth of the fringe detector with respect to these phase modulations, however, is much less than the quoted value of 250 cps because of the manner in which the fringe contrast was measured. As previously discussed, the fringe contrast given by the oscilloscope trace is determined by locating the envelope of I_{max} and I_{min} and measuring the fringe contrast from this envelope rather than trying to resolve the contrast of single fringes. There is no direct way in which the phase modulation can affect the envelope of the amplitude of the ac signal, although phase modulation can affect the apparent contrast of a single fringe. An alternative way to look at this problem is to note that since the envelope is an average of 10 to 100 cycles of the 100 cps signal (depending on aperture separation) the actual bandwidth of the system is 25 to 2.5 cps rather than 250 cps. Since this bandwidth is so narrow, phase modulation noise is generally negligible. To verify this, artificial turbulence produced by a hot wire and a high-pressure gas nozzle were used to introduce turbulence. Although the fringes could not be seen with the viewing eyepiece because of the vibration of the fringe field, the measurements of a 6.55×10^{-4} radian source both at a fringe contrast of 0.4 and at extinction separation agreed within experimental error with the measurements made when no turbulence was present.

Fluctuations in brightness of the source are a nonlinear source of noise, since the signal-to-noise ratio is proportional to the square root of the source brightness. Brightness fluctuations will also create false fringes in that the dc signal output of the phototube will change with the source brightness fluctuations. It is clearly possible for source brightness fluctuations of the proper frequency to generate a fringe pattern where the fringe contrast is actually equal to zero. This production of apparent fringes may be combatted by discrimination techniques that independently monitor the brightness of the source with a second channel and electronically correct the fluctuating intensity of what should be the dc part of the signal coming from the phototube. The fluctuating signal-to-noise ratio will still be present, however, and will contribute to inaccuracies in the measurement related to those frequency components of the fluctuating signal that are within the electrical bandpass of the system. Since the shot noise is proportional to the square root of the source brightness, and since the shot noise increases the apparent fringe contrast in this type of measurement, the minimum fringe contrast which may be

measured when using discrimination techniques will fluctuate with the source brightness. The effective bandwidth for this type of noise can be reduced to 2.5 cps in the same manner as the phase fluctuations if the discrimination techniques employed are sufficiently accurate. These changes in shot noise have been verified experimentally by varying the intensity of the light source with neutral density filters as discussed under "Performance of Fringe Detector" (p. 25). There the signal-to-noise ratio was observed to vary as the square root of the source brightness as described above.

Background illumination introduces noise in the form of an increase in the dc component of the signal and an increase in the shot noise of the phototube. The increase in the dc signal is proportional to the background illumination. The increase in the dc component can be compensated in the same manner as the fluctuating source intensity with an additional channel to monitor the background illumination. This additional channel can also compensate for fluctuating background illumination. The increase in shot noise has the apparent effect of increasing the equivalent noise input (ENI) of the phototube, thus reducing the sensitivity. Designing the fringe detector with the smallest detecting area consistent with other requirements limits the field of view of the instrument and, hence, reduces the effects of background illumination to a minimum. Both of these effects of background illumination were well established during the experimental phase of this program.

SECTION V

COMPARISON OF TELESCOPE AND INTERFEROMETER

This section reviews the known advantages of the single-mirror telescope and the Michelson stellar interferometer and defines those parameters that must be measured to establish the relative usefulness of each type of instrument, with particular attention to adverse atmospheric effects.

Although a single-mirror telescope can obtain the same information as the interferometer, the interferometer has several advantages. The most obvious is in the measurement of sources whose image is smaller than the diffraction limit of the telescope. In this case no measurement can be made by the telescope. The interferometer has no such limit and could therefore measure the angular size and position of any incoherent source. The mechanical stability or energy losses of a particular instrument might, however, dictate a practical lower limit on angular size.

In the common range of measurement, the interferometer is again advantageous when the measurement must be made through a turbulent medium such as the atmosphere because the effects of the medium on the interferometer are of a different character than those on the telescope. We can broadly divide the atmospheric effects into three categories: 1. fluctuations of image intensity, 2. fluctuations in the image size, and 3. fluctuations in the apparent position of the image. These variations are characterized by their amplitude and frequency distribution.

Fluctuations in the intensity represent a fluctuating signal for both instruments. In the interferometer, a signal from an independent observation of the source intensity could be coupled to the instrument amplifier gain and could thus maintain the output signal level. We must now distinguish two cases to determine the overall effect. If the instrument is lim[illegible] noise from the signal, then the signal-to-noise ratio will not be affected and the feedback loop will compensate for the brightness variation. If the instrument is limited by background noise, either dark current or ambient illumination, then the signal-to-noise ratio will not be constant and the feedback loop will maintain the signal at the expense of introducing a fluctuating noise component. The net result in this case will be an increase in the effective noise if the fluctuations are within the measurement bandwidth, otherwise they will be filtered out. In the telescope the measurement accuracy will be maintained unless the fluctuations are either of such magnitude, or occur at such a rate, as to cause operator fatigue.

Changes in apparent image size are due to distortions in the wavefront as it transverses the medium. These changes allow only a measurement of the average size. The interferometer is not susceptible to this difficulty directly but will be affected by changes in the correlations of the fields at a pair of points. It is difficult to compare the relative magnitudes of these effects, since relatively little information is available on the latter problem.

Changes in the apparent image position can be caused by either the turbulent medium or improper tracking. The problem is one of relative motion, and the discussion of the effects applies for either cause. In the interferometer, this motion causes undesirable variations in the signal level. Only those variations whose frequencies are within the bandwidth of the instrument will affect its performance and constitute an additional source of noise. In the telescope, both the frequency and amplitude of the fluctuations will affect the degree of degradation and, since no filtering is available, no measurement can be made if the fluctuations have components faster than the resolution time of the eye.

A final effect of atmospheric transmission is the loss of contrast with range. Since the ambient level does not depend on the target range, this loss of contrast reflects a loss in signal energy. This energy is unavailable regardless of the type of instrument used.

In order to establish the relative usefulness of the two instruments, atmospheric-induced source motion, reduction in spatial coherence, ambient background illumination, and brightness fluctuations must be studied. For a proper comparison, tracking accuracy must also be considered.

SECTION VI

INVESTIGATION OF PIE-SHAPED SOURCES

The method of measuring angular sizes of small circular sources with a Michelson stellar interferometer (by measuring the beam separation for which the fringe contrast goes to zero) is well established.[1] However, while a similar analysis may be applied to pie-shaped sources, it is considerably more complicated because of the rotational asymmetry of the source and other factors such as orientation and a nonuniform intensity distribution. Hence, this investigation was undertaken to determine the feasibility of using a Michelson stellar interferometer to study pie-shaped sources. In particular, calculations of the fringe contrast or equivalent $|\gamma_{12}|$ were made and experimentally verified.

THEORY

In a Michelson stellar interferometer, partially coherent quasi-monochromatic illumination from a small distant source falls upon two small apertures placed at P_1 and P_2 (Figure 25).

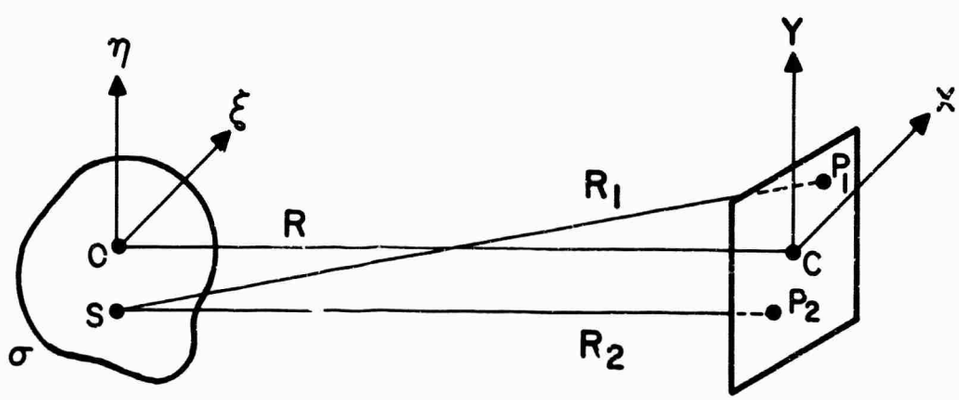

Figure 25. Notation of the van Cittert-Zernike Theorem

The two beams when brought together form cosine interference fringes (see Appendix I) of the form

$$I_1 + I_2 + 2\sqrt{I_1 I_2}\,|\gamma_{12}(o)|\cos 2\frac{kdy}{f} \qquad (1)$$

where I_1 and I_2 represent the intensity of the source falling on P_1 and P_2, respectively, and $\gamma_{12}(o)$ is the complex degree of coherence of the two light beams at P_1

and P_2 ($\gamma_{12}(o)$ will subsequently be referred to as just γ_{12}). The fringe contrast (FC) defined by

$$FC = \frac{I_{max} - I_{min}}{I_{max} + I_{min}} \tag{2}$$

is equal (for $I_1 = I_2$) to $|\gamma_{12}|$. Hence, as the aperture separation is varied, $|\gamma_{12}|$ may be mapped out for all pairs of points P_1 and P_2 along a given line associated with some particular angle of orientation of the source. As will be shown, $|\gamma_{12}|$ inherently depends upon the source characteristics (i.e., size, shape, orientation, and overall intensity distribution) and, hence, varies significantly for circular and pie-shaped sources.

Theoretically, $|\gamma_{12}|$ may be calculated by application of the van Cittert-Zernike theorem. According to this theorem, if the linear dimensions of the source and the separation of the points P_1 and P_2 are small compared with the distance of these points from the source, the degree of coherence $|\gamma_{12}|$ is given by the absolute value of the normalized Fourier transform of the intensity distribution over the source.[1] Using the notation of Figure 25, we may write $|\gamma_{12}|$ as follows

$$\gamma_{12} = \frac{e^{i\psi'} \iint_\sigma I(\xi,\eta)\, e^{-ik(p\xi + q\eta)}\, d\xi\, d\eta}{\iint_\sigma I(\xi,\eta)\, d\xi\, d\eta} \tag{3}$$

where

$(\xi,\eta) \equiv$ coordinates of a point in the source plane

$(x,y) \equiv$ coordinates of a point in the plane of P_1 and P_2

$\psi' \equiv$ phase differences $2\pi(R_1 - R_2)/\bar{\lambda}$

$p \equiv (x_1 - x_2)R$

$q \equiv (y_1 - y_2)R$.

When considering sources with circular symmetry it is easier to write Eq. (3) in polar coordinates. Making the substitutions:

$$\begin{aligned} \xi &= \rho \cos \Theta & p &= \omega \cos \varphi \\ \eta &= \rho \sin \Theta & q &= \omega \sin \varphi \end{aligned} \tag{4}$$

yields

$$\gamma_{12} = \frac{e^{i\psi'} \int_{o}^{a} \int_{-\delta/2}^{\delta/2} I(\rho, \Theta)\, e^{-ik\rho\omega \cos[\Theta - (\varphi + \phi)]}\, \rho d\rho d\Theta}{\int_{o}^{a} \int_{-\delta/2}^{\delta/2} \rho d\rho d\Theta} \tag{5}$$

where a is the radius of the cone and δ the cone angle. The denominator when evaluated is equal to $a^2\delta/2$. Note that in this equation ϕ represents the angle of orientation shifted from φ.

Early in the program, attempts were made to evaluate Eq. (5) in closed form for $I(\rho, \Theta) = c$. (The Fourier transforms of some cone shaped objects are known[2,3] but do not include the cases of interest, i.e. a 10° cone of varying intensity distr[illegible]s.) Whereas a circular source yields a simple expression independent of orientation, Eq. (5) becomes an infinite series of the form

$$\begin{aligned}\gamma_{12} = c\, e^{i\varphi'} \Bigg[& 2 \frac{J_1(ka\omega)}{ka\omega} + \frac{1}{\phi} 2 \sum_{n=1}^{\infty} (-1)^n \sin n\phi \cos 2n(\delta + \varphi) \times \\ & \sum_{k=0}^{\infty} \frac{2n + 2k + 1}{(n + k)(n + k + 1)} \frac{J_{2n + 2k + 1}(ka\omega)}{ka\omega} \\ & - \frac{1}{\phi} 4i \sum_{n=0}^{\infty} (-1)^n \sin\left(\frac{2n + 1}{2}\right) \phi \cos (2n + 1)(\delta + \varphi) \times \\ & \sum_{k=0}^{\infty} \frac{r(n + k + 1)}{(2n + 2k + 1)(2n + 2k + 3)} \frac{J_{2n + 2k + 2}(ka\omega)}{ka\omega} \Bigg]\end{aligned} \tag{6}$$

where $J_n(ka\omega)$ denotes a Bessel function of order n.

Because of the complexity of the integral in Eq. (5) and, alternately, the above closed form solution, we were forced to use a computer to evaluate $|\gamma_{12}|$. In this context it appeared somewhat easier and definitely more accurate to program the

original integral. It should be noted that the latter solution contains infinite series of Bessel functions which do not converge very rapidly, and considerable error would probably result from truncating the series to fit the limitations of computer time. Furthermore, numerical evaluation of Bessel functions is also a more lengthy process by computer. The advantage of choosing a straight integral approach is further heightened when proceeding from the case of uniform illumination to the case of zones of varying intensity.

Hence, one aspect of this program has been the design of a computer program to calculate $|\gamma_{12}|$ for a pie-shaped source as a function of size, shape, orientation, and distribution of intensity from Eq. (5), which will be discussed in more detail in the next section. To verify the computer results, an analog experiment was performed by optically viewing the Fourier transform of a pie-shaped source in a coherent diffraction system.

COMPUTER CALCULATIONS

For computer calculating purposes, the integral of Eq. (5) may be replaced by a summation over i and j of the intensity at the discrete points (ρ_i, Θ_j),

$$\gamma_{12}(\omega, \alpha) = \frac{a^2\delta}{2} e^{i\psi'} \sum_{1=1}^{M} \sum_{j=1}^{N} I\left(\rho_i, \Theta_j\right) e^{-ik\rho_i\omega \cos\left(\Theta_j - \alpha\right)} \rho_i \Delta\rho_i \Delta\Theta_j$$

where α equals $\varphi + \phi$, the angle of orientation of the cone axis with respect to a line joining the two apertures.

In the following calculations, a constant intensity distribution is assumed in the Θ direction across the source, so that $I(\rho_i, \Theta_j)$ becomes simply $I(\rho_i)$. The distribution in the radial direction was divided into three segments (Figure 26), each of

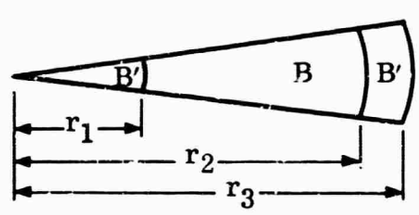

Figure 26. Intensity Distribution Over the Cone

constant intensity. The quantities B and B′ as functions of the radii r_1, r_2, and r_3 therefore define the nonuniform intensity distribution. The radii r_1 and r_2 were fixed at 1/40 r_3 and 39/40 r_3, respectively, and the cone angle at 10°. The ratio of the relative intensities B′/B were given values of 1, 10, and 100. Once the cone angle is fixed, a change in r_3 by a constant A will inversely change the scale of $|\gamma_{12}|$ to ω/A.

In dealing with computer programs, one is always faced with the problem of whether the input and/or output data is being sampled sufficiently. In the case of taking a Fourier transform with x and y coordinates in the source plane and coordinates p and q in the transform plane, the sampling theorem[4] is an adequate guide. Then

$$p_{max} = \frac{1}{2\Delta x}$$
$$q_{max} = \frac{1}{2\Delta y} \quad . \tag{7}$$

The maximum values of p and q that can be accurately calculated in the transform plane are thus simply related to the sampling intervals of the input data. A similar relation has been developed by Gabor[5] for the case where the areas of interest in the source and transform planes are circular and the intensity in the source may be represented by a summation of Bessel functions. Gabor's result is not applicable to the present approach (Eq. (5)) and hence a rough estimate of (7) was applied by letting Δx and Δy equal the largest sampling distances used, corresponding to $r_3\Delta\Theta$. The largest value of ω which can then be accurately calculated is more than adequate for all angles of α.

The following graphs, Figures 27 to 35, represent $|\gamma_{12}|$ (normalized) for the noted values of cone orientation (α), and ratio of the intensities of the segments (B′/B). The fringe contrast (or $|\gamma_{12}|$) is plotted in each case as a function of the generalized coordinate, ω, which is equal to the aperture separation times a normalization constant R/r_3. For details of the computer program, see Appendix II.

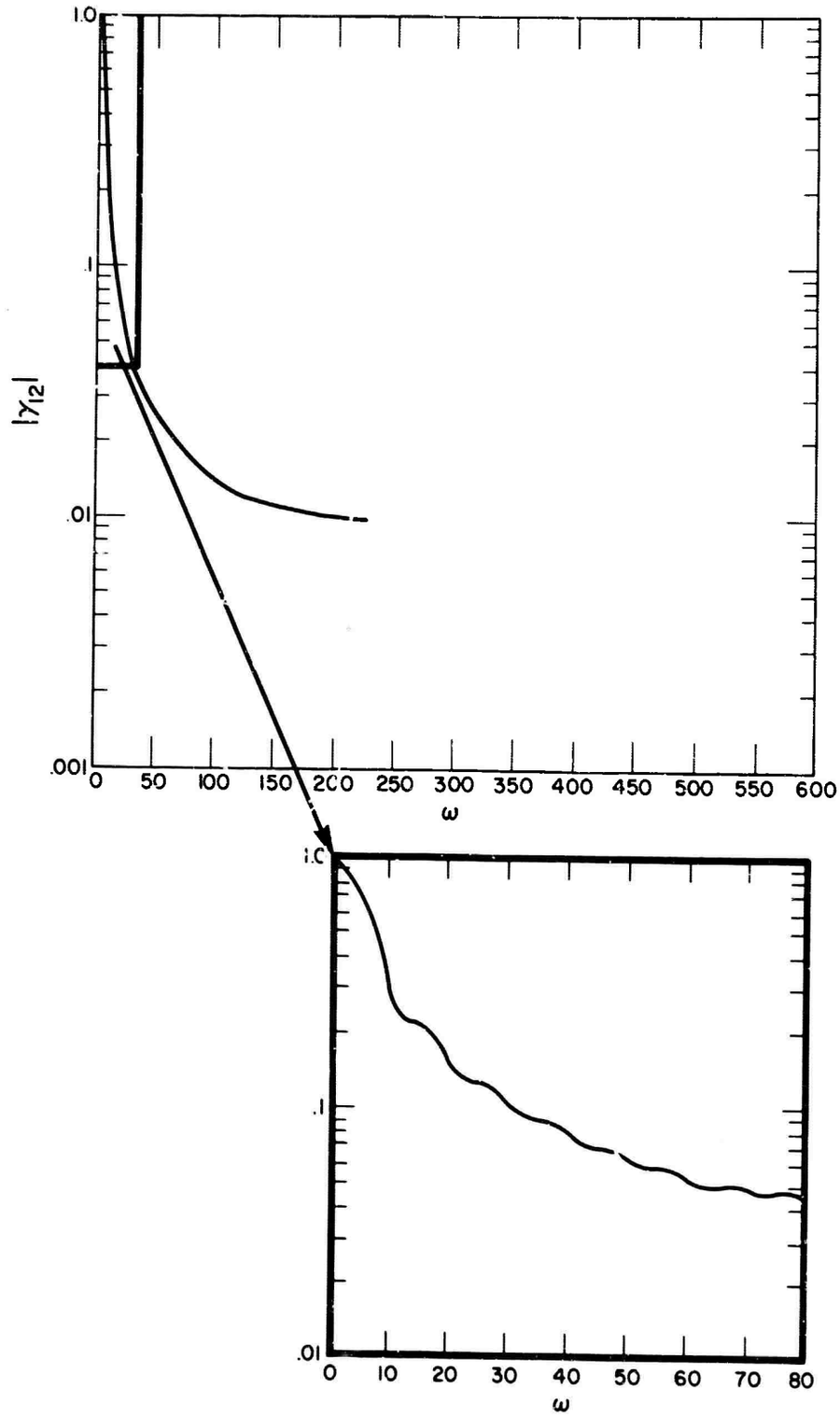

Figure 27. Fringe Contrast $|\gamma_{12}|$ As Function of ω for $\alpha = 0^{o}$, $B'/B = 1$

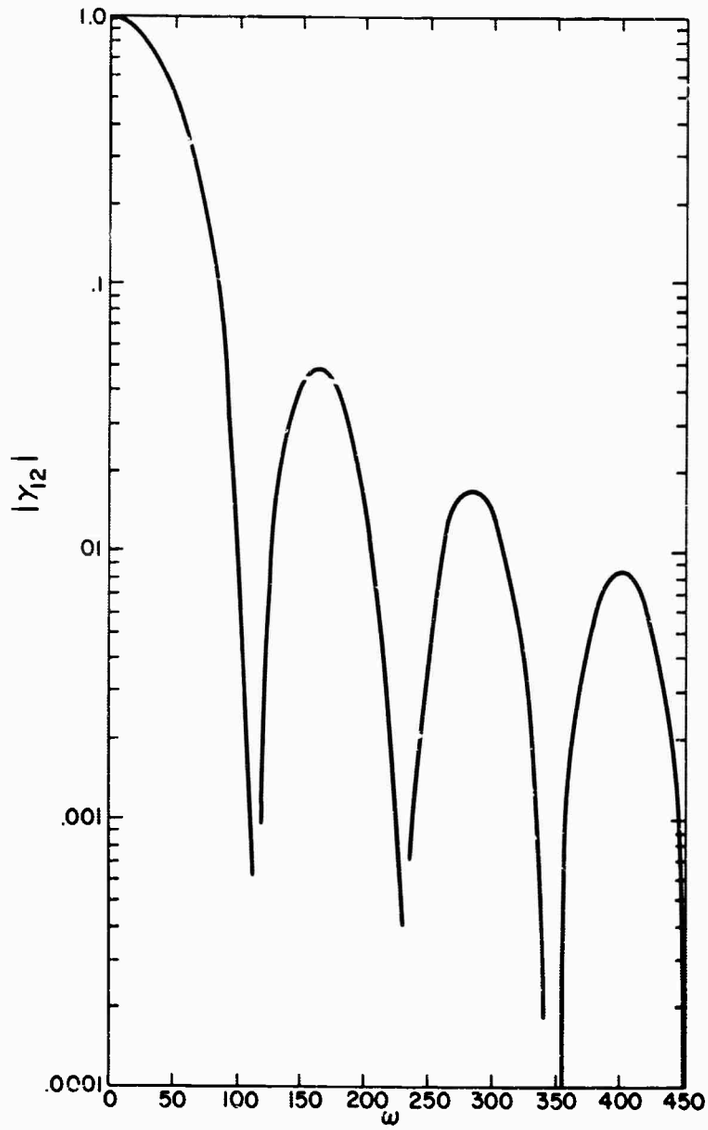

Figure 28. Fringe Contrast $|\gamma_{12}|$ As Function of ω for $\alpha = 90^{\circ}$, $B'/B = 1$

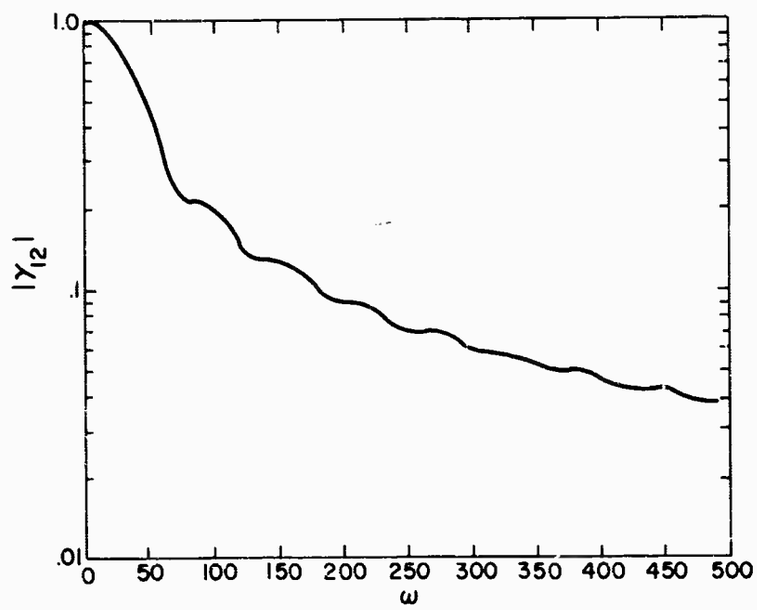

Figure 29. Fringe Contrast $|\gamma_{12}|$ As Function of ω for $\alpha = 90^{\circ} \pm 5^{\circ}$, $B'/B = 1$

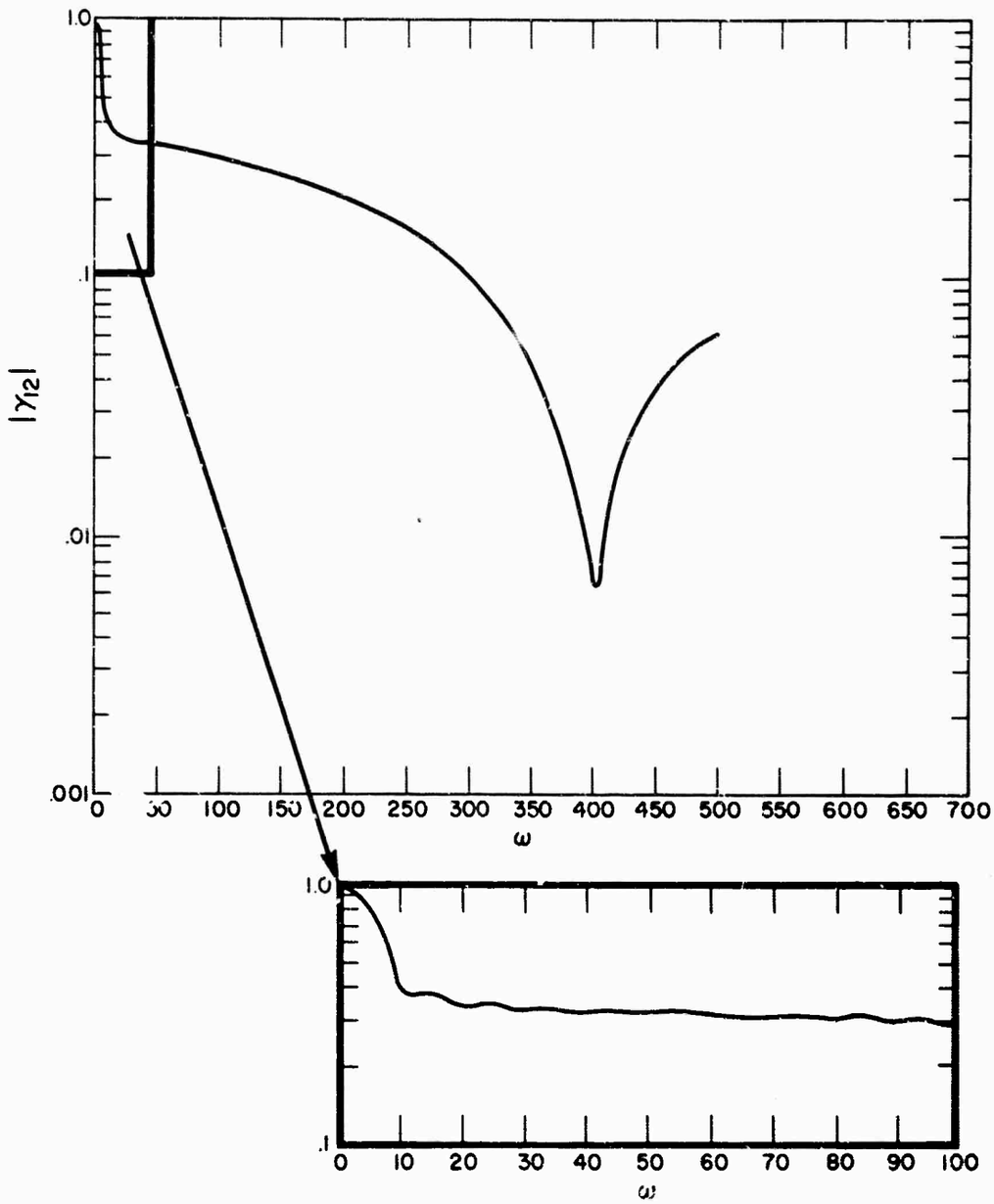

Figure 30. Fringe Contrast $|\gamma_{12}|$ As Function of ω for $\alpha = 0^{o}$, $B'/B = 10$

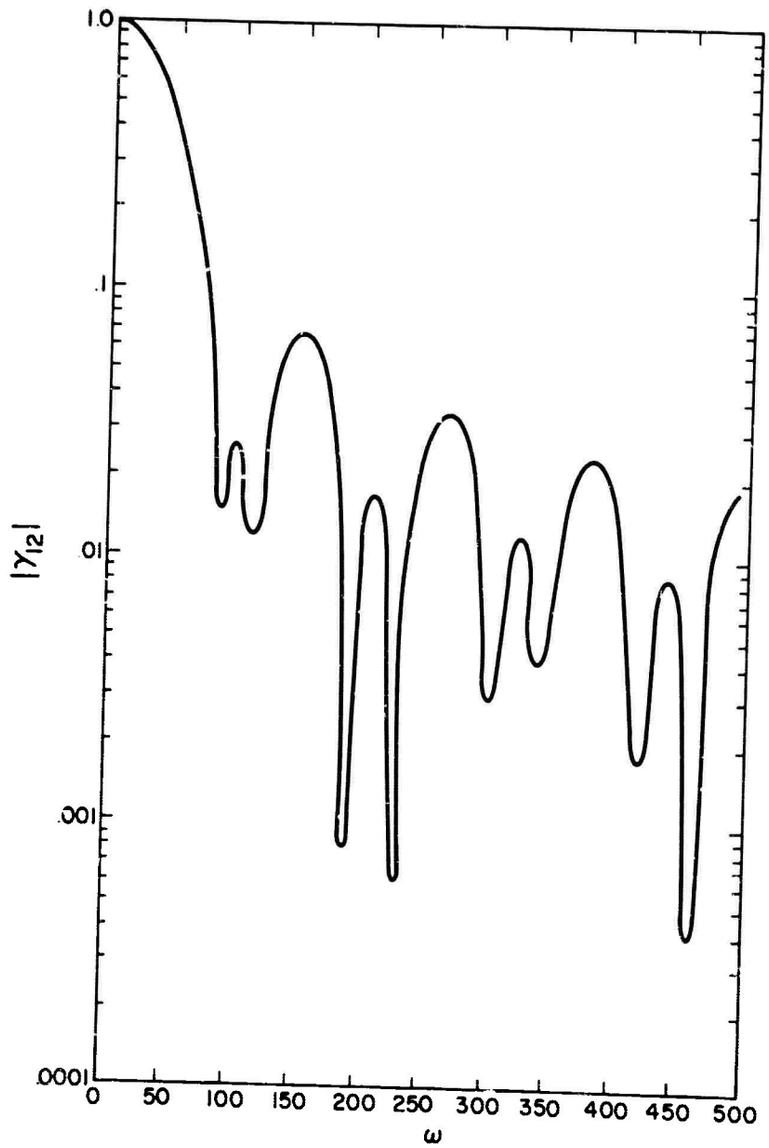

Figure 31. Fringe Contrast $|\gamma_{12}|$ As Function of ω for $\alpha = 90^{\circ}$, $B'/B = 10$

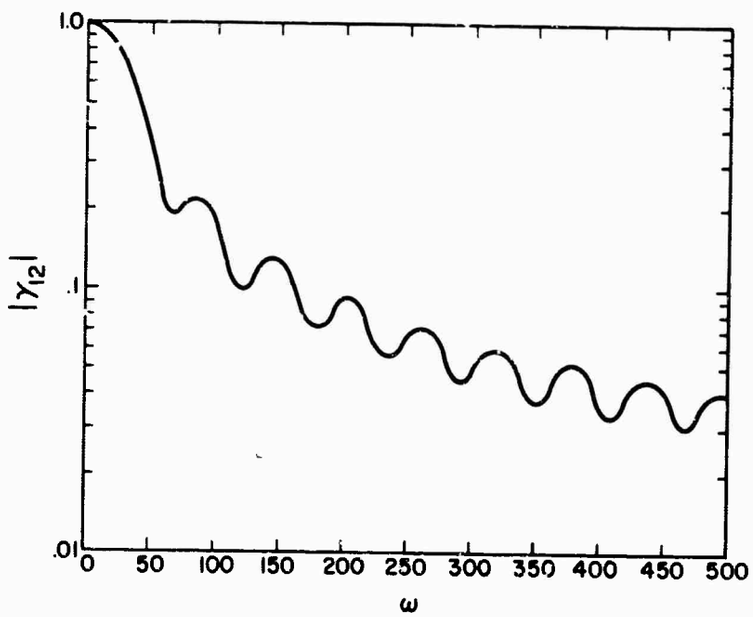

Figure 32. Fringe Contrast $|\gamma_{12}|$ As Function of ω for $\alpha = 90^{\circ} \pm 5^{\circ}$, $B'/B = 10$

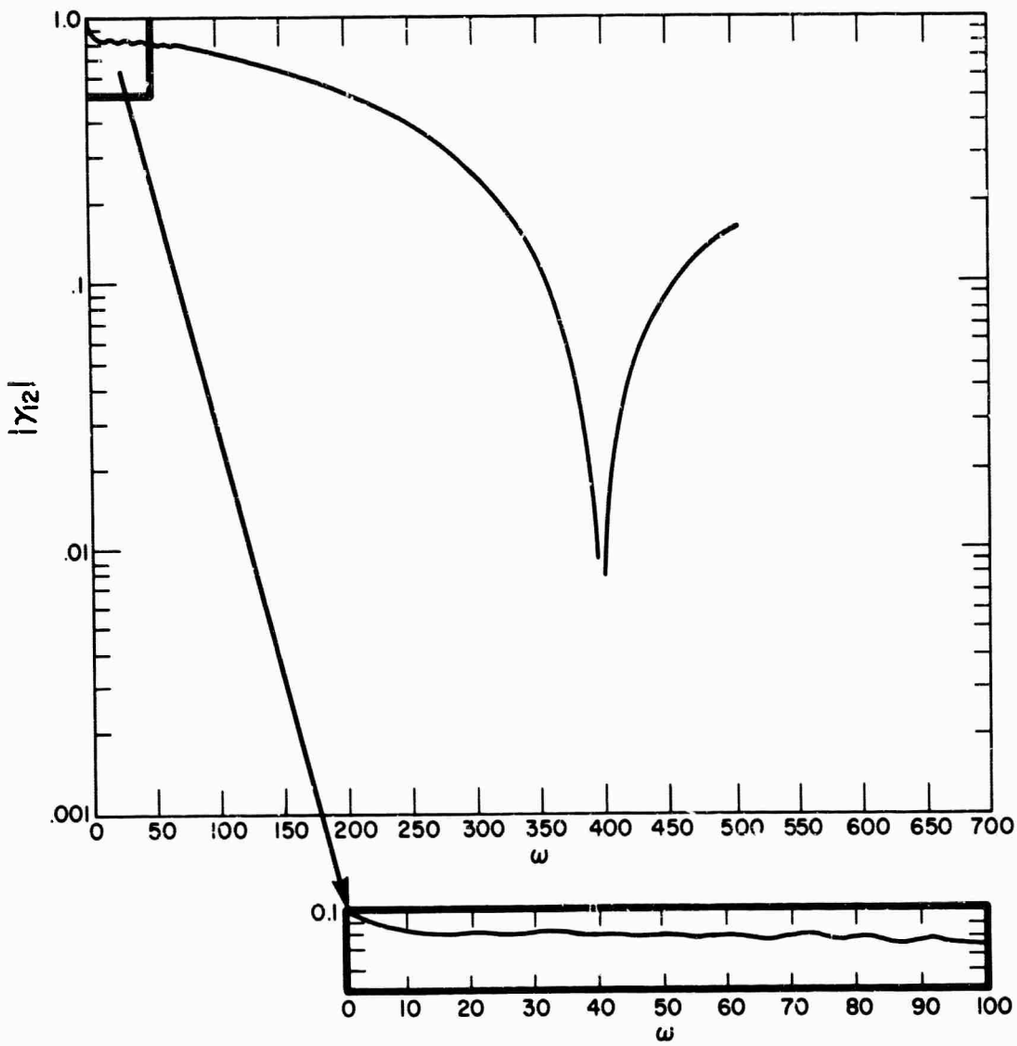

Figure 33. Fringe Contrast $|\gamma_{12}|$ As Function of ω for $\alpha = 0^{\circ}$, $B'/B = 100$

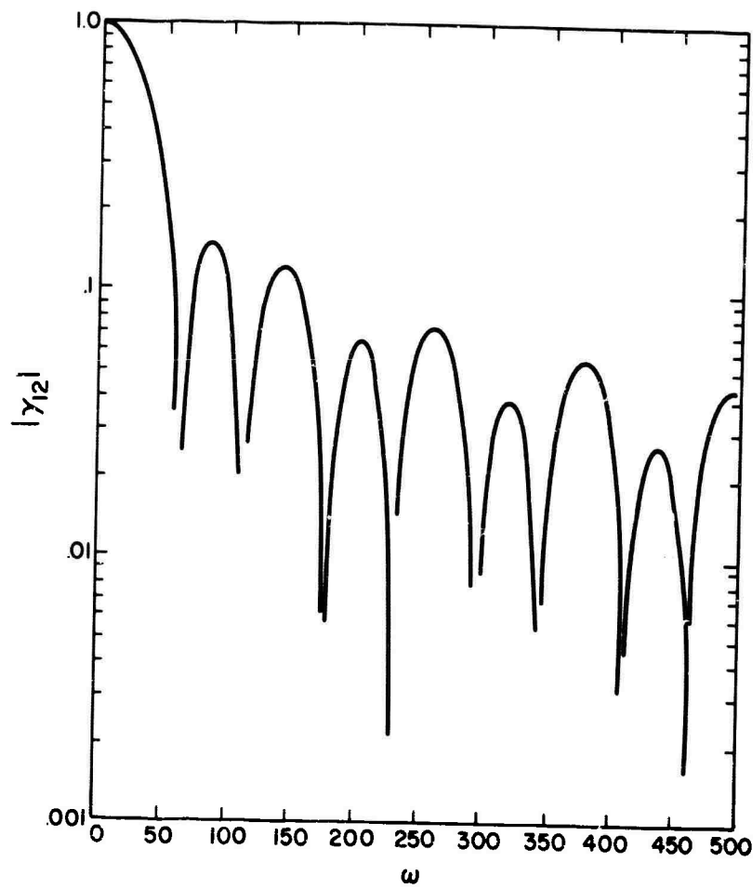

Figure 34. Fringe Contrast $|\gamma_{12}|$ As Function of ω for $\alpha = 90^{\circ}$, $B'/B = 100$

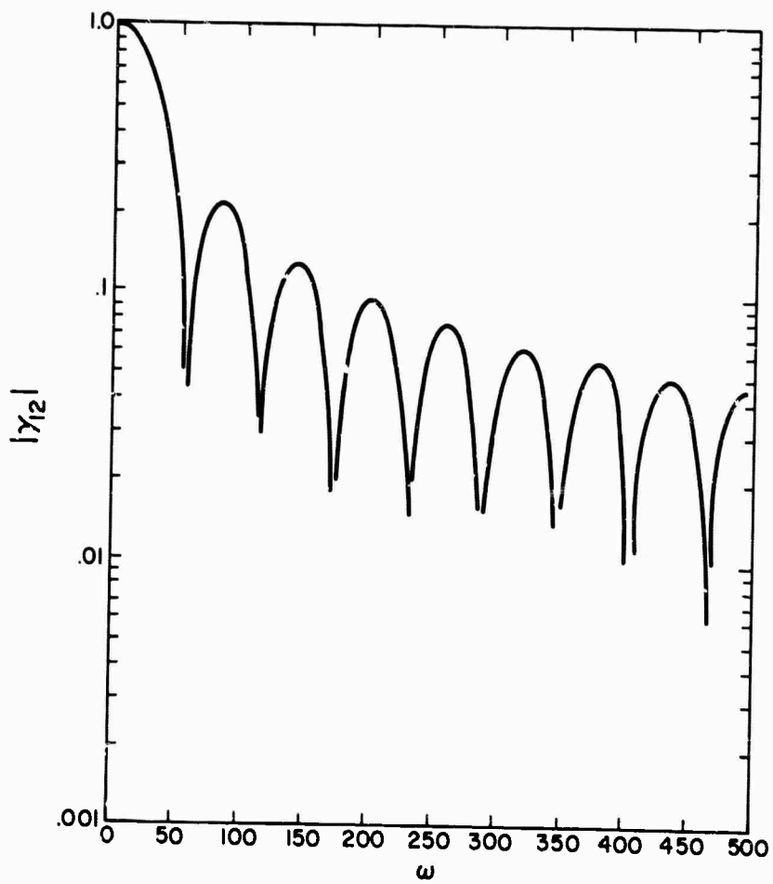

Figure 35. Fringe Contrast $|\gamma_{12}|$ As Function of ω for $\alpha = 90^{\circ} \pm 5^{\circ}$, $B'/B = 100$

EXPERIMENT

To verify the calculated values of $|\gamma_{12}|$, the following experiment was performed. A 10° cone, 0.5 mm high, illuminated with laser light provided a coherently illuminated source. This illuminated cone was Fourier-transformed by standard optical techniques and the result was recorded on film. Microdensitometer traces of the film were then compared with the calculated data.

The cone was constructed by drilling a number of 1 mm holes in brass shim stock 0.005 in. thick and selecting the best hole. A cone was then formed by laying two pieces of aluminum sheet over the hole at a 10° angle; the point of the angle formed was centered in the 1 mm hole. The two straight edges involved were formed by folding thin sheets of aluminum. After trying several techniques including razor blade edges, folded aluminum was found to provide the best results. The entire cone assembly was mounted on a microscope slide. A photomicrograph of the cone is shown in Figure 36.

Figure 36. Micrograph of Pie-Shaped Source (100X)

The cone was illuminated with laser light with a coherence interval of 7 mm. Since the largest dimension of the cone was only 0.5 mm, the cone was essentially coherently illuminated. The cone aperture was transformed by using a 10 in. focal length lens in the standard configuration shown in Figure 37. The transform was recorded on plus-X film and traced with a microdensitometer. An enlarged picture of the transform is shown in Figure 38. Slight asymmetries in the transform were attributed to the fact that the focal plane of the lens is not perfectly flat. Initial experiments using a mercury arc lamp to illuminate the cone provided substantially poorer results than the laser, since the mercury arc lamp is not as bright as the laser and, as a result, focusing was more difficult.

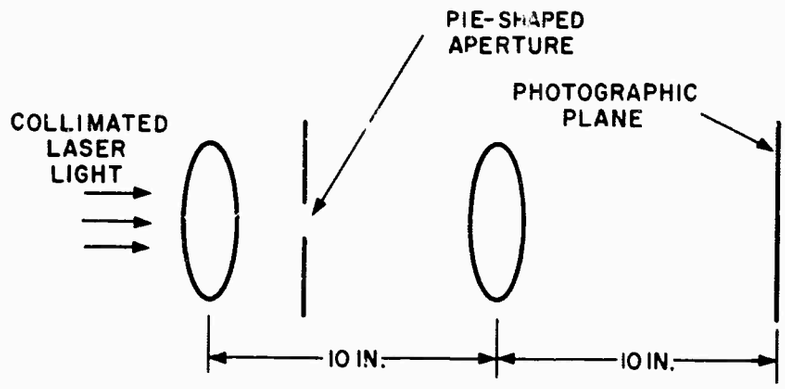

Figure 37. Optical System Used to Transform Cone-Shaped Aperture

Figure 38. Enlarged Micrograph of Transform of Pie-Shaped Source

Because a coherent diffraction system was used, the desired Fourier transform is represented in amplitude and therefore the recorded data in intensity is equal to $|\gamma_{12}|^2$. To make a comparison of experimental and calculated data, it was therefore necessary to square the calculated values. The resulting curves are shown in Figures 39 to 41 along with the microdensitometer traces of the experimental data.

There appears to be good qualitative agreement between the calculated and experimental data shown. No attempt was made to find quantitative agreement, for instance, of the relative values of the maxima because of the nonlinearity of the film record at high and low intensities. However, the positions of maxima and minima agree to well within 5%.

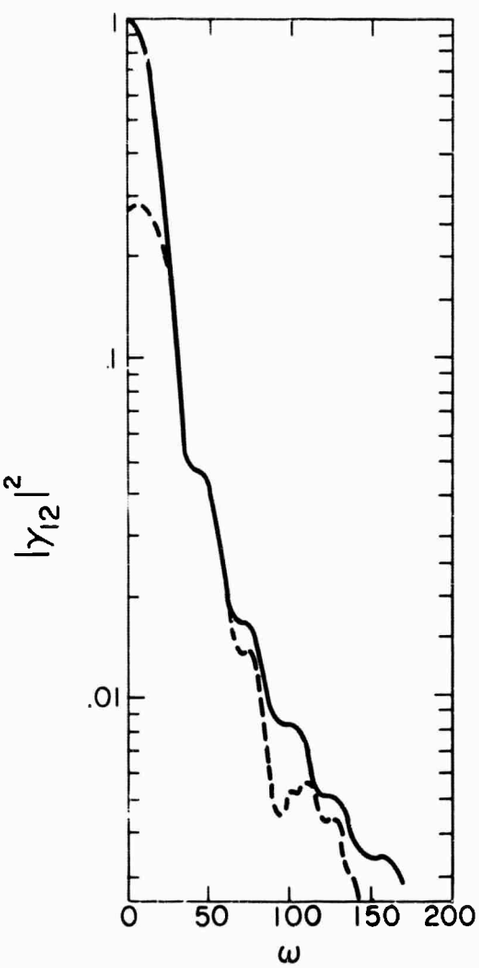

Figure 39. Experimental and Theoretical Results for $|\gamma_{12}|^2$ for $\varphi = 0^o$

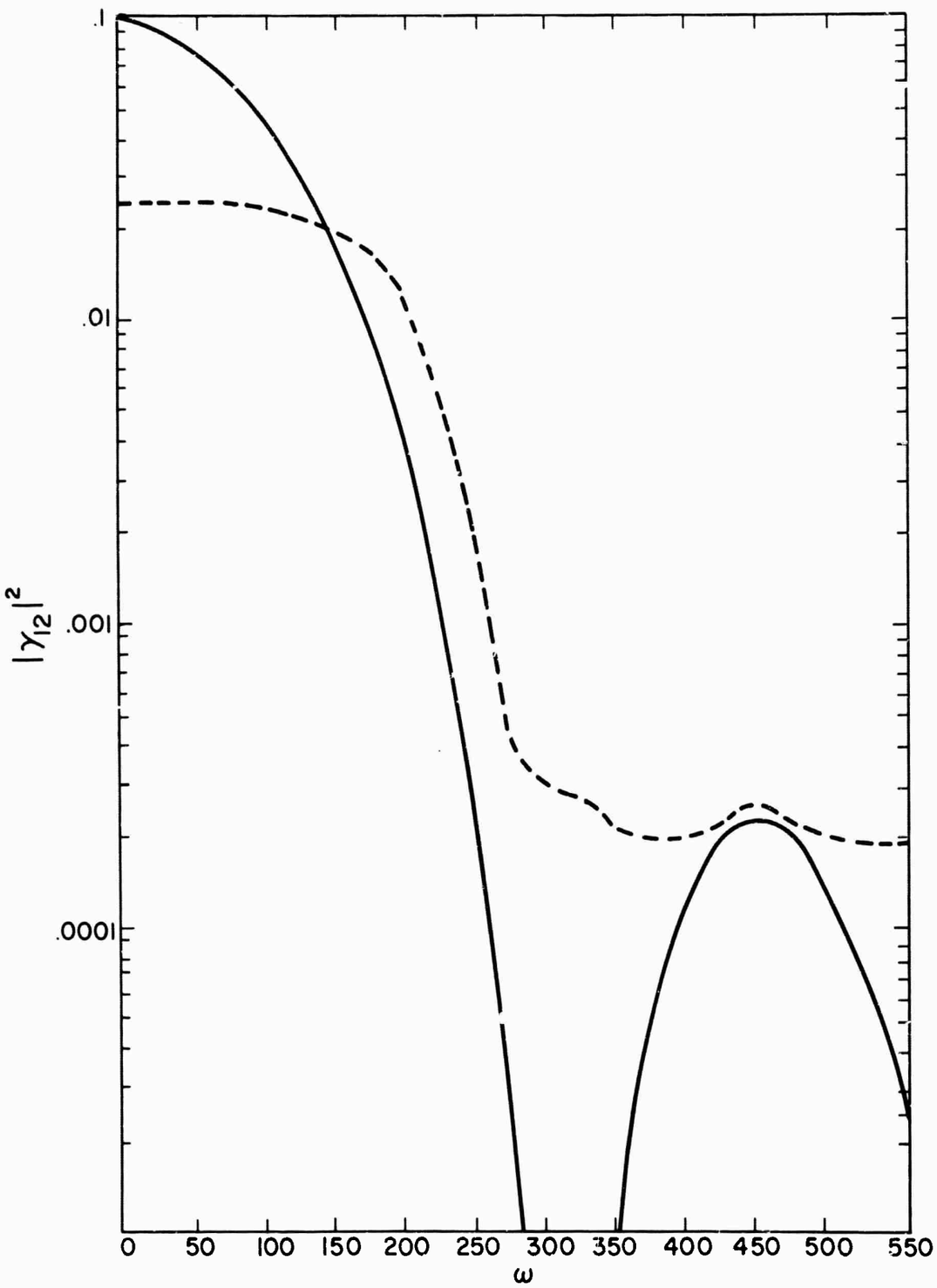

Figure 40. Experimental and Theoretical Results for $|\gamma_{12}|^2$ for $\varphi = 90^\circ \pm 5^\circ$

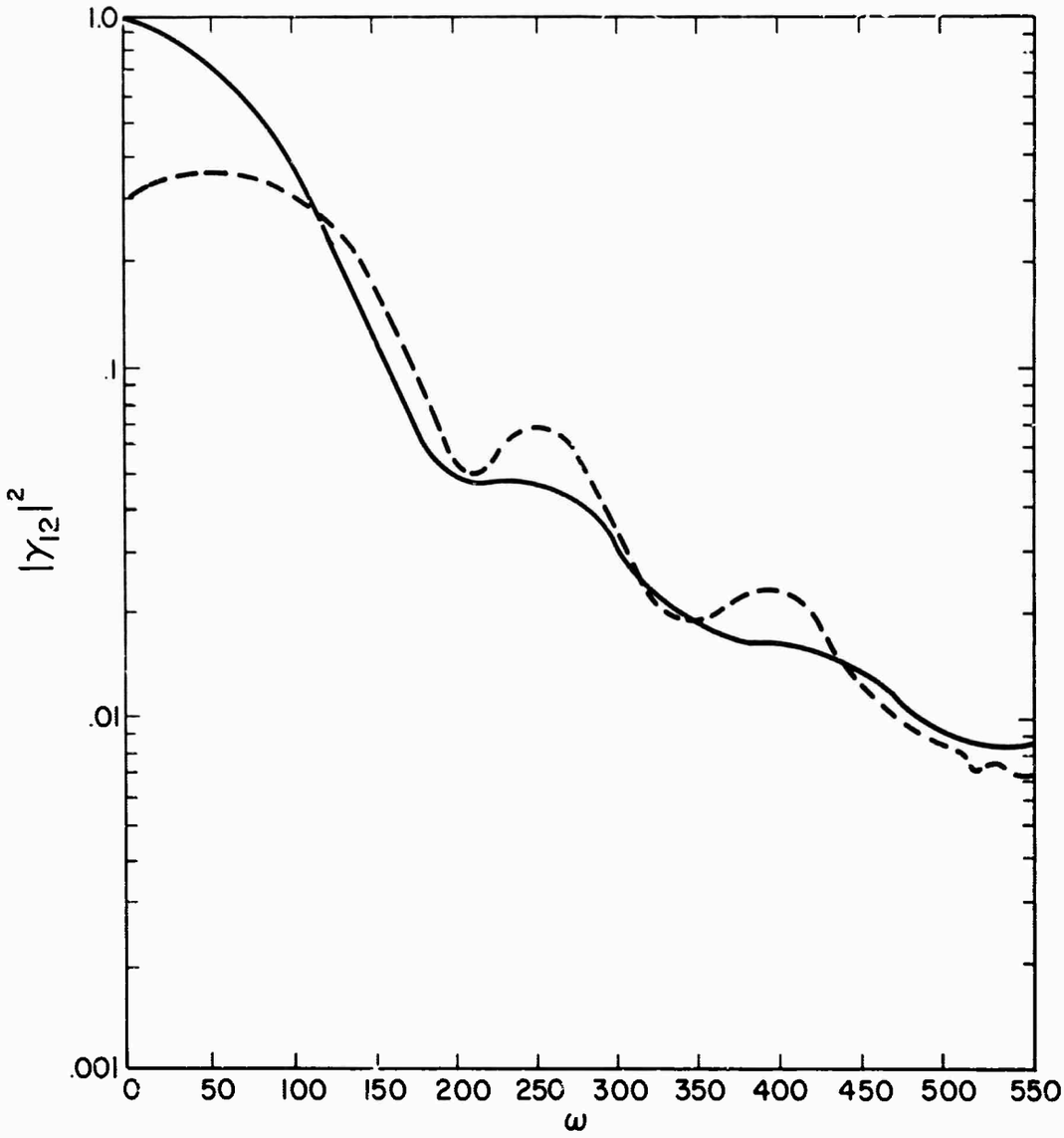

Figure 41. Experimental and Theoretical Results for $|\gamma_{12}|^2$ for $\varphi = 90^{\circ}$

SECTION VII

CONCLUSIONS AND RECOMMENDATIONS

SUMMARY

The feasibility of an electronic fringe detector has been firmly established. A fringe detector operating in conjunction with a Fizeau interferometer has been designed, constructed, operated, and tested in the laboratory. Methods for analyzing the detecting system output have been established to optimize the sensitivity of the fringe detector from the standpoint of noise and discrimination techniques. The atmospheric noise inputs that degrade the resolution capabilities of both telescopes and interferometers have been analyzed, and the appropriate atmospheric research required has been defined. The possible use of a Michelson stellar interferometer to analyze the characteristics of pie-shaped sources has been analyzed by both a theoretical computer study and an experimental study. The pie-shaped source proved to have characteristics that are not particularly compatible with a Michelson stellar interferometer.

FRINGE DETECTOR

A Fizeau interferometer fringe-detector combination was constructed with variable separation apertures that can be adjusted from 0.6 to 6 cm. Aperture height was maintained at 0.1 times the separation. These apertures were in front of a 200 in. focal length optical system, which was used to produce a fringe pattern by superimposing the partially coherent light entering the two apertures. The fringe pattern was reflected by a rotating reflector and focused onto a single slit immediately in front of a phototube. The rotating reflector, single slit, and phototube combine to transform the spatially varying intensity pattern of the fringe field into a time-varying voltage signal displayed on an oscilloscope face. The oscilloscope trace was photographed and analyzed to determine fringe contrast.

The performance capabilities of the fringe detector are shown in Figure 22 (p. 29), which plots the fringe contrast required for detection as a function of watts per centimeter squared incident on the fringe detector. This is a general curve for any source in that the source brightness, size, and source-to-interferometer distance can be combined and expressed as watts per centimeter squared incident on the fringe detector.

There are four ways in which the performance of the fringe detector can be significantly improved in terms of sensitivity. If a grating instead of a slit were used to demodulate the fringes, a factor of 5 to 10 could be gained in sensitivity. A more sophisticated phototube (cooled) could provide a factor of 20 improvement in sensitivity. If the design of the entrance aperture were optimized for the particular application of interest, it could provide a factor of 5 improvement. A further gain in sensitivity could

be obtained by using long slits and a cylindrical lens as discussed under "Other Systems Considered" (p. 7). This system would be useful only if measurement of fringe contrast at a single aperture separation were required. Overall, an ultimate fringe detector could be as much as 500 to 1000 times as sensitive as this instrument.

The following considerations and problems are involved in designing and constructing the optimum instrument. The integrals involved in designing the optimum configuration for the variable separation apertures could only be evaluated on a computer, if then. A single grating cannot be used with variable separation apertures because the optical design required (zoom lens) is impractical over the range of aperture separations required. Either the grating must be changed or a number of fringe detectors operating in parallel must be used to measure fringe contrast at different aperture separations. To maximize phototube sensitivity, the phototube must be cooled; it must have an optical response matched to the source; and it must have a photoemissive surface whose area is as small as possible consistent with the area of the grating. A specially designed phototube such as the phototube with the grating behind the photoemissive surface as described in "Design Criteria" (p. 3) may be required. If the interferometer is to operate under conditions where the brightness of the source is fluctuating, or if there is an ambient background illumination present, then additional channels will be required as discussed under "Outside Noise Sources" (p. 31).

COMPARISON WITH TELESCOPE

In addition to higher resolution, the interferometer has advantages over the single-mirror telescope in that it can electrically filter out part of the noise due to image motion and ambient background illumination. The telescope can probably equal or surpass the interferometer when the source intensity is fluctuating. The important atmospheric parameters to study to compare the interferometer to the telescope are image motion and reductions in the complex degree of coherence due to atmospheric turbulence as well as ambient sky illumination and atmospheric induced image motion.

PIE-SHAPED SOURCES

From the calculated values of fringe contrast, $|\gamma_{12}|$, we may conclude that the use of a Michelson stellar interferometer to study pie-shaped sources is more difficult than for simple circular sources. One reason is that $|\gamma_{12}|$ does not possess well-defined zeros, or maxima, which may be directly related to any one source characteristic such as radial or angular size. Also, even where a distinct and measurable pattern is apparent which might be related to all the characteristic parameters of the source, the wide differences in intensity values or the extreme minuteness of detail, and the lower overall illumination available (compared to a circular source) demand a very sensitive recording instrument.

REFERENCES

1. M. Born and E. Wolf, Principles of Optics, 2nd ed. (New York, N.Y.: The Macmillan Company, 1964).

2. J. Scheiner and S. Hirayama, Akhandl. Deut. Akad. Wiss., Vol. I (Berlin, 1894).

3. A.I. Mahan, C.B. Bitterli, and S.M. Cannon, J. Opt. Soc. Am. 54, 721 (1964).

4. E.L. O'Neill, Introduction to Statistical Optics (Reading Mass.: Addison-Wesley Publishing Company, Inc., 1963), p. 139.

5. D. Gabor, Progress in Optics, Vol. 1, E. Wolf, ed. (North-Holland Publishing Company, 1961), p. 139.

APPENDIXES

I. THE MICHELSON STELLAR INTERFEROMETER

II. COMPUTER PROGRAM FOR PIE-SHAPED SOURCES

III. SPECIFICATIONS FOR FRINGE DETECTOR

IV. GRATING MODULATION CHARACTERISTICS

BLANK PAGE

APPENDIX I

THE MICHELSON STELLAR INTERFEROMETER

The construction of the Michelson stellar interferometer is shown in Figure 42. The inner mirrors, M_2 and M_3, are fixed, while the outer mirrors, M_1 and M_4, are symmetrically movable and perpendicular to axis OA. Light from the distance source, after reflection by the mirrors, passes through the two apertures S_1 and S_2, and into the telescope objective. The separation of the two beams is given by the separation of the two mirrors M_1 and M_4, and this separation can be made much larger than the aperture of the objective. Because the fringe contrast as a function of beam separation is inversely related to the object size, the smallest angular diameter that may be measured for simple objects is determined here by the maximum possible separation of the outer mirrors and not by the diameter of the objective. When the mirrors are removed, the system collapses to the simple Fizeau interferometer, where the smallest angular diameter measurable is determined by the aperture separation rather than the separation of the outer mirrors. The Michelson system therefore allows measurements of much smaller angular diameters for a given lens diameter than the Fizeau system.

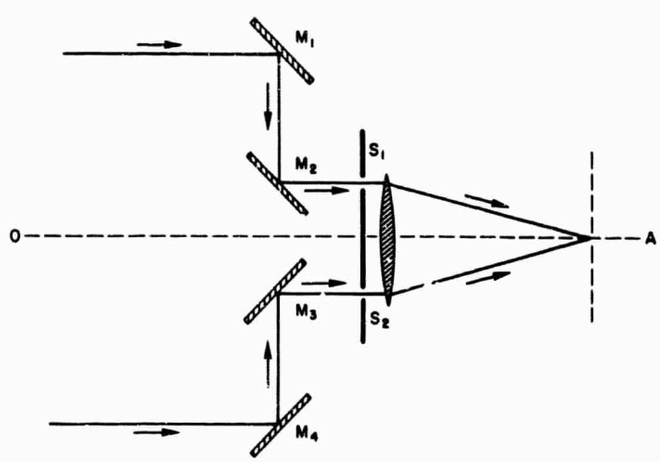

Figure 42. Schematic Diagram of the Michelson Stellar Interferometer

The following is an analysis of the Fizeau system, but it may be readily extended to that of Michelson. However, before analyzing the system in Figure 42, we must consider a few pertinent definitions from coherence theory. For an extensive treatment of coherence theory, see Refs. 1 and 6.

BASIC DEFINITIONS

MUTUAL COHERENCE FUNCTION

The basic entity in the theory of partial coherence is the mutual coherence function $\Gamma_{12}(\tau)$, for points $\underline{x}_1$ and $\underline{x}_2$, which may be defined by

$$\Gamma_{12}(\tau) \equiv \Gamma\left(\underline{x}_1, \underline{x}_2, \tau\right) = \left\langle V\left(\underline{x}_1, t\right) V^*\left(\underline{x}_2, t + \tau\right)\right\rangle \quad . \tag{1}$$

Here the underscore denotes position vector, the asterisk a complex conjugate, and the sharp brackets indicate a long time average†

$$\langle f \rangle = \lim_{T \to \infty} \frac{1}{2T} \int_{-T}^{T} f dt \quad . \tag{2}$$

In (1) V is the analytic signal associated with the optical disturbance, which we assume to be a single Cartesian component of the electric field vector. In terms of the mutual coherence function, the complex degree of coherence $\gamma_{12}(\tau)$ is defined as

$$\gamma_{12}(\tau) = \frac{\Gamma_{12}(\tau)}{\sqrt{\Gamma_{11}(0)\, \Gamma_{22}(0)}} \tag{3}$$

It should be noted that the complex degree of coherence, like the mutual coherence function, is in general a function of seven variables, six position coordinates and the time-delay coordinate τ.

The treatment of problems involving partially coherent light involves the solution of the two wave equations:

$$\nabla_s^2 \Gamma_{12}(\tau) = \frac{1}{c^2} \frac{\partial^2 \Gamma_{12}(\tau)}{\partial \tau^2} \qquad (s = 1, 2) \quad , \tag{4}$$

where ∇_s^2 denotes the Laplacian operator in the coordinates of the point x_s. A typical problem involves determining the mutual coherence in the source or object plane, solving (4) to obtain the mutual coherence on a later surface such as the image plane, and then recovering the intensity, I, in the plane of interest from the relation

$$I\left(\underline{x}_1\right) = \Gamma\left(\underline{x}_1, \underline{x}_1, 0\right) \quad . \tag{5}$$

---

†Equation (2) is equivalent to the definition introduced by Wolf, though in a slightly different form.

Equation (5) follows directly from the definition of the mutual coherence function and the properties of the analytic signal.

For a large class of problems the theory outlined in the preceding paragraph may be greatly simplified. These problems are characterized by the quasi-monochromatic approximations, which are stated as

$$\left\{ \begin{array}{l} \Delta\nu < \bar{\nu} \\ |\tau| \ll \dfrac{1}{\Delta\nu} \end{array} \right\}$$

where $\Delta\nu$ is the spectral width and $\bar{\nu}$ the mean wavelength. Of these two constraints, the second is obviously the more significant. White light may often be treated as quasi-monochromatic if the path differences, $c|\tau|$, involved in the experiment are suitably small. In those circumstances for which the approximations above are applicable, the mutual coherence function may be replaced by the mutual intensity function $\Gamma(\underline{x}_1, \underline{x}_2)$:

$$\Gamma\left(\underline{x}_1, \underline{x}_2\right) \equiv \Gamma_{12} = \Gamma\left(\underline{x}_1, \underline{x}_2, 0\right) \quad . \tag{6}$$

The complex degree of coherence reduces to $\gamma_{12}(0) \equiv \gamma_{12}$, and the wave equations (4) reduce to the two Helmholtz equations

$$\nabla_s^2 \Gamma_{12} + \underline{k}^2 \Gamma_{12} = 0 \qquad (s = 1, 2) \quad , \tag{7}$$

where k is the wave number.

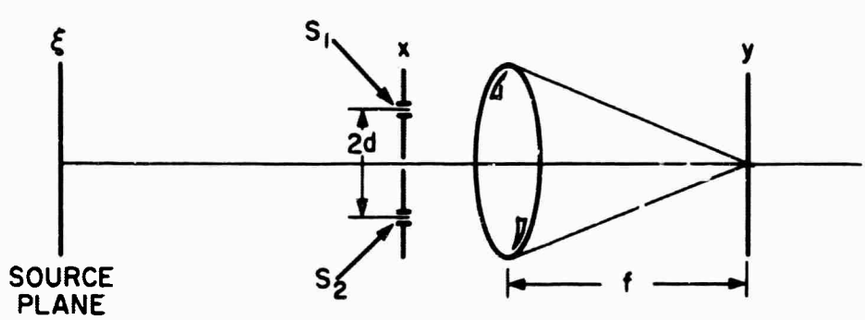

Figure 43. Schematic Diagram of Fizeau Interferometer

ANALYSIS OF FIZEAU INTERFEROMETER

We may now proceed to analyze the interferometer in Figure 43 from the viewpoint of coherence theory. A source in the ξ-plane will give rise to a disturbance in the x-plane of the form $\Gamma(x_1, x_2)$[6] as described by the van Cittert-Zernike theorem. The van Cittert-Zernike theorem says that $\Gamma(x_1, x_2)$ is the normalized Fourier transform of the source intensity distribution. This theorem is discussed further under "Investigation of Pie-Shaped Sources" (p. 35). (To be as general as possible, we will make no assumptions about the character of the source here except that it is quasi-monochromatic, $\Gamma(x_1, x_2, \tau) = \Gamma(x_1, x_2)$.) In the x-plane $\Gamma(x_1, x_2)$ is multiplied by the transmission function of the apertures, which we will represent by

$$t(x) = \delta(x + d) + \delta(x - d) = \delta(x \pm d)$$

where $\delta(x)$ is the unit impulse function. The resulting disturbance is passed through a lens and then propagated, by use of the Green's function solution to the wave equation, to the y-plane. This process may be represented mathematically by

$$\iint \Gamma\left(x_1, x_2\right) t\left(x_1\right) t^*\left(x_2\right) e^{-\frac{ik}{2f}\left(x_1^2 - x_2^2\right)} e^{\frac{ik}{2f}\left[\left(y - x_1\right)^2 - \left(y - x_2\right)^2\right]} dx_1\, dx_2 \ .$$

Substituting for $t(x_1)\, t^*(x_2)$ and simplifying yields the intensity in the y-plane

$$I(y) = \iint \Gamma\left(x_1, x_2\right) \delta\left(x_1 \pm d\right) \delta\left(x_2 \pm d\right) e^{\frac{-iky}{f}\left(x_1 - x_2\right)} dx_1\, dx_2 \ .$$

Performing the integration yields

$$I(y) = \Gamma(-d, -d) + \Gamma(d, d)$$
$$+ \Gamma(-d, d)\, e^{\frac{iky}{f}(2d)} + \Gamma\left(d, -d\right) e^{\frac{-iky}{f}(2d)} \ .$$

We may then note that $\Gamma(-d, -d)$ is just the intensity I_1 at the slit S_1 and similarly $\Gamma(d, d)$ is the intensity I_2 at slit S_2. Since the two points x_1 and x_2 must be indistinguishable, $\Gamma(-d, d)$ is equal to $\Gamma(d, -d)$ and we may write

$$I(y) = I_1 + I_2 + 2\Gamma_{12} \cos \frac{2kyd}{f}$$

where Γ_{12} represents the mutual coherence function for points S_1 and S_2. Substituting from Eq. (3) in the above yields the result quoted in Section VII (p. 35).

$$I(y) = I_1 + I_2 + 2\sqrt{I_1 I_2}\,\gamma_{12} \cos \frac{2kdy}{f}$$

For other approaches to this problem see Refs. 1, 7, and 8.

REFERENCES

1. M. Born and E. Wolf, Principles of Optics, 2nd ed. (New York, N.Y.: The Macmillan Company, 1964).

2. J. Scheiner and S. Hirayama, Akhandl. Deut. Akad. Wiss., Vol. I (Berlin, 1894).

3. A.I. Mahan, C.B. Bitterli, and S.M. Cannon, J. Opt. Soc. Am. 54, 721 (1964).

4. E.L. O'Neill, Introduction to Statistical Optics (Reading, Mass.: Addison-Wesley Publishing Company, Inc., 1963), p. 139.

5. D. Gabor, Progress in Optics, Vol. 1, E. Wolf, ed. (North-Holland Publishing Company, 1961), p. 139.

6. M. Beran and G.B. Parrent, "Theory of Partial Coherence" (Englewood Cliffs, N.J.: Prentice-Hall, Inc., 1963).

7. B.J. Thompson and E. Wolf, J. Opt. Soc. Am. 47, 895 (1957).

8. B.J. Thompson, J. Opt. Soc. Am. 48, 95 (1958).

APPENDIX II

COMPUTER PROGRAM FOR PIE-SHAPED SOURCES

Below is the actual computer program written for the IBM 7094-II computer system (Fortran II) under this contract. The program computes the fringe contrast in a Michelson stellar interferometer arising from a distant cone-shaped source. The input specifies the cone angle, angular distribution, and relative intensities of three intensity zones in the radial direction. The output is the normalized value of $|\gamma_{12}|$ as a function of cone orientation and slit separation.

```
C       CALCULATION OF FRINGE CONTRAST, I.E. MUTUAL COHERENCE FUNCTION
C       FOR 10'DEGREE CONE'SHAPED SOURCES ALLOWING FOR WEIGHTING OF THREE
C       SEGMENTS RADIALLY AND VARIABLE DISTRIBUTION IN THETA DIRECTION
C       SIZE OF INPUT MAY NOT EXCEED 200 X 35
        DIMENSION PHI(50),F(35),THETA(35),W(200),C(35),R(200),WR(200),X(35
       2,200),CY(35,200),SY(35,200),FMCR(200),FMCI(200),FMOD(200)
      1 READ INPUT TAPE 5,10,DELR,DELTH,DELW
     10 FORMAT(3F6.4)
        READ INPUT TAPE 5,20,WGTFCN
     20 FORMAT(F8.4)
        READ INPUT TAPE 5,30,IPHI,ITH,IW
     30 FORMAT(3I3)
        READ INPUT TAPE 5,20,(PHI(K),K=1,IPHI)
        READ INPUT TAPE 5,20,(F(N),N=1,ITH)
        WRITE OUTPUT TAPE 6,40
     40 FORMAT(37H1CALCULATION OF FRINGE CONTRAST 41391)
        WRITE OUTPUT TAPE 6,50,DELR,DELTH,DELW
     50 FORMAT(11HODELTA RHO=F6.4,12HDELTA THETA=F6.4,12HDELTA OMEGA=F6.4)
        WRITE OUTPUT TAPE 6,60,WGTFCN
     60 FORMAT(49HOWEIGHTING CONSTANT FOR INNER AND OUTER SEGMENTS=F8.4)
        WRITE OUTPUT TAPE 6,70
     70 FORMAT(21H1ANGULAR DISTRIBUTION)
        KK=1
        THETA(1)=-.0873&.5*DELTH
        DO 100 N=2,ITH
    100 THETA(N)=THETA(N-1)&DELTH
        WRITE OUTPUT TAPE 6,80
     80 FORMAT(1H0,/13X,5HTHETA,9X,9HANG.DIST.)
        WRITE OUTPUT TAPE 6,90,(THETA(N),F(N),N=1,ITH)
     90 FORMAT(1H0,2(10X,F8.4))
        W(1)=0.
        DO110 M=2,IW
    110 W(M)=W(M-1)&DELW
        R(1)=DELR/2.
        R(200)=199.5*DELR
        DO 120 K=2,199
```

```
 120 R(K)=R(K-1)&DELR
     DO 121 K=1,5
 121 WR(K)=R(K)*WGTFCN*DELTH*DELR
     DO 122 K=6,195
 122 WR(K)=R(K)*DELTH*DELR
     DO 123 K=196,200
 123 WR(K)=R(K)*WGTFCN*DELTH*DELR
1000 DO130 N=1,ITH
 130 C(N)=COSF(THETA(N)-PHI(KK))
     DO 140 K=1,200
     DO 140 N=1,ITH
 140 X(N,K)=R(K)*C(N)*6.28318
     MM=1
2000 DO 150 K=1,200
     DO150 N=1,ITH
     ARG=W(MM)*X(N,K)
     CY(N,K)=COSF(ARG)*F(N)
 150 SY(N,K)=SINF(ARG)*F(N)
     FMCR(MM)=0.
     FMCI(MM)=0.
     DO 155 K=1,200
     DO 155 N=2,ITH
     SY(1,K)=SY(1,K)&SY(N,K)
 155 CY(1,K)=CY(1,K)&CY(N,K)



     DO160 K=1,200
     FMCR(MM)=FMCR(MM)&CY(1,K)*WR(K)
 160 FMCI(MM)=FMCI(MM)&SY(1,K)*WR(K)
     FMOD(MM)=(FMCR(MM)**2 &FMCI(MM)**2 )**.5
     IF(IW-MM)3000,3000,170
 170 MM=MM&1
     GO TO 2000
3000 WRITE OUTPUT TAPE 6,200,PHI(KK)
 200 FORMAT(26H1MUTUAL COHERENCE FUNCTION,15X,4HPHI=F8.4)
     FNORM=FMOD(1)
     DO 205 K=1,IW
 205 FMOD(K)=FMOD(K)/FNORM
     WRITE OUTPUT TAPE 6,210,(W(K),FMOD(K),K=1,IW)
 210 FORMAT(1H0,2(10X,F8.4))
     IF(IPHI-KK)4000,4000,220
 220 KK=KK&1
     GO TO 1000
4000 GO TO 1
     END
```

APPENDIX III

SPECIFICATIONS FOR FRINGE DETECTOR

Construction drawings for the electronic fringe detector are given in Figures 44 (front view) and 45 (top and side views). The component specifications are as follows (letters refer to letters on figures):

A. Variable Separation Apertures

B. 24 in. F.L. Positive Lens

C. Adjustable Focus Control

D. 40 mm F.L. Negative Lens

E. Viewing Mirror

F. 10X Erfle Viewing Eyepiece

G. Mirror Position Control

H. Bodine No. NSH-12R Motor with Variable Speed Control

I. Eight-Sided Silvered Rotating Reflector

J. Adjustable Interferometer Slit

K. Slit Width Control

L. Photo-Tube Cell with E.M.I. No. 95245 Photomultiplier Tube

Other components not shown:

Baird Atomic No. 345 Super Stable Power Supply

Tektronix - No. 547 Scope with 53E/54E Preamplifier

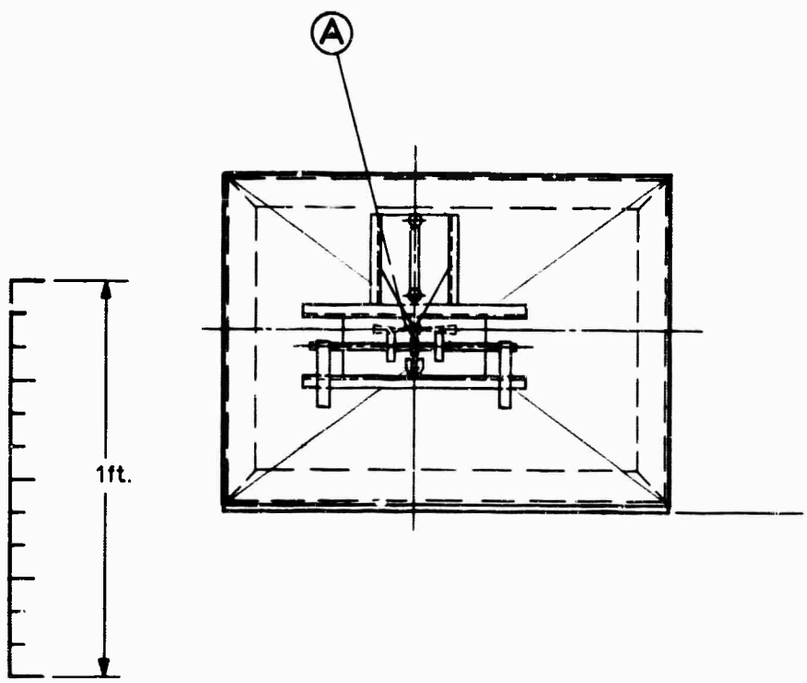

Figure 44. Electronic Fringe Detector, Front View

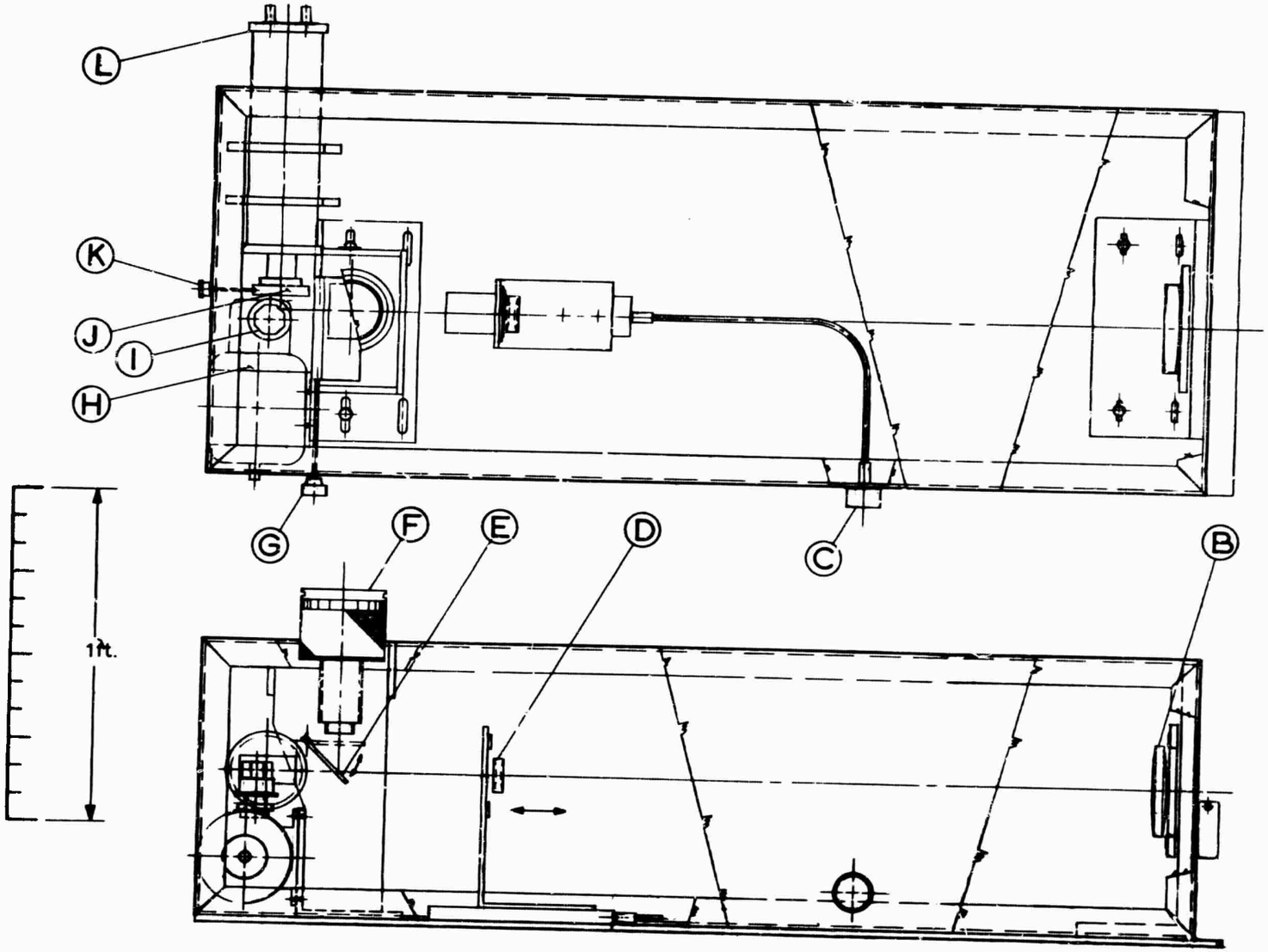

Figure 45. Electronic Fringe Detector, Top and Side Views

BLANK PAGE

APPENDIX IV

GRATING MODULATION CHARACTERISTICS

In order to study conversion of the field by a grating, first consider a uniform set of fringes described in one dimension by

$$I(x) = I_o(1 + a \cos \omega x) \quad , \tag{1}$$

where I(x) is the intensity at any point x, I_o is the average intensity, a is a non-dimensional constant between 0 and 1 describing the fringe contrast, ω is the spatial fringe frequency, and x is the positional variable. The fringe contrast, F.C., is given by

$$F.C. = \frac{(1 + a) - (1 - a)}{(1 + a) + (1 - a)} = a \quad . \tag{2}$$

In order to monitor the fringe contrast of a spatial fringe distribution electronically, it is useful to transform the spatial function into a time-modulated electrical signal. A pinhole traveling at a uniform rate in a direction perpendicular to the fringes would transmit an intensity I(t), described by a function of the form

$$I_o(1 + ca \cos \omega' t) \quad , \tag{3}$$

where c is a constant between 0 and 1, a is the fringe contrast, t is time, and ω' is a frequency. A phototube monitoring the transmitted intensity would yield the desired time-modulated electrical signal. Similarly, if a line of pinholes at the same spatial frequency as the fringes is properly aligned with the fringes, the transmitted intensity function will be similar to that given by Eq. (3) and will have an energy content that increases with the number of pinholes.

Expanding to two-dimensions, we see that the pinholes become a transmission grating. If ν describes the grating frequency and v is velocity in fringes/second, the output intensity of a moving grating, $g(\nu x - vt)$, is described by a function of the form

$$\begin{aligned} I(t) &= I_o \left\{ 1 + f_1(\omega - \nu)\, f_2\left[g(\nu x - vt),\ I(x)\right]\, f_3(\Delta\phi)\, a \cos \omega' t \right\} \\ &= I_o \left[1 + Ha \cos \omega' t \right] \quad , \end{aligned} \tag{4}$$

where I(t) and I_o are intensities and a represents the original fringe contrast. The functions $f_1(\omega - \nu)$, $f_2[g(\nu x - vt), I(x)]$, and $f_3(\Delta\phi)$ are real numbers between 0 and 1 representing, respectively, the frequency error between the grating and the fringes, the form of the grating and the fringes, and alignment errors.

If the total or a known portion of the light incident on the grating is chopped and this modulated intensity is monitored by a phototube, the resulting peak-to-peak value of the phototube output is a measure of I_0 in Eq. (4). The peak-to-peak value of the phototube output due to the grating movement is given from Eq. (4) by $2I_0Ha$. If H is determined by calibration of the instrument, then the fringe contrast can be determined by comparing the voltage modulation due to chopping to the voltage modulation due to the grating movement.

Three types of gratings were considered for the fringes described by Eq. (1). These are a grating with a transmission of the form $g(\nu x - vt) = 1 + b \cos(\nu x - vt)$, a square-wave transmission grating, and a moire fringe grating. The transmitted intensity, I(t), is given by

$$I(t) = \int_{-L}^{L} I(x)\, g(\nu x - vt)\, dx \quad , \tag{5}$$

where L is one-half the length of the grating in a direction perpendicular to the fringes. Notice that Eq. (5) has the same form as the convolution of I(x) and g(x), which will be written $I(x) * g(x)$. But the convolution of two functions is equal to the Fourier transform of the product of the Fourier transforms of the two functions. This may be written

$$I(x) * g(x) = \widehat{\tilde{I}(\mu)\, \tilde{g}(\mu)} \quad , \tag{6}$$

where $\tilde{I}(\mu)$ is the Fourier transform of I(x), and is given by $\tilde{I}(\mu) = \int_{-\infty}^{\infty} e^{2\pi i \mu x} I(x)\, dx$ etc.

COSINE GRATING

If a transmission grating is described by $g(\nu x - vt) = 1 + b(\nu x - vt)$, then

$$\tilde{I}(\mu) = 2I_0 \left\{ L \operatorname{sinc} 2\pi\mu L + a \left[L \operatorname{sinc} L(2\pi\mu + \omega) + L \operatorname{sinc} L(2\pi\mu - \omega) \right] \right\} \tag{7}$$

and

$$\tilde{g}(\mu) = 2 \left\{ L \operatorname{sinc} 2\pi\mu L + b \cos vt \left[L \operatorname{sinc} L(2\pi\mu + \nu) + L \operatorname{sinc} L(2\pi\mu - \nu) \right] \right\} , \tag{8}$$

where $\operatorname{sinc} x = \sin x/x$ and μ is a dummy variable in Fourier transform space.

When ω does not exactly equal ν, two sinc functions will overlap, as shown in Figure 46. Since the sinc function centered at $\omega/2\pi$ has zeros at $\omega/2\pi \pm 1/2L$, etc., and $P \approx (1/2)\left[(\omega/2\pi) + (\nu/2\pi)\right]$, we will write the area of overlap as

$$\text{O.L.} = \int_A^B f\left(\frac{\nu}{2\pi}\right) d + \int_B^C f\left(\frac{\omega}{2\pi}\right) d \approx 2 \int_A^B f\left(\frac{\nu}{2\pi}\right) d\mu \quad , \tag{9}$$

where A is $\left(\frac{\nu}{2\pi} - \frac{1}{2L}\right)$, B is $\frac{1}{2}\left(\frac{\omega}{2\pi} + \frac{\nu}{2\pi}\right)$, and C is $\left(\frac{\omega}{2\pi} + \frac{1}{2L}\right)$.

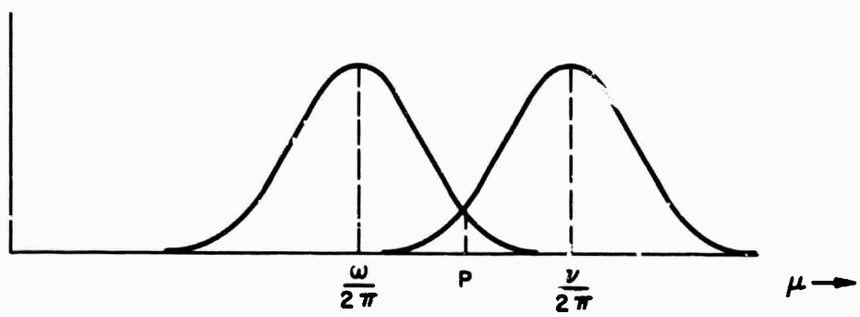

Figure 46. Overlap of Two Sinc Functions

Examining the case where $f(\nu/2\pi) = L \text{ sinc } L(2\pi\mu - \nu)$, we have

$$\text{O.L.} = \left[1 - (\nu - \omega)L\right] \quad , \tag{10}$$

where we have normalized to the area of one of the sinc functions. Letting ϵ be the error between the two frequencies and n be the number of fringes per unit length and noting that Eq. (10) represents $f(\omega - \nu)$ in Eq. (4), we rewrite Eq. (10) as

$$f(\omega - \nu) = 1 - L\epsilon n \quad . \tag{11}$$

Now we may write I(t) as

$$\begin{aligned} I(t) &= \widetilde{\tilde{g}(\mu)\, \tilde{I}(\mu)} = \int_{-L}^{L} e^{-i\mu 2\pi x}\, \tilde{I}(\mu)\, \tilde{g}(\mu)\, (1 - L\epsilon n)\, d\mu \\ &\approx 8 I_o L \left[1 + 0.5\, ab(1 - L\epsilon n) \cos vt\right] \quad , \end{aligned} \tag{12}$$

where the approximation has been made that 2L is much greater than one fringe width. Note that in our calculations we have assumed that $a \approx b$ when we evaluated Eq. (9). Since for $\omega = \nu$ the area of overlap is the area of the smaller of the two sinc functions, we will approximate for small frequency errors, i.e., $[(\omega/2\pi) - (\nu/2\pi)] << 1/2L$, so that Eq. (12) becomes

$$I(t) \approx 8I_o L[1 + 0.5\,ab\,\alpha(1 - L\epsilon n)\cos vt] \tag{13}$$

where α is the smaller of the ratios of a to b or b to a and, of course, where L is the same for both the grating and the fringes, as it will be in any case we consider.

In Eq. (12) the dc component of the transmitted intensity is given by $8I_oL$ and the ac signal, S, is given by

$$S = 8I_o L(0.5)\,ab(1 - L\epsilon n)\cos vt \quad . \tag{14}$$

Now for a maximum signal we have

$$\frac{dS}{dL} = 0 = 1 - 2L\epsilon n$$

or (15)

$$L = \frac{1}{2\epsilon n} \quad .$$

Thus, given n and monitoring S as a function of L we can determine ϵ for the purpose of calibrating the instrument. For maximum instrument sensitivity we want S to be a maximum; so we have $1 - L\epsilon n = 1/2$. Equation (12) then becomes

$$I(t) = 8I_o L(1 + 0.25\,ab\cos vt) \quad . \tag{16}$$

In practice, of course, it would be ideal if ϵ were so small that S increased linearly with L.

SQUARE-WAVE GRATING

Consider a square-wave grating where F(x) is described by Figure 45; thus

$$\tilde{F}(\mu) = \left[\sum_{m=-n}^{m=n} \int_{md-c}^{md+c} A\, e^{i\mu 2\pi x}\, dx + \int_{md+c}^{md-c} B\, e^{i\mu 2\pi x}\, dx\right] . \tag{17}$$

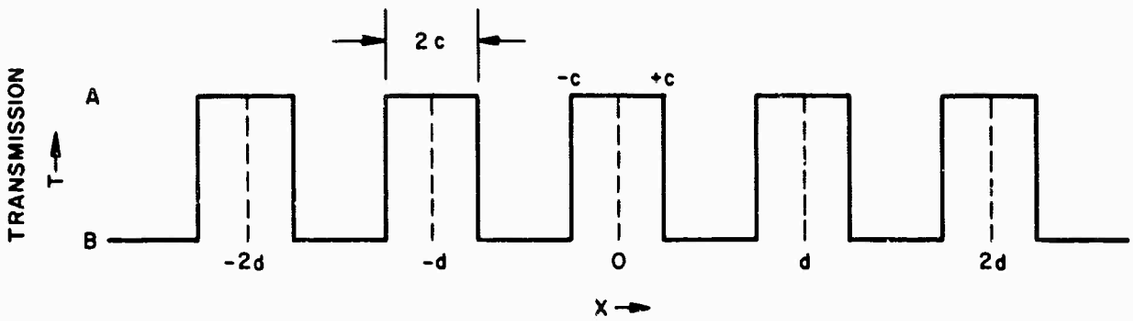

Figure 47. Square-Wave Grating

If we let A = 1 and B = 0, we have

$$\tilde{F}(\mu) = \sum_{m=-n}^{m=n} \frac{e^{+i\mu 2\pi md}}{i\mu 2\pi}\left(e^{i\mu 2\pi c} - e^{-i\mu 2\pi c}\right)$$

$$= 2c \text{ sinc } 2\mu\pi c \sum_{m=-n}^{m=n} e^{i\mu 2\pi md} \tag{18}$$

$$= 2c \text{ sinc } 2\mu\pi c \sum_{m=-n}^{m=n} \delta\left(\mu - \frac{m}{d}\right) .$$

This is an array of delta functions whose magnitudes are described by 2c sinc $2\pi\mu c$ and whose widths in Fourier transform space are described by Nd, which corresponds to the L of the cosine grating. To determine the modulation, we will compare the energy in the grating dc term ($\mu = 0$) to the energy in the delta functions located at $\mu = \pm 1/d$, which, in transform space, correspond to appropriate delta (sinc) functions of the fringes if the grating and the fringes are at the same frequency. From Eq. (18) we see that the magnitude of the dc term is simply 2c. The ac signal will have a magnitude of 2c sinc $2\pi c/d$. For $c/d = 0$ we get 100% modulation, but no energy passes through the grating. For $c = d/2$ all the energy passes through the grating, but there is no modulation. For $d = 4c$ the modulation is $\sin(\pi/2)/(\pi/2) = 2/\pi \approx 0.637$. Combining $\tilde{I}(\mu)$ with $\tilde{g}(\mu)$ in accordance with Eq. (6), we get for $d = 4c$

$$I(t) = 4I_o Lc(1 + 0.637a \cos vt) . \tag{19}$$

For the square-wave grating in general I(t) is

$$I(t) = 4I_oLc\left[1 + \operatorname{sinc}\left(\frac{2\pi c}{d}\right) a \cos vt\right] \quad . \tag{20}$$

Let the dimension of the grating in a direction parallel to the fringes be described by h and the angular alignment error between the fringes and the grating be described by θ. Notice that when θ is of such a magnitude that one end of a transmission slit in the grating is aligned with a peak in the fringe field and the other end is aligned with a null or minimum there will be no net modulation. If ℓ is the length of one fringe cycle, then one end of the slit must be displaced by $\ell/2$ from the other end. The angle associated with this condition of zero modulation is given by $\theta_o = \ell/2h$. Under conditions of perfect alignment the transmitted intensity for a grating slit centered on a fringe peak would be proportional to 1 + a. The transmission of the slit is described by a function of the form

$$T(h) = \frac{1}{2\omega}\int_{-\omega}^{\omega} (1 + a\cos\omega)\, d\omega = 1 + a\frac{\sin\omega}{\omega} \quad , \tag{21}$$

where we have normalized by 2ω so we can compare the answer to the case of perfect alignment. Specifically in Eq. (21) $\omega = (\theta/\theta_o)(\pi/2) = h\theta\pi/\ell$. Similarly, when a slit is centered on a minimum in the fringe field, the transmission is of the form

$$T(h) = 1 - a\frac{\sin\omega}{\omega} \quad . \tag{22}$$

The observed fringe contrast, F.C., now is given by

$$F.C. \propto \frac{\left(1 + a\operatorname{sinc}\frac{h\theta\pi}{\ell}\right) - \left(1 - a\operatorname{sinc}\frac{h\theta\pi}{\ell}\right)}{\left(1 + a\operatorname{sinc}\frac{h\theta\pi}{\ell}\right) + \left(1 - a\operatorname{sinc}\frac{h\theta\pi}{\ell}\right)} = a\operatorname{sinc}\frac{h\theta\pi}{\ell} \quad . \tag{23}$$

Thus, the measured fringe contrast will be in error by a factor sinc $h\theta\pi/\ell$. This adjustment is clearly critical, as demonstrated by experimental results reported elsewhere in this report. Equation (23) describes the $f_3(\Delta\phi)$ mentioned in Eq. (4).

Notice that when [see Eq. (11)]

$$L\epsilon = 1/2N \tag{24}$$

there will be no net modulation. We have, in this case, an equation similar to Eq. (21) where now $\omega = L\epsilon/(1/2N)(\pi/2) = L\epsilon N\pi$. The observed fringe contrast is described by

$$\text{F.C.} \propto a \text{ sinc } L\epsilon N\pi \ , \tag{25}$$

which is the $f_1(\omega - \nu)$ of Eq. (4). Thus, the complete equation for a square-wave grating in terms of Eq. (4) is given by combining Eqs. (20), (23), and (25) and may be written as

$$I(t) = 4I_o Lc \left[1 + \text{sinc}\left(\frac{2\pi c}{d}\right) \text{sinc}\left(\frac{h\theta\pi}{\ell}\right) \text{sinc } (L\epsilon N\pi) \text{ a cos vt} \right] \ . \tag{26}$$

The sinc functions in Eq. (26) are plotted in Figure 48.

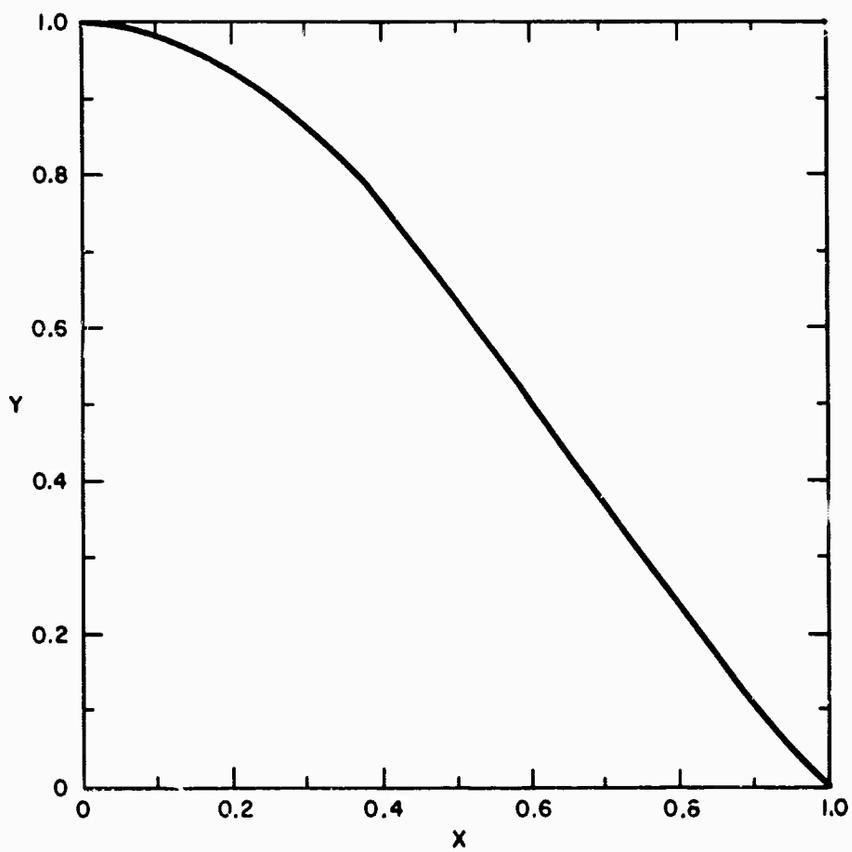

$$y(c) = \text{sinc } \frac{2\pi c}{d} \ , \quad x(c) = \frac{2c}{d}$$

$$y(h) = \text{sinc } \frac{h\theta\pi}{\ell} \quad x(h) = \frac{h\theta}{\ell}$$

$$y(L) = \text{sinc } L\epsilon n\pi \ , \quad x(L) = L\epsilon n$$

Figure 48. Variation of Modulation Index vs Slit Width (2c), Slit Height (h), and Grating Length (L)

MOIRE FRINGE GRATING

When two gratings are superimposed on each other such that the planes of the two gratings are parallel to each other, a set of fringes is formed whose frequency is a function of the frequencies of each of the two gratings and of the angle formed by the slits of the two gratings. When the angle is 0, the moire fringe frequency is a function only of the difference between the frequencies of the two gratings. This frequency will increase as the angle between the two gratings increases.

Starting with the gratings perfectly aligned, $\theta = 0$, then the frequency of the moire fringes, f, is given by

$$f^2 = \nu_1^2 + \nu_2^2 - 2 \cos \theta \, \nu_1 \, \nu_2 \quad , \tag{27}$$

where ν_1 and ν_2 are the frequencies of the two gratings. When $\nu_1 = \nu_2 = \nu$, then we have

$$f^2 = 2\nu^2(1 - \cos \theta) \quad . \tag{28}$$

If $\nu_1 = \nu_2$ and one of the gratings is moved at a velocity V in a direction such that the frequency of the moire fringes does not change but the fringes move in a direction perpendicular to themselves, the velocity V′ of the moire fringe movement is given by

$$V' = \frac{V}{\sin \theta} \quad . \tag{29}$$

This phenomenon, described by Eq. (29), can be employed to achieve large movements of the moire fringes with smaller movements of one of the gratings.

The use of the moire fringe for a modulation grating then has two principal advantages: (a) the frequency may be continuously adjusted in accordance with Eq. (28) and (b) the total grating area required to give the same number of cycles of modulation can be reduced in accordance with Eq. (29).

RELATIVE MERITS OF GRATINGS

Since the square-wave transmission grating was considered in the greatest detail and, in general, such gratings are easily obtained, this type of grating was elected for the original experiments. Although cosine gratings can certainly be ıbricated to some degree of accuracy by properly exposing film to a uniform cosine fringe pattern, the multitude of nonlinearities in such a procedure would make the fabrication of an accurate grating comparatively difficult. This observation, coupled with the fact that large, accurate, relatively inexpensive square-wave gratings can be obtained quickly, indicates the advantage of the square-wave grating. In addition, the square wave is less sensitive to small grating frequency errors, as can be seen by comparison of Eq. (11) with Eq. (25). For both gratings operating at 50% transmission (d = 4c for the square-wave grating and the cosine grating is described by

$1 + \cos \nu x$) the square-wave grating gives a modulation of 0.637 and the cosine grating, a modulation of 0.5. The moire fringe grating has a continuously variable frequency and requires less grating area for equal results. However, the adjustment and use of this grating is more tedious.

EXPERIMENT

EXPERIMENTAL PROCEDURE

A schematic of the experimental setup is shown in Figure 49. With a viewing lens placed at V, the 20-line/cm square-wave grating was rotated in a direction perpendicular to the fringes produced by two 200 μ pinholes placed approximately 0.3 cm apart. Lens L_2 was adjusted along the axis of the optical system until the fringes and the grating formed an array of squares such that the grating and the fringes were approximately at the same frequency. The grating was then rotated to be approximately parallel to the fringes formed by the pinholes. L_2 and the grating rotation were then alternately adjusted until the moire fringe pattern disappeared (i.e., the dimension of the grating was much less than one-half a cycle of the moire fringes).

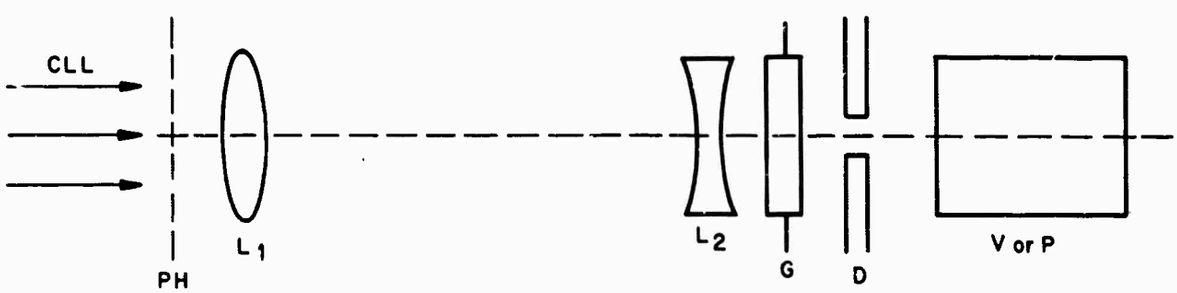

CLL — Collimated Gas Laser Light

PH — Pinholes, 200 μ Diameter, 0.3 Cm Apart

L_1 — 48-In.-Focal-Length Positive Lens

L_2 — Negative Lens Movable to Adjust Fringe Frequency

G — 20-Line/Cm Square-Wave Transmission Grating with Slits and Fringes of Equal Width; Adjustable in Rotation and x and y Directions

V — Optical Viewing Lens System

P — 5819 RCA Phototube with Electronics

D — Aperture in Front of Phototube

Figure 49. Experimental Setup

The viewer was then replaced by a phototube and the recording meter was adjusted to zero when the pinholes were blocked off. The grating was then moved perpendicular to the fringes and the maximum and minimum readings of the meter were recorded. The maximum and minimum readings were taken for several rotational positions of the grating about the aligned position for each of several apertures, D. The diameter of the central diffraction spot of one of the 200 μ pinholes was about 1 cm.

The experimental results are plotted in Figures 50 and 51. The readings, in degrees, are the values recorded from the rotational scale attached to the grating. Ideal alignment was about 40 deg. Here the modulation index represents the apparent fringe contrast, a. This number decreased in accordance with $f_3(\Delta\phi)$ in Eq. (4) as the grating was rotated. The modulation increased in accordance with $f_1(\omega - \nu)$ of Eq. (4) as smaller and smaller sampling areas were used.

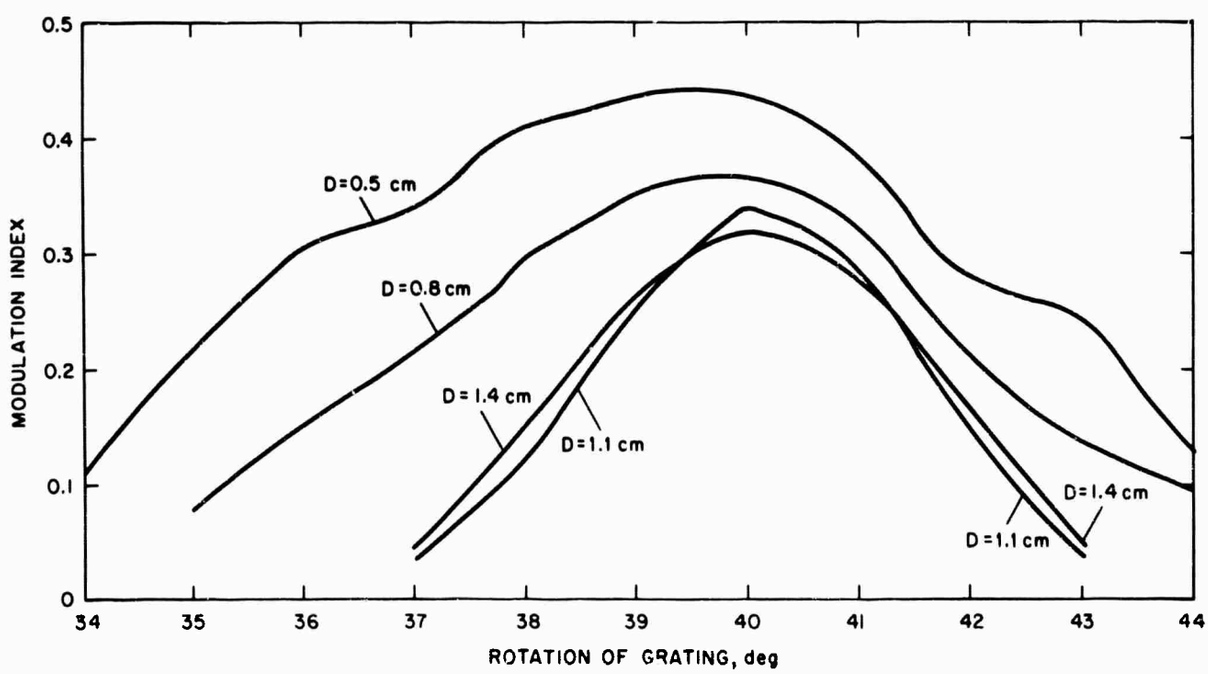

Figure 50. Rotation of Grating vs Modulation Index

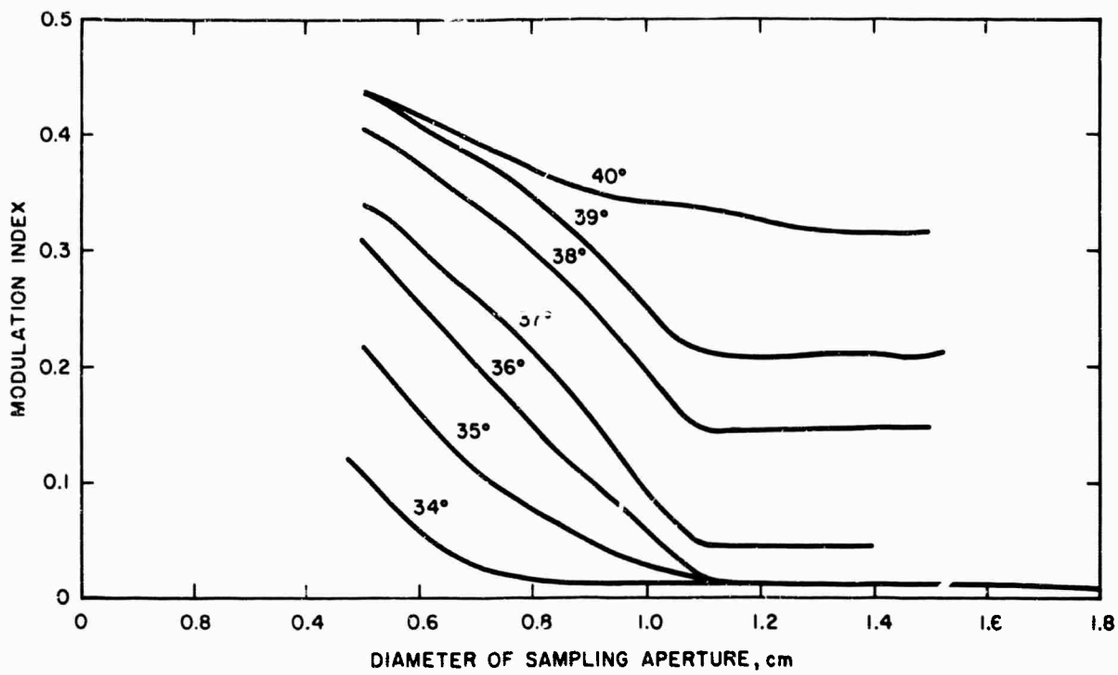

Figure 51. Sampling Aperture vs Modulation Index

DISCUSSION OF RESULTS

Equation (23) describes the modulation as a function of rotation of the grating and predicts a decreased modulation as the grating is misaligned. However, this modulation decrease is for the case where the fringe field is of uniform intensity. This did not apply in our experiment, where, in some cases, the entire Airy disc was sampled and the intensity clearly was not uniform. Similarly, Eq. (25) describes the modulation as a function of L and predicts a decreased modulation as L is increased for $\epsilon > 0$ under conditions of a uniform fringe field. Although a direct correlation of theory with this experiment is not possible until the theory has been expanded to include nonuniform intensities, a good general correlation between theory and experiment can be observed.

One result of this experiment was that a very high percentage of the energy that passed through the pinholes was recorded in the phototube. This turned out to be an important factor in the over-all sensitivity of the final fringe-contrast measuring device. Figure 50 shows, as expected, that the sensitivity to angular alignment becomes less critical as D is decreased because the slit height, h, in Eq. (23) has been decreased. Little change was observed (see Figure 51) as D was increased beyond 1 cm because essentially all the energy was contained in the Airy disc, which had a diameter of approximately 1 cm.

BLANK PAGE

Unclassified
Security Classification

DOCUMENT CONTROL DATA - R&D

(Security classification of title, body of abstract and indexing annotation must be entered when the overall report is classified)

1. ORIGINATING ACTIVITY *(Corporate author)*
Technical Operations Research
Burlington, Mass.

2a. REPORT SECURITY CLASSIFICATION
Unclassified

2b. GROUP

3. REPORT TITLE
Investigation of Electronic Fringe Detector for a Stellar Interferometer

4. DESCRIPTIVE NOTES *(Type of report and inclusive dates)*
Scientific Report. Interim

5. AUTHOR(S) *(Last name, first name, initial)*
Boardman, John, Kellen, Paul, and Nyyssonen, Diana

6. REPORT DATE
7 November 1966

7a. TOTAL NO. OF PAGES
91

7b. NO. OF REFS
8

8a. CONTRACT OR GRANT NO.
AF19(628)-5145
ARPA Order No. 450, Amendment 2, 4

b. PROJECT AND TASK NO.
8663

c. DOD ELEMENT
6250301R

d. DOD SUBELEMENT
N/A

9a. ORIGINATOR'S REPORT NUMBER(S)
TO-B 66-91
Scientific Report No. 1

9b. OTHER REPORT NO(S) *(Any other numbers that may be assigned this report)*
AFCRL-66-767

10. AVAILABILITY/LIMITATION NOTICES
Distribution of this document is unlimited

11. SUPPLEMENTARY NOTES
Prepared for Hq. AFCRL, OAR(CRO)
United States Air Force
L. G. Hanscom Field, Bedford, Mass.

12. SPONSORING MILITARY ACTIVITY
Advanced Research Projects Agency

13. ABSTRACT

A fringe detector was constructed to detect fringes from a Michelson stellar interferometer and to relate these measurements to the characteristics of the source of illumination. This instrument has variable separation apertures adjustable from 0.6 to 6 cm. Aperture height is maintained at 0.1 times the separation. An optical system produces the fringe pattern by superimposing the partially coherent light entering the two apertures. A rotating reflector, single slit, and phototube combine to transform the spatially varying intensity pattern of the fringe field into a time-varying voltage signal displayed on an oscilloscope face. The oscilloscope trace is photographed and analyzed to determine fringe contrast.

The maximum sensitivity of the detector was determined to be equivalent to a source providing 10^{-10} watts/cm^2 at a fringe contrast of 1 and a signal-to-noise ratio of 1. Improvements in the entrance aperture configuration, phototube sensitivity, and the use of a grating instead of a single slit can provide a factor of 500 to 1000 improvement in detector sensitivity. The interferometer was determined to have potentially better resolution than a single-mirror telescope because it can electrically filter the effects of ambient background illumination and turbulence. The use of an interferometer to measure the angular size of a pie-shaped source was studied and found to be not particularly suited to this purpose.

DD FORM 1 JAN 64 1473

Unclassified
Security Classification

14. KEY WORDS	LINK A ROLE	LINK A WT	LINK B ROLE	LINK B WT	LINK C ROLE	LINK C WT
Electronic Fringe Detector						
Michelson Stellar Interferometer						
Coherence						

INSTRUCTIONS

1. ORIGINATING ACTIVITY: Enter the name and address of the contractor, subcontractor, grantee, Department of Defense activity or other organization *(corporate author)* issuing the report.

2a. REPORT SECURITY CLASSIFICATION: Enter the overall security classification of the report. Indicate whether "Restricted Data" is included. Marking is to be in accordance with appropriate security regulations.

2b. GROUP: Automatic downgrading is specified in DoD Directive 5200.10 and Armed Forces Industrial Manual. Enter the group number. Also, when applicable, show that optional markings have been used for Group 3 and Group 4 as authorized.

3. REPORT TITLE: Enter the complete report title in all capital letters. Titles in all cases should be unclassified. If a meaningful title cannot be selected without classification, show title classification in all capitals in parenthesis immediately following the title.

4. DESCRIPTIVE NOTES: If appropriate, enter the type of report, e.g., interim, progress, summary, annual, or final. Give the inclusive dates when a specific reporting period is covered.

5. AUTHOR(S): Enter the name(s) of author(s) as shown on or in the report. Enter last name, first name, middle initial. If military, show rank and branch of service. The name of the principal author is an absolute minimum requirement.

6. REPORT DATE: Enter the date of the report as day, month, year, or month, year. If more than one date appears on the report, use date of publication.

7a. TOTAL NUMBER OF PAGES: The total page count should follow normal pagination procedures, i.e., enter the number of pages containing information.

7b. NUMBER OF REFERENCES: Enter the total number of references cited in the report.

8a. CONTRACT OR GRANT NUMBER: If appropriate, enter the applicable number of the contract or grant under which the report was written.

8b, 8c, & 8d. PROJECT NUMBER: Enter the appropriate military department identification, such as project number, subproject number, system numbers, task number, etc.

9a. ORIGINATOR'S REPORT NUMBER(S): Enter the official report number by which the document will be identified and controlled by the originating activity. This number must be unique to this report.

9b. OTHER REPORT NUMBER(S): If the report has been assigned any other report numbers *(either by the originator or by the sponsor)*, also enter this number(s).

10. AVAILABILITY/LIMITATION NOTICES: Enter any limitations on further dissemination of the report, other than those imposed by security classification, using standard statements such as:

(1) "Qualified requesters may obtain copies of this report from DDC."

(2) "Foreign announcement and dissemination of this report by DDC is not authorized."

(3) "U. S. Government agencies may obtain copies of this report directly from DDC. Other qualified DDC users shall request through _____."

(4) "U. S. military agencies may obtain copies of this report directly from DDC. Other qualified users shall request through _____."

(5) "All distribution of this report is controlled. Qualified DDC users shall request through _____."

If the report has been furnished to the Office of Technical Services, Department of Commerce, for sale to the public, indicate this fact and enter the price, if known.

11. SUPPLEMENTARY NOTES: Use for additional explanatory notes.

12. SPONSORING MILITARY ACTIVITY: Enter the name of the departmental project office or laboratory sponsoring *(paying for)* the research and development. Include address.

13. ABSTRACT: Enter an abstract giving a brief and factual summary of the document indicative of the report, even though it may also appear elsewhere in the body of the technical report. If additional space is required, a continuation sheet shall be attached.

It is highly desirable that the abstract of classified reports be unclassified. Each paragraph of the abstract shall end with an indication of the military security classification of the information in the paragraph, represented as *(TS)*, *(S)*, *(C)*, or *(U)*.

There is no limitation on the length of the abstract. However, the suggested length is from 150 to 225 words.

14. KEY WORDS: Key words are technically meaningful terms or short phrases that characterize a report and may be used as index entries for cataloging the report. Key words must be selected so that no security classification is required. Identifiers, such as equipment model designation, trade name, military project code name, geographic location, may be used as key words but will be followed by an indication of technical context. The assignment of links, rules, and weights is optional.